# Stellar Formation in the Carina South Pillars Region

by

**Jesús Abraham Reyes De Librado**

Thesis submitted in partial fulfillment of the requirements
for the degree of

**MASTER OF SCIENCE IN ASTROPHYSICS**

at the

**Instituto Nacional de Astrofísica, Óptica y Electrónica**
May 2013
Tonantzintla, Puebla

Advised by:

**Dr. Bertha Alicia Porras Juárez**
Tenured Researcher INAOE

# Acknowledgment

Quiero agradecer en primer lugar a mi mamá, Yolanda De Librado Sánchez, por todo su amor, comprensión, consejos, paciencia y un sinfin de cosas más que me han ayudado a lo largo de mi vida. También le agradezco al resto de mi familia su apoyo incondicional en todo momento.

Le agradezco mucho a mi asesora, Dra. Alicia Porras, el haberme aceptado como su estudiante, los útiles consejos que me proporcionó, pero sobre todo, la paciencia que tuvo al estar todo este tiempo conmigo trabajando en esta tesis.

Agradezco al Dr. David Hughes el haber proporcionado los datos milimétricos, sin ellos, esta tesis no hubiera sido posible. También les doy las gracias a los estudiantes de doctorado del INAOE, David Sanchez y Milagros Zeballos, por sus consejos en el manejo de estos datos. Gracias también a los doctores Divakara Mayya y Manuel Corona por sus valiosas sugerencias en la presentación de este trabajo. Y de forma particular, agradezco a la dra. Irene Cruz-González por sus significativos comentarios en la escritura de mi tesis.

También agradezco a mis compañeros de generación, quienes a pesar de haber terminado mucho antes que yo, siguieron apoyándome todo este tiempo. De igual manera, agradezco a mis amigos de la universidad y a mis camaradas del bachiller por sus ánimos, especialmente a esos que se la pasaban preguntando cada vez que me los encontraba: ¿Cuándo terminas tu maestría?

Los resultados parciales de esta tesis fueron presentados en los siguientes Congresos:

- Encuentro Regional de Ciencias, Benemérita Universidad Autónoma de Puebla, Noviembre 2010
- Congreso Nacional de Astronomía, Guadalajara, Jalisco, Septiembre 2011
- New Quests in Stellar Astrophysics III, Puerto Vallarta, Jalisco, Marzo 2012 (in Proceedings)

# Contents

# Chapter 1

# Introduction

## 1.1 Massive stars. Definitions.

Massive stars are one of the most interesting and prominent objects in the Universe. They are known as the principal source of heavy elements and UV radiation using a combination of winds, massive outflows, expanding HII regions and supernova explosions. Thus, massive stars directly affect the evolution of the Universe in the processes of how stars and planets are formed.

In Table 1.1, is presented a crude classification of massive stars and the corresponding main sequence spectral types given by Zinnecker & Yorke (2007).

Table 1.1: Main-sequence massive star definition.

| **Mass** | **Designation** | **Sp. Type** |
|---|---|---|
| 8-16 $M_{\odot}$ | Early B-Type massive stars | B3V to B0V |
| 16-32 $M_{\odot}$ | Late O-Type massive stars | O9V to O6V |
| 32-64 $M_{\odot}$ | Early O-Type massive stars | O5V to O2V[a] . |
| 64-128 $M_{\odot}$ | O/WR-type massive stars | WNL-H[b] |

---

[a] O2V main-sequence stars have been identified by Walborn et al. (2002)

[b] WNL-H: N-rich late type Wolf-Rayet type stars, still on the main sequence (see Crowther, 2007).

## 1.2 Theoretical and observational difficulties in the study of massive star formation

In the case of low-mass stars, the process that describes the major evolutionary stages of protostars follows this model: (a) A stage of accretion, characterized by the presence of a central protostar and a circumstellar disc surrounded by a falling envelope of gas and dust; (b) A second phase in which the protostar dispose of angular and lineal momentum together with the kinetic energy in its surroundings through jets and molecular fluxes; and finally (c) a stage relatively more advanced in which the protostar is settled in the zero age main sequence (ZAMS), increasing its luminosity. This model has been useful to explain the observationally known behavior shown on low-mass stars, its usefulness and application to the high-mass star formation is open to be discussed (Garay & Lizano, 1999). The early stages of formation of massive stars are still poorly understood: first, it is known that the evolutionary time-scales of high-mass stars are shorter that these for low-mass stars. Also, it is expected that massive stars affect their surrounding medium quickly after the stellar nucleus has been formed, that means that these stars start to burn Hydrogen and reach the main sequence before they start to accrete material from the surrounding stellar envelope. The formation of a massive disk and therefore the appearance of the molecular fluxes and jets in the accretion phase is not clear yet (see Zinnecker & Yorke, 2007). Besides, in the stage (c) the massive star starts to produce an appreciable output of UV photons and possibly develop strong winds which will drastically affect the physical conditions, the structure, and the chemical composition of its surroundings. Since in this phase the massive star ionizes its surroundings, this stage is usually referred as the Ultra Compact (UC) HII region. An understanding of the physical processes that dominate during these early phases in the massive star formation and its influence on the surrounding medium in which they were formed requires a detailed knowledge about the conditions of the previous and after conditions of star formation.

The difficulties in determining the physical parameters of the gas during the early formation and evolution of an individual massive star are not only because of fast evolution, but also due to some observational disadvantages. It is known that massive stars born deeply embedded in molecular cores, that means that the star forming process is obscured by the surrounding dust and so it cannot be investigated in the visible wavelengths. Garay et al. (1993) observed with arcsecond angular resolution the radio continuum emission toward 16 highly luminous IRAS point sources known to be associated with compact HII regions detected with single-dish telescopes. They found that a large fraction of these sources, particularly the most luminous ones, exhibit complex radio morphologies which could be decomposed into multiple components, strongly supporting the premise that massive stars tend to born in rich groups or clusters. This statement means that the individual studies of these sources are affected by confusion, because massive stellar objects are at larger distances than the low mass stars formation sites.

It is important to recall that O and B stars emit their radiation volume at wavelengths shorter than the Lyman continuum ($\lambda \sim 912 - 940$ $\AA$), which ionizes the dense molecular gas producing compact HII regions. Also, the circumstellar dust surrounding the region of ionized gas absorbs all the stellar radiation, either directly or after has been processed in the nebula, producing compact regions of hot dust that re-emit the absorbed energy at Infrared (IR) wavelengths. Therefore, studies of the young massive stars and their environment are better made through observations in radio, millimeter and IR wavelengths, where the dust and gas opacity are considerably lower.

The Garay & Lizano’ review concludes that observational evidence gathered in the paper and other authors within shows the existence of hot and very dense molecular structures undergoing large mass accretion rates and attesting that during the process of collapse of massive stars, massive disks are formed and bipolar outflows appears and indicate that the formation of massive stars from massive prestellar cores shares similar characteristics with those of low-mass stars. Although the massive prestellar cores appear in clusters and could be formed by a complex accumulation process starting with smaller clumps within massive clouds, the observational evidence at that time suggests that massive stars are formed by the collapse of single massive prestellar cores, rather than by an accumulation process, and suggests that the paradigm of low-mass star formation is more universal than previously thought.

Moreover, Ercolano et al. (2013) discuss the effect of the ionizing radiation from Massive Young Stellar Objects in their SEDs. They mention that for stars $> 8\ M_\odot$ few protoplanetary disk have been found: W33A (Davies et al., 2010), IRAS 13481-6124 (Kraus et al., 2010). According to Preibisch et al. (2011), no circumstellar disc surrounding stars higher than $\sim 20\ M_\odot$ has been reported actually. And very recently, from SOFIA observations (Herter et al., 2012), Zhang et al. (2013) observed the massive protostar G35.20-074 in 11.3, 19.7, 31.5, and 37.1 $\mu$m. Fitting a SED with fluxes from near-IR to mm, they found that the source G.35 has a mass $\sim$20 - 34 $M_\odot$ and $L_{bol}$ $\sim$0.7 - 2.2 $\times 10^5\ L_\odot$ depending on the outflow cavity opening angle (35° to 50°). They conclude that G35.2 is a massive protostar, forming from high surface density core and clump, via relatively ordered, symmetric collapse and accretion. The best fitted model shows an outer disk of 940 AU and a mass of $\sim$1/3 of its stellar mass.

Two different theoretical mechanisms have been proposed to explain the formation of massive stars: accretion and coalescence. In the first hypothesis (Osorio et al., 1999; Yorke & Sonnhalter, 2002; McKee & Tan, 2003; Yorke, 2004; Krumholz et al., 2009) it is assumed that massive stars are formed via accretion of gas in dense cores. In the coalescence scenario (Stahler et al., 2000; Zinnecker, 2004) it is proposed that high-mass stars form by merging of low and intermediate mass stars in a dense cluster environment (Bonnell et al., 1998). The role of coalescence and accretion processes in the assembling of a massive star is still under debate. To discern which of the two competing models best explain the formation of massive stars, it is necessary to appeal to observational data which would place strong constraints on the theoretical models.

Observations show that high-mass stars are born within massive dense cores with approximately this features: typical radii of $\sim$ 0.4 pc, densities of $\sim 10^6$ cm $^{-3}$, masses of a few $10^3\ M_\odot$ and line widths of $\sim\ 6$ km s$^{-1}$. It appears that a significant fraction of the total mass of the massive dense cores is in the form of molecular gas, also suggested by the values of the masses derived from the dust continuum emission (gas mass) and virial mass (total mass), indicating that the gas dominates the gravitational potential. Moreover, the observations provide clear evidence that high-mass stars are preferentially born near the center of young stellar clusters (Lada & Lada, 2003; Parker & Goodwin, 2007). This is unlikely to be result of the dynamical evolution, since the ages of the stars are smaller than the required collisional relaxation times (Bonnell et al., 1998; Hillenbrand & Hartmann, 1998). The questions of how an individual massive star forms and how the cluster forms are therefore closely related. Whatever mechanism may be used, an overall model for the formation of massive stars should explain these observational facts.

So, how are massive dense cores produced? Larson (1982) suggested that dense cores might be formed by a gradual dissipation of turbulent motions in larger clouds. This will cause the gravitational contraction of the large cloud while still remaining nearly in virial equilibrium reducing its size and increasing its internal velocity dispersion. The gas escapes to the center of the core where is accreted by the central object at high rates.

How are high-mass stars formed? In the two main theoretical ideas, the birth of massive stars is seen as an event associated with a very dense environment. In the coalescence model the determining parameter is the stellar density, whereas in the accretion model it is the gas density. In the accretion induced collisions mechanism (Bonnell et al., 1998) is suggested that the process of building up massive stars by collisions with lower mass objects is more efficient at the center of the cluster where considerable more dynamical interactions take place, qualitatively explaining one of the observational facts. For stellar mergers to be responsible for the formation of massive stars, stellar densities of $\geq 10^8$ stars pc$^{-3}$ are required (Bonnell, 2002). Several observations at IR wavelengths, which are able to probe the population of newly formed stars deeply embedded in molecular clouds, do indeed show that massive stars form at the center of young rich clusters, with sizes of $0.2 - 0.4$ pc, containing a high density of low-mass stars (Megeath et al., 1996b; Carpenter et al., 1997; Porras et al., 2000, for cluster sizes less than 2 pc). The young embedded dense clusters have, however, stellar volume densities $\leq 10^4$ stars pc$^{-3}$, which are at least four orders of magnitude smaller than that required theoretically.

The accretion hypothesis requires that the parental cores be dense enough such that upon collapse the ram pressure of the associated accretion inflow overcame the radiative forces on dust. It appears that in isolated massive dense cores this takes place near their central regions. This observational evidence is consistent with the hypothesis that the formation of massive stars proceeds via accretion in very dense cores. In the turbulent and pressurized dense core accretion model (McKee & Tan, 2003), the collapse of a massive dense core is likely to produce the birth of a stellar cluster, with most of the mass going into relatively low-mass stars. The high-mass stars are formed preferentially at the center of the core, where the pressure is the highest, and in short time scales of $\sim 10^5$ years (Osorio et al., 1999; McKee & Tan, 2002)

The observational evidence for understanding massive star formation summarized above by Garay (2004) allow to differentiate between the two theoretical possibilities mentioned. The recollected data in the article shows that bipolar molecular outflows, jets and disks appear to be intrinsic to the formation process of high-mass stars (Plambeck et al., 2009; Wang et al., 2011). Flow energetics and jet radio luminosities appear to scale with the luminosity of the central source. The discovery that the phenomena of molecular outflows and jets are also basic components of the formation process of high-mass stars provide strong support to the hypothesis that massive OB stars are formed via accretion through a disk in an analogous manner to the formation of low-mass stars. The main difference between high-mass and low-mass stars formation via accretion is the mass accretion rate. Mass accretion rates as high as $1 \times 10^{-2}\ M_\odot$ yr$^{-1}$ have been estimated in collapsing cores associated with high-mass star forming regions (Zhang & Ho, 1997; Hofner et al., 1999), whereas those associated with the formation of low-mass stars are typically $\sim 10^{-6}\ M_\odot$ yr$^{-1}$.

## 1.3 Eta Carina Region

### 1.3.1 What is $\eta$ Carina?

Eta Carina ($\eta$ Car) is arguably the most remarkable stellar object that is possible to be observed in great detail. It is the nearest and most luminous evolved star that can be studied within the Milky Way. It mass is about 100 $M_\odot$ and its luminosity is about $1.9 \times 10^{40}$ erg $\approx 10^{6.7}\ L_\odot$, with an uncertainty of about $\pm 20\%$ (Davidson & Humphreys, 1997). This stellar object is the brightest extrasolar IR source in the sky at 20 $\mu$m, and has one of the most famous stellar winds (Cox et al., 1995) at millimeter or centimeter wavelengths. Besides, $\eta$ Car has produced one of the most elegant of all known bipolar nebulae: The Homunculus Nebula. The two lobes of this object appear nearly circular, and each one has a diameter of about 0.1 pc (see references in Davidson & Humphreys, 1997).

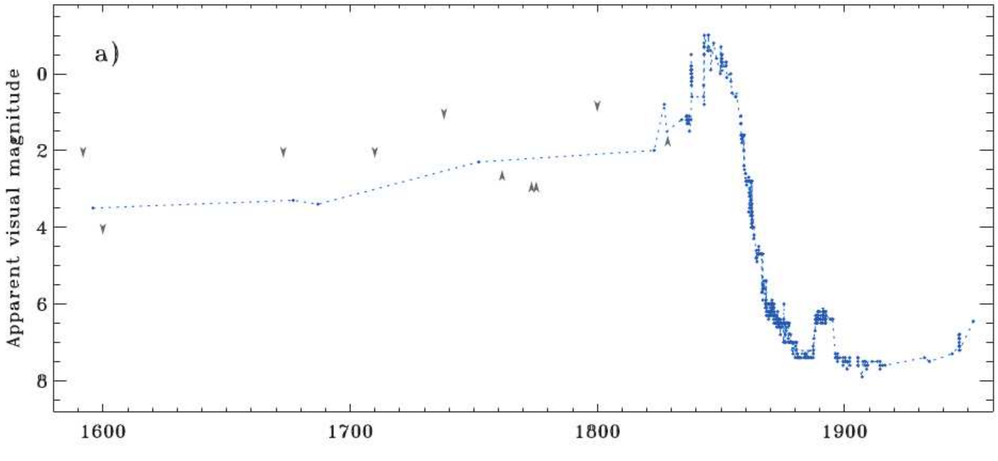

Figure 1.1: $\eta$ Car light curve from the most recent set of visual data (Smith & Frew, 2011), from 1596 to about 1960.

The unusual variability of $\eta$ Car was noted early in the 17th century by Halley, when it was reported to vary between 4th and 2nd magnitude.

Later, in the early and mid 19th century, it was observed by John Herschel in 1847, and started to brighten significantly to become the second brightest star in the sky until 1870, then became fainter (see Fig. 1.1) During that event, the star ejected more than 10 $M_{\odot}$ of material with almost $10^{50}$ erg of kinetic energy, which has since expanded to form the so-called "Homunculus" nebula seen today in HST images (Humphreys & Davidson, 1994; Currie et al., 1996). After more than 160 years, the underlying cause of this so-called event "The Great Eruption" is still the most enduring and intriguing mystery associated with $\eta$ Car.

In the analysis of the above event, it was discovered that $\eta$ Car brightened more than usual and fluctuated between first and zero magnitude for almost 20 years. After 1856 it faded, apparently stabilizing at 7th or 8th magnitude around 1870. Except for a Lesser Eruption between 1887 and 1895, $\eta$ Car has appeared more stable since 1870 than it was in the centuries preceding the Great Eruption. After 1900, a very pretty expanding circumstellar ejecta-nebula became visible, the already mentioned "Homunculus" Nebula. Since 1940, $\eta$ Car has actually started to brighten again and it is lately between 6th and 5th magnitude (van Genderen et al., 1993, 1994).

Twentieth-century astronomers realized that $\eta$ Car is more than 1 kpc away, which makes the Great Eruption an extremely luminous event: it might be an unusual nova, a slow supernova or a massive protostar. Gaposchkin (1957) and Burbidge (1962) called it an unstable yellow supergiant; and later, Westphal & Neubebauer (1969) made the discovery that now most of the star's luminosity emerges at IR wavelengths beyond 10 $\mu$m, in an amount comparable to what was seen at visual wavelengths during the Great Eruption. This circumstellar visual extinction together with the powerful IR emission of the stars give as a result that the central object's present luminosity dominates at UV wavelengths. That means that most of this energy flux is absorbed by dust that has formed in the ejecta from the Great Eruption and the dust re-radiates it as a thermal IR emission.

### 1.3.2 The Carina Nebula

The Carina Nebula is the southern hemisphere's largest and highest surface brightness nebula (see Fig. 1.2). Most observational effort in the Carina Nebula has been focused on the variable star $\eta$ Car and its immediate surroundings. This object give us an ideal laboratory in which we can study the ongoing star formation in the vicinity of some of the most massive stars known, including of course $\eta$ Car. The advantage of working in this nebulae compared to other sites of star formation like 30 Dor in the Large Magellanic Cloud (Massey & Hunter, 1998; De Marchi et al., 2011), is that in the Carina Nebula one can make detailed studies of small-scale phenomena, like protoplanetary discs and jets, because these studies in remote regions are hampered by considerably more extinction due to their greater distances. Besides, the sightline to the Carina Nebula also suffers little reddening, which gives the opportunity for detailed visual-wavelength studies of the stars and fainter nebulosity. Although a casual look at an optical image reveals that extinction is highly position-dependent in the nebula. In conclusion, the low extinction toward Carina combined with its proximity and rich nebular content offer us pretty useful and interesting information that is worth studying.

The Carina Nebula resides in one of the richest regions of the Milky Way, from the point of view of massive star formation. Unlike most massive star formation regions, the distance to the Carina Nebula is known accurately: it is around 2.3 kpc and is accurate to ±2% (Allen & Hillier, 1993; Smith, 2002, 2006), which is approximately the same distance to $\eta$ Car, the KeyHole Nebula and the cluster Tr 16.

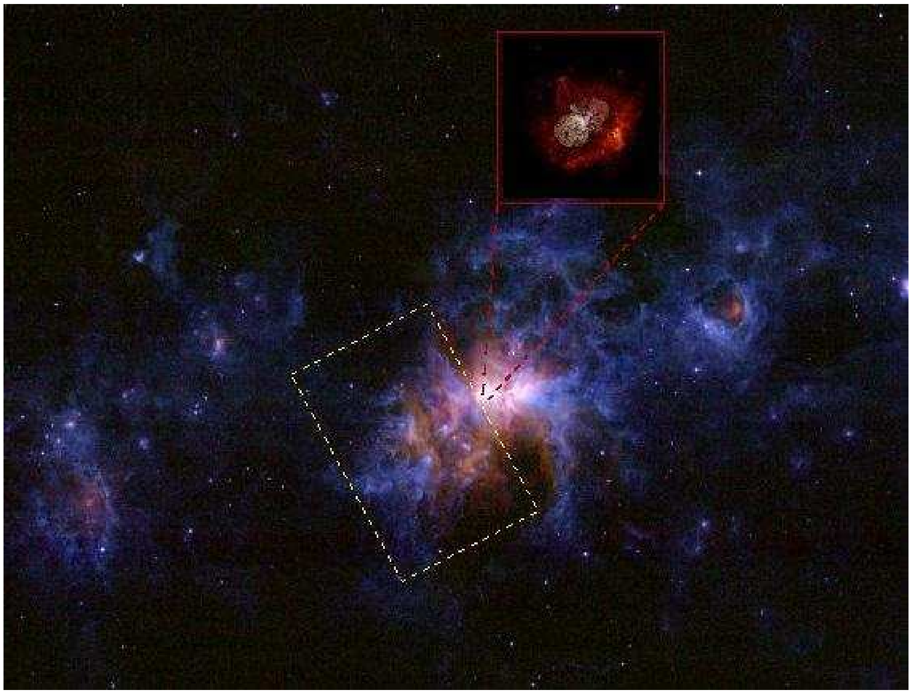

Figure 1.2: Color composite MSX map[1] (Red=14.65 $\mu$m, Green=12.13 $\mu$m, and Blue=8.28 $\mu$m) showing the position of $\eta$ Car and a zoom of the optical composite image[2] (Red=6306 $\AA$, Green=4090 $\AA$, and Blue=3342 $\AA$) of the Homunculus. The South Pillar region of about one square degree studied in this thesis, is shown with a dashed line rectangle.

From the point of view of understanding star formation in the region, two important facts should be taken into account:

1. Although $\eta$ Car is probably the most massive and luminous star known in the Milky Way, at the current time it contributes essentially nothing to the radiative energy budget of the surrounding region. This strange phenomena arises, because $\eta$ Car is currently surrounded by the nearly opaque dust shell ejected 160 years ago in the ”Great Eruption” (see above section), which absorbs nearly all of the star’s UV and visual luminosity. As mentioned previously, that luminosity is then re-radiated in the thermal IR and it has been found that is exerting little influence on the surrounding gas in the star-forming complex (Smith & Brooks, 2008).

2. However, before 1843 (for about 3 Myr prior), $\eta$ Car had a tremendous influence on the UV energy budget of the entire region, since this luminosity dominated the ionization of the main cavity and it sculpted many of the most prominent elephant trunks in the region (Rathborne et al., 2004). When the ”Great Eruption” ended and $\eta$ Car faded due to dust obscuration, the UV luminosity of the region dropped by 20% (Smith, 2006) and the remaining O stars scattered through the region now dominate the ionization.

The first radio observations within Carina nebula were focused on the central region and identified two bright concentrations known as Car I ($\alpha = 10^h41^m36.0^s$, $\delta = -59°19'09''$ ) and Car II ($\alpha = 10^h43^m07.2^s$, $\delta = -59°22'38''$ ) (Gardner et al., 1970). Subsequent observations established that these two sources were thermal and represented two separated HII regions. Car I was found to be located toward the north-western part of the inner nebula, and Car II was identified with the central KeyHole nebula.

The Carina Nebula is probably best known as the dwelling of $\eta$ Car. While on the main sequence, this one star dominated the evolution of the surrounding HII region. However, $\eta$ Car often outshines its several spectacular neighbors that also occupy the interior of the Carina Nebula, distributed in several sub-clusters. In addition to $\eta$ Car itself, Carina boasts an O2 supergiant (HD 93129A; Walborn et al. (2002)), three WNH Stars (late-type WN stars with hydrogen; see Crowther et al. (1995); Smith & Conti (2008)), several O3 stars, and more than 60 additional O stars (see Smith, 2006). Because of its remarkable stellar content and observability, Carina has often been in the forefront of understanding very massive stars, since it is the first place where the (then) earliest spectral type O3 stars were recognized (Walborn, 1973), and an O2 Ia supergiant was classified (Walborn, 2002). A summary of some of these early-type stars is presented at Table 1.2

Table 1.2: Some examples of early-type stars within the Carina nebula.

| **Name** | $\alpha$ | $\delta$ | **Spectral Type** | **Source** |
|---|---|---|---|---|
| HD 93129A | $10^h43^m57.50^s$ | $-59°32'53.00''$ | O2 If* | Walborn et al. (2002) |
| WR 22 | $10^h41^m17.52^s$ | $-59°40'36.90''$ | WN7+abs | Smith & Brooks (2008) |
| WR 24 | $10^h43^m52.26^s$ | $-60°07'04.02''$ | WN6ha-w | Smith & Brooks (2008) |
| WR 25 | $10^h44^m10.33^s$ | $-59°43'11.41''$ | WN+ | Smith & Brooks (2008) |
| HD 93205A | $10^h44^m33.74^s$ | $-59°44'15.46''$ | O3.5 V((f)) | Smith (2006) |
| HD 93129 | $10^h43^m57.46^s$ | $-59°32'51.30''$ | O3Iab | Smith (2006) |
| HD 93128 | $10^h43^m54.37^s$ | $-59°32'57.37''$ | O3.5 V((f+)) | Smith (2006) |
| HD 93250 | $10^h44^m45.03^s$ | $-59°33'54.68''$ | O3.5 V((f)) | Smith (2006) |
| HDE 303308 | $10^h45^m05.85^s$ | $-59°40'06.36''$ | O4 V((f)) | Smith (2006) |
| Tr16-244 | $10^h44^m13.19^s$ | $-59°43'10.33''$ | O4 If | Smith (2006) |
| HD 93204 | $10^h44^m32.33^s$ | $-59°44'31.00''$ | O5V((f)) | Smith (2006) |
| HDE 303311 | $10^h44^m37.46^s$ | $-59°32'55.44''$ | O5 V | Smith (2006) |

### 1.3.3 Carina South Pillars Region

In the past few years, it was found that the most active region of ongoing star formation in the Carina Nebulae is the so-called "South Pillars Region" (here on called as SPR Smith & Brooks, 2008, see Fig. 1.3), where winds and UV radiation from the central clusters Tr 14 and Tr 16 are sweeping through and destroying a Giant Molecular Cloud (GMC). The importance of this region was recognized after wide field thermal-IR images from the MSX satellite became available (Smith et al., 2000).

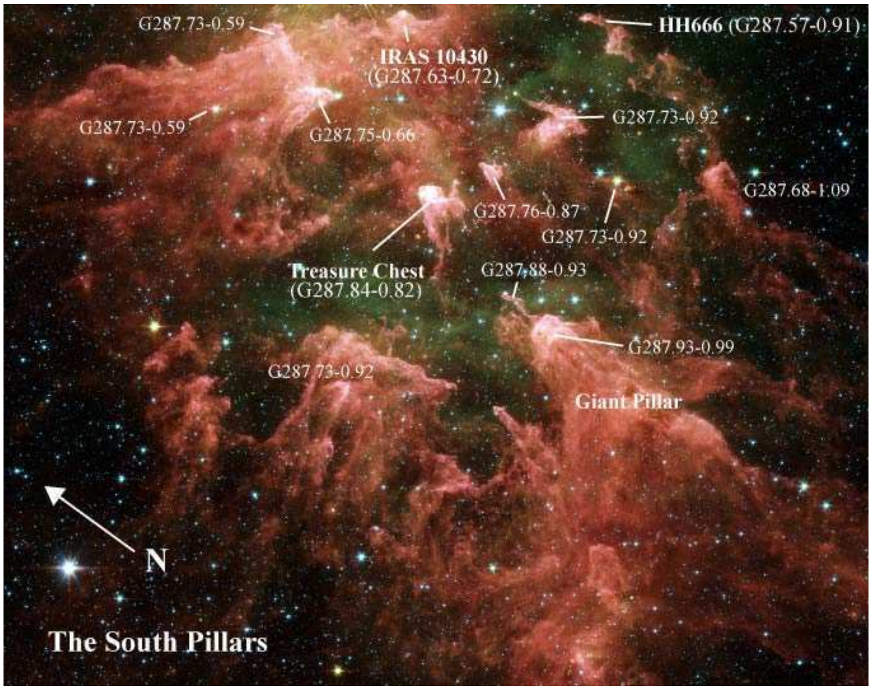

Figure 1.3: Spitzer/IRAC image of the South Pillars (Smith & Brooks, 2008).

Since then, it has become the main focus for studies and research, investigating ongoing and triggered star formation in Carina. Figure 1.4 shows an image in [S II] in which we can perceive the location of the stellar clusters Tr 14, Tr 16, Bochum 10 and Bochum 11, plus 3 WNH massive stars and $\eta$ Car. Smith et al. (2010b) and Povich et al. (2011) report several new young stellar objects (YSOs) in the South Nebulae based on IR observations. Some examples of star forming activity in the South Pillars region are the following (Smith & Brooks, 2008):

1. **IRAS 10430-5931** ($\alpha = 10^h45^m01.1^s$, $\delta = 59°47'06''$ ): A study of this embedded IR source by Megeath et al. (1996a) provided the first strong evidence that active star formation was still happening in the Carina Nebula. This source is embedded in a bright-rimmed globule at the inner edge of the dark obscuring dust lane that bisects the Carina Nebula, and points toward $\eta$ Car. This globule has a luminosity of roughly $10^4\ L_\odot$ with $\sim 70\ M_\odot$ of gas, possibly containing several embedded point sources.

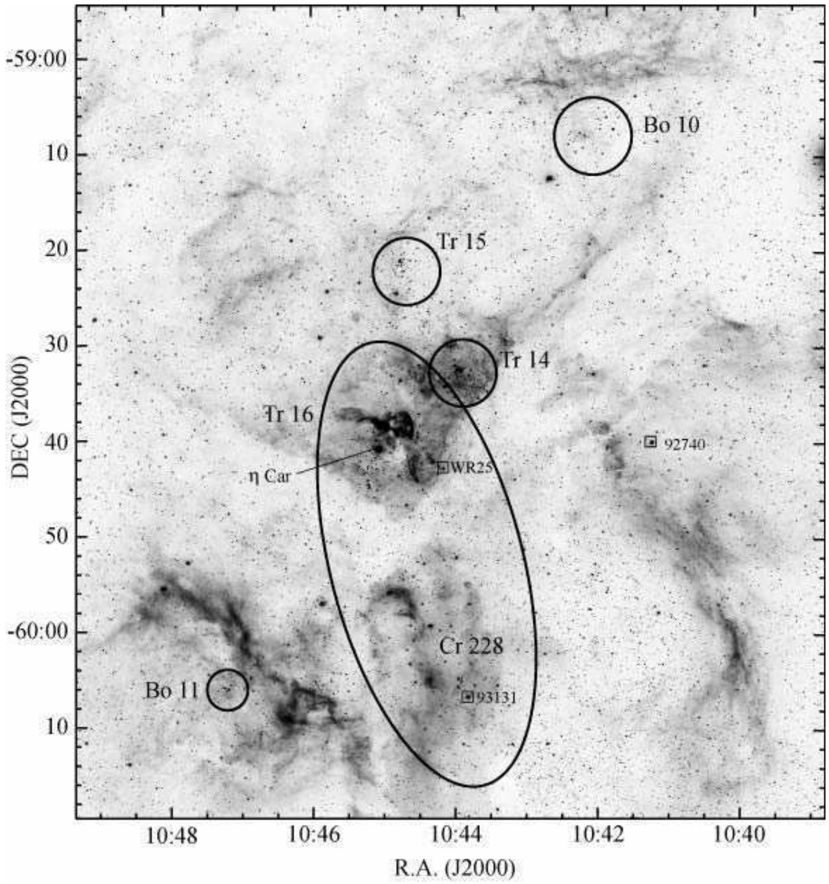

Figure 1.4: A [S II] image of the Carina Nebula identifying the approximate locations of the star clusters: Trumpler 14, 15, and 16, and Bochum 10 and 11. Note that Collinder 228 is generally considered to be part of Tr 16, but these appear as two clusters on the sky because they are divided by an obscuring dust lane. The location of Carinae is given, and the three WNH stars are identified with small squares: WR25 (HD 93162), HD 93131, and HD 92740. The CTIO Schmidt image is from Smith et al. (2004).

2. **HH 666 - The Axis of Evil**: One definitive signpost of active star formation is the presence of protostellar outflows, called Herbig-Haro jets, that get out from a molecular cloud core were young embedded stars are actively accreting material from their circumstellar disk. The first protostellar outflow to be identified in Carina is HH 666, dubbed as the “Axis of Evil”. This is a remarkable straight, several parsec-long bipolar jet emanating from a molecular globule G287.57-0.91 ($\alpha = 10^h 43^m 51.3^s$, $\delta = -59°55'21.2''$) in the South Pillars region. The embedded source is likely to be an intermediate luminosity ($\sim 200\ L_\odot$) Class I protostar called HH 666 IRS. This jet was identified on ground-based images, and was seen because it is the most spectacular jet in the region, and one of the longest HH jets known to date (Smith et al., 2004). More recently, 21 HH jets plus 17 candidate jets, ranging in length from 0.005 to 3 pc have been reported, based on H$\alpha$ observations with the Hubble Space Telescope (Smith et al., 2010a).

3. **The Treasure Chest**: In addition to individual young stars embedded within the heads of dust pillars, the South Pillar region also contains young embedded clusters. The brightest and most spectacular of these is the Treasure Chest cluster associated with the dust pillar G287.84-0.82. The most luminous member of this star cluster is the O9.5 V star CPD-59°2661 ($\alpha = 10^h\ 45^m\ 53.7^s$, $\delta = -59^\circ\ 57'\ 04''$). It was found that this embedded cluster was very young, with a likely age less than 0.1 Myr (Smith et al., 2005).

4. **The Giant Pillar**: Among the South Pillars, the largest one is a giant dust pillar more than 25 pc across that points toward $\eta$ Car (Smith et al., 2000). Many smaller dust pillars, more typical of those seen in other HII regions, are seen to sprout from this one giant pillar, which also contains several embedded IR sources. Examples of these sources are G287.93-0.99 ($\alpha = 10^h 45^m 56.1^s$, $\delta = -60^\circ 08' 50''$) and G287.88-0.93 ($\alpha = 10^h 46^m 00.9^s$, $\delta = -60^\circ 05' 12''$). This giant pillar is probably the remains of a GMC core that is being shredded by feedback from the stars in Tr 16.

In addition to these, there are many others sites of ongoing star formation in the South Pillars region and around the Carina Nebula.

However, a lack of information in this region at millimeter wavelengths still remains. **To obtain stellar information of the most embeeded stars and dust cores, and analyze the YSO diversity at $\eta$ Car South Pillar region based on IR and millimeter observations are the aims of this Master's thesis.** Given the singular properties of this star forming region, it is very useful to study the different evolutionary stages of early massive star formation, both individually and collectively, and compare with other star-forming regions.

## 1.4 Overview of the Thesis

A description of the chapter contents is summarized below:

- **Chapter 2. Infrared Catalogs.** Here will be described how the IR catalogs used to study the South Pillars region were obtained. It will be defined a box that delimit the study region, and a program to find matches between these catalogs to end with a big IR catalog.

- **Chapter 3. Millimeter data.** It presents in first place the description and importance in this thesis of the millimeter data. Then, it describes the steps used to build the millimeter map, obtain the sources flux, together with some simulations that show the quality of data reduction. Based on the results of these simulations a subsample of millimeter sources will be selected lying in the box defined in the last chapter to construct the final catalog of embedded millimeter sources with IR counterparts in the previous big IR catalog.

- **Chapter 4. YSO classification.** Here a Lada (1987) classification of young stellar objects (YSO) is used, and they are represented in color-color and color-magnitude IR diagrams. Special attention is paid for millimeter sources with 24 $\mu$m counterparts in the final catalog. After a visual inspection of these YSO candidates, the spatial distribution of all types of YSOs with millimeter counterpart is presented.

- **Chapter 5. Spectral Energy Distributions: Theory and Results.** Millimeter sources with IR counterpart (YSO candidates) are plotted as Spectral Energy Distributions (SEDs) and fitted with models from Robitaille et al. (2007). The physical parameters that can be obtained from these fits roughly describe the YSOs in the Pillars region. Millimeter data are very helpful to constrain the best models. Also, a discussion about the validity of Lada classification in intermediate and high mass stars is included.

- **Chapter 6. Millimeter cores.** This chapter deals with the millimeter sources that do not have counterparts in the big IR catalog (starless cores). A discussion on classification of protostellar and prestellar cores is treated. Also, the dust masses and densities of these cores, as well as their spatial distribution are presented.

- **Chapter 7. Global view of the South Pillars region.** A description of the whole region is presented by discussing the YSO content in subregions and isolated sources, including all information available in the previous chapters and other publications.

- **Chapter 8. Main conclusions and future work.** In the last chapter, a summary of the conclusions of this thesis and a brief comment about the future work is given.

# Chapter 2

# Infrared Catalogs

## 2.1 Introduction

Since the YSOs are embedded in their parent clouds, it is reasonable to search for infrared (IR) data, in order to obtain the most accurate information from their Spectral Energy Distribution (SED) fittings. The search of surveys at IR wavelengths was made such as they fulfill the following requirements:

1. Include the complete area of our study (see Fig. 1.2)
2. The spatial resolution of maps being of 18 arcsec ($\sim$30 arcsec from millimeter observations, see Chapter 3) or better
3. Positional accuracy of few (1-10) arcsec to get the good match between catalogs
4. Photometry accuracy $\lesssim$ 10%
5. Public access availability

Under these considerations, 5 IR catalogs were selected covering a range of $\lambda$ from $1.2 - 24$ $\mu$m.

## 2.2 Origin of each IR Catalog

Data in catalogs from the surveys are listed in Table 2.1, and were obtained as follows. The IRAC$-$2MASS catalog was obtained from Smith et al. (2010b). MSX and AKARI catalogs were obtained from the IPAC web page: *http:// irsa.ipac.caltech.edu/*, by using the IRSA Services of Gator Catalog Query. From AKARI public data base, the Akari/IRC Point Source Catalog was chosen, while for MSX Public Data Base, the Midcourse Space Experiment (MSXC6) was chosen. For both, MSX and AKARI, the used spatial constraints were: *Coordinate or Object Name*: $\alpha = 10^h46^m48.667^s$ and $\delta = -60^\circ08'47.66''$, plus using a *Box* equal to 4400 arcsec (1.2 degrees).

Table 2.1: List of IR catalogs used in this thesis.

| **Survey Name** | **Spatial resolution** | **Positional accuracy** | **Photometry accuracy** |
|---|---|---|---|
| 2MASS[a] | 4.00” | 0.5” | 5% [b] , 10% [c] |
| AKARI[d] | 9.36” | 0.3” | 2-3% |
| MSX[e] | 18.00” | 2.0” | 5% (A), 3% (C),<br>4% (D), 6% (E) |
| IRAC[f] | 2.00” | 0.2” | 3%, all channels |
| MIPS[g] | 6.00” | 1.0” | 6% |

---

[a] Two Micron All Sky Survey (Skrutskie et al., 2006)

[b] Unconfused point sources

[c] Unconfused extended sources

[d] The Japanese IR Astronomy Satellite (Murakami et al., 2007)

[e] The Midcourse Space Experiment (Mill et al., 1994)

[f] The Infrared Array Camera onboard *Spitzer* Space Telescope (Fazio et al., 2004)

[g] The Multiband Imaging Photometer for the SIRTF (Rieke et al., 2004) also onboard *Spitzer* Space Telescope

The MIPS catalog was built from images of $\eta$ Car obtained from the Spitzer Heritage Archive at the web page *http://irsa.ipac.caltech.edu/applications/Spitzer/SHA/*. A *Radius* of 500 arcsec was used as a spatial constraint to search for Individual Data Products. The Post-BCD MIPS scan results in the area centered in $\eta$ Car position, showed observations by several programs.

Table 2.2: Bands and wavelengths of the selected IR catalogs.

| **Band** | **Wavelength** | **Survey** |
|---|---|---|
| J | $1.25$ $\mu$m | 2MASS |
| H | $1.65$ $\mu$m | 2MASS |
| K | $2.2$ $\mu$m | 2MASS |
| I1 | $3.6$ $\mu$m | IRAC |
| I2 | $4.5$ $\mu$m | IRAC |
| I3 | $5.8$ $\mu$m | IRAC |
| I4 | $8.0$ $\mu$m | IRAC |
| S9W | $9.0$ $\mu$m | AKARI |
| L18W | $18.0$ $\mu$m | AKARI |
| A | $8.28$ $\mu$m | MSX |
| C | $12.13$ $\mu$m | MSX |
| D | $14.65$ $\mu$m | MSX |
| E | $21.34$ $\mu$m | MSX |
| MIPS-24 | $24.0$ $\mu$m | MIPS |
| - | 1.1 mm | AzTEC |

The best Astronomical Observation Requests (AORs) that covered the southern Carina nebula at 24$\mu$m, were the following: *Eta Car South Map Short (AOR key: 23787264)*, *Eta Car West Map1 Short (AOR Key: 23788800)* and *Eta Car West Map2 Short (AOR key:23787520)*, all these AORs are from the program MIPSCAR/30848, whose PI is Nathan Smith. The mosaic image was produced using the standard software MOPEX. The photometry was made using an application called PhotVis on March 2011, but a paper with the photometry catalog was published in May (Povich et al., 2011) using APEX. To get the MIPS-24um aperture photometry on the processed mosaic, the IDL package PhotVis v1.10 (e.g. Gutermuth et al., 2008) was used. The parameters used as an input in PhotVis were:

1. **Aperture radius:** 2.86 pix (7.15 arcsec)
2. **Inner sky annulus:** 6.16 pix (20.40 arcsec)
3. **Outer sky annulus:** 13.06 pix (32.65 arcsec)
4. **Photons per Analogue-to-Digital Unit:** 1
5. **Zero point:** 14.60 mag

PhotVis has the capability to automatically find sources with these parameters, and friendly include or exclude sources to the final list, accordingly with their nature after a review by eye is done in each mosaic section. In this way, a total of 5696 sources were recovered. This number will be smaller in the area of study (see Section 2.3). Then, an aperture correction of *1.467* was applied to the photometric values. This correction value was obtained as the fraction to complete the 100% source flux from the mosaic PSF graph as it is recommended to be estimated in the MIPS instrument documentation page: *http://irsa.ipac.caltech.edu/data/SPITZER/docs/mips/mipsinstrumenthandbook/50/*.

The bands and their respective wavelengths taken from each survey are listed in Table 2.2. The treatment for the 1.1 millimeter data will be explained in Chapter 3.

## 2.3 Throw the big IR catalog: matching data

Data used from the above catalogs are the following: the name of the sources, its position ($\alpha$ and $\delta$) and its fluxes or magnitudes along with their respective uncertainties in each wavelength. To process the data for each catalog, a program called Tool for Operations on Catalogs And Tables (TOPCAT, Taylor, 2005) was employed. TOPCAT is an interactive graphical viewer and editor for tabular data and provides a lot of facilities that astronomers need for analysis and manipulation of source catalogs and other tables. It understands a number of different astronomical formats (including FITS, IPAC and VOTable) and offers a variety of ways to view and analyze tables, in particular, the tool used to match and join tables by using flexible matching algorithms. Table data and metadata can be edited and the resulting modified table can be written out in a wide range of output formats. These features were useful in processing the data from the obtained catalogs. Installation of TOPCAT in a Linux Operative System is simple, go to the page *http://www.star.bris.ac.uk/~mbt/topcat/* and in the section *Obtaining TOPCAT* download the jar archive called *topcat-full.jar*. Its necessary to have installed JAVA 1.5 or higher in order to run TOPCAT. Then, open a terminal in Linux, go to the directory were the jar file is and write the following command: *java -jar topcat-full.jar*. This should successfully open the program.

First, is necessary to delimit our study region based in the map of 1.1 mm avoiding the position of $\eta$ Car, by using a program build in IDL[1] which defines a box. The coordinates of the region vertices of this box are shown in Table. 2.3, which is at a distance of $\sim$3 arcmin from $\eta$ Car. The aim of the program is to know how many sources of each catalog fall within this box and write an output file for each catalog read, which will contain these sources together with their data above mentioned. The program also writes a .reg file that can be read by the program DS9 to check if the sources obtained really are within the box.

After obtaining these “new” catalogs, the second step consist to read them with the program TOPCAT, by going to *File* → *Load Table*. A new window appears, and to search the catalog, is necessary to click on the button *Filestore Browse* and search the catalog to use. Depending on the format of each catalog to study, the program must be adjusted to read them. So, before opening a catalog, it is necessary to change the Table Format to ASCII so the program can read the table. The same procedure is repeated to open all the catalogs. To display the tables of these new catalogs in TOPCAT, one can go to *Views* → *Table Data*.

Table 2.3: Coordinates of the box which contains the studied South Pillars of Carina nebula based on AzTEC map coverage and avoiding the bright star $\eta$ Car.

| **Corner** | $\boldsymbol{\alpha}$ | $\boldsymbol{\delta}$ |
|---|---|---|
| 1 | $10^h41^m02.52$ | $-60°10'48.07''$ |
| 2 | $10^h46^m37.69$ | $-59°26'55.32''$ |
| 3 | $10^h52^m27.22$ | $-60°06'12.60''$ |
| 4 | $10^h48^m08.32$ | $-60°55'36.23''$ |

The third step is to know how many sources between two o more catalogs have counterpart, for that the matching tool of TOPCAT: *Match Tables* is used, which can be accessed by going to *Joins* and selecting one of the options to make the match depending on the number of catalogs to be compared. TOPCAT can do a match between 2, 3, 4 and 5 tables at the same time based on the position of the sources of the catalog, specifying the columns in which are right ascension and declination in the table together with their units, and using a given tolerance (*Max Error*). That is, give a certain error based in the source position in which the program will search if a source in one catalog has counterpart in other catalog or not. This tool can export the results of the comparison by writing in a new table that can have just the sources with counterpart, or

---

[1] A version of this program, *truebox.pro*, is available in the electronic version of this thesis.

writing in the table the sources with counterpart together with the sources that do not have counterpart.

*Match Tables* was used to do a quadruple match between the “new” catalogs of IRAC-2MASS, AKARI, MSX and MIPS. The *Sky algorythm* was used (based in $\alpha$ and $\delta$ values) together with a *Max Error* equal to 3 arcsec because the highest error in position of all these catalogs corresponds to the AKARI data. Also, it was used in the part of *Output Rows* the option *Shows All Rows*, in this way, the resulting table will contain all the sources with counterparts and all the sources without counterparts plus an extra column that indicates the separation between the matched sources. After doing this operation, this table was saved in ASCII format since it will be used later together with the 1.1 mm catalog (see Section 3.5).

In the same way, it was built another similar big IR catalog, however, this one has data in magnitudes instead of fluxes of IRAC-2MASS, MIPS, AKARI and MSX data. The first two catalogs have data of the sources in magnitudes, however the last two catalogs have data only in fluxes and it was necessary to make the conversion. For that, the following equation was used:

$$m - m_0 = -2.5 \log \left( \frac{F}{F_0} \right)$$

where $F$ represents the fluxes for each one of the sources in the catalogs, and $F_0$ is the zero flux for each band of AKARI and MIPS. Taking $m_0 = 0$, the magnitudes of the sources are calculated directly. The values for the zero fluxes of MSX were taken from Sjouwerman et al. (2009), whereas the zero fluxes of AKARI were obtained fromTakita et al. (2010), these values are shown in Table 2.4. An additional modification to the box-limiting program was added to calculate the magnitudes for the sources and their uncertainties by including the above equation and applying propagation of errors. In the end, two IR catalogs were built, one which contains flux values and the other one with magnitude values. They are available in the electronic version of this thesis in INAOE’s library.

Table 2.4: Zero Fluxes for A, C, D and E bands of MSX catalog, and 9 and 18 $\mu$m of AKARI catalog.

| **Band and survey** | **Zero Flux (Jy)** |
|---|---:|
| A | 58.49 |
| C | 26.51 |
| D | 18.29 |
| E | 8.80 |
| 9 $\mu m$ | 56.26 |
| 18 $\mu m$ | 12.00 |

# Chapter 3

# Millimeter data

## 3.1 Introduction

Studies in millimeter wavelengths are an important part in astrophysics, since the applications and utilities of data involve the understanding of several important phenomena in astronomy. For this thesis, the application of the millimeter data to describe and explain the processes of star formation in our Galaxy is of vital importance. Stars form within the dense regions of giant molecular clouds (GMC) within the galaxies. High spatial resolution measurements are required to describe the dynamics within the molecular clouds that set the initial conditions for protostellar formation and evolution. Soon, the Large Millimeter Telescope (LMT) will allow us to investigate the many scales and processes related to star formation in molecular clouds within our Galaxy. Accurate descriptions of the dynamics of molecular clouds are essential to our understanding of the star formation process, both theoretical and observational.

Two distinct modes of star formation have been identified. In one, is supposed that the star formation occurs within small (0.1 pc), low mass ($1-10\ M_\odot$), dense (10 000 molecules per cm$^{-3}$), isolated cores that typically form a single star with low to moderate mass. The other mode describes dense regions from which newborn stellar clusters emerge, they are larger ($0.5-1$ pc), more massive (1 000$-$10 000 $M_\odot$), denser (1 million molecules per cm$^{-3}$), and more inhomogeneous. Such regions have the capacity to produce 100 to 1,000 stars and are practically the only sites of massive star formation, besides these regions are often associated with compact or evolved HII regions (Irvine et al., 2005). However, there are few nearby examples that would provide insights into their origins within giant molecular clouds and the complex interactions that must occur between embedded protostellar objects. The maps that will be produced with the AzTEC camera once assembled in the LMT, will allow us to reveal the column density distribution of material and identify protostellar objects within the massive cores, complementing the mid-IR measurements from the Spitzer Space Telescope.

The formation of a star starts from the gravitational collapse of dense gas within a molecular cloud. Protostars studies can give useful knowledge of the physics and the initial conditions required for star formation and protostellar evolution.

Millimeter data in southern nebula of stellar formation in the star $\eta$ Car were obtained using the AzTEC continuum camera (Wilson et al., 2008), as a visitor instrument on the Atacama Submillimeter Telescope Experiment (ASTE, Kohno, 2005). AzTEC is a large-format bolometer array camera developed at the University of Massachusetts (UMASS) Amherst, and will serve as one of the first facility instruments of the Large Millimeter Telescope (LMT/GTM, Pérez-Grovas et al., 2006; Hughes et al., 2010).

AzTEC's detector array is composed of 144 silicon nitride micromesh bolometers with a bandpass defined through a series of changeable filters and coupling optics. The Carina region data were obtained on June 23rd 2007, with a total integration time of 90 minutes.

## 3.2 Processing data

Data from $\eta$ Car region were processed with the use of tools developed specifically for the AzTEC camera (Wilson et al., 2008). Grant Wilson is the Principal Investigator that has been working in the AzTEC camera in UMASS, and together with his group of collaborators, have developed the software (programs, packages and libraries) used to reduce and analyze the observed data with the AzTEC camera (see Scott et al., 2008). These programs were written in the programming language Interactive Data Language (IDL), so it is necessary to have installed IDL (version 7 or higher) preferentially in a Linux distribution, for a better understanding of the following steps. The millimeter data were provided by David Hughes and observed by his students from the group "Cosmología e Instrumentación Milimétrica" (Cosmology and Millimeter Instrumentation) at INAOE. They made remote observations at ASTE together with other institutions of a larger program that included the Carina Region.

An appropriate setup in order to start the data analysis includes the following lines in an archive called *.tsrch*.

```
#------------------------------------------------ # IDL
setenv IDL_DIR /usr/local/itt/idl71
setenv IDL_PATH \+$IDL_DIR/lib
alias idl $IDL_DIR/bin/idl           # generic IDL version
alias idlde $IDL_DIR/bin/idlde   # IDL GUI Development Environment
setenv AZTEC_IDL_PATH /usr/local/itt/idl71/lib/aztec_idl_utilities
```

Here, the first line represents the path where IDL is installed, the second one is the path where the libraries of IDL are, the third and fourth lines represent where the generic version and the GUI Development Environment of IDL are respectively, and finally, the fifth line tell us the location of the AzTEC libraries. To start working, it is necessary to change the shell in the Linux terminals to tcsh in order to recognize where the AzTEC libraries are. This change is done in the user settings option of the Linux distribution. If the shell is not shown there, it will be necessary to install it. After running IDL, the first line to write is: *@aztec_startup*, that will make that IDL recognizes the libraries to build the map and the millimeter data reduction.

Millimeter data of $\eta$ Car are stored in 7 netCDF (.nc) files. This format was developed by the Unidata Program Center at the University Corporation for Atmospheric Research in Boulder, Colorado. The basic building blocks of the netCDF files are variables, attributes and dimensions (Gumley, 2002):

- Variables are scalars or multidimensional arrays. The IDL data types supported by netCDF files are string, byte, int, long, float and double.
- Attributes contain supplementary information about a single variable or an entire file. Attributes that contain information about a single variable (e.g., units, valid range, scaling factor) are known as variable attributes. Attributes may be scalars or one-dimensional arrays, and the supported data types are string, byte, int, long, float or double.
- Dimensions are long scalars that record the size of one or more variables

## 3.3 Building the AzTEC map

Information from the netCDF files of $\eta$ Car to build the map is used calling an IDL program called *full_nk_pipeline*[1] . This script takes a data set of netCDF files and reduces it completely to make the map. It is divided into three parts, and they will be described briefly together with the used keywords.

The goal of the first part in *full_nk_pipeline* is to indicate the location of the directory where the netCDF files are, writing the path in the variable *working_dir*. The second part seeks to determine which steps of the reduction process are need to be performed ($<$ keyword $>$ = 1); these steps are listed in the order that they will be made. If we want all steps to be made in one run, it is necessary to put all the keywords equal to 1. Depending of the computer used to do this steps, the full process can take a long time to produce the map. So, it is possible limit this script to perform only a subsection of the reduction, choosing some steps/keywords equal to 1 and the rest equal to 0, and later run again the program with the steps left equal to 1 and the steps done equal to 0 to finish the work.

The last part of the program deals with some keywords related with how the millimeter data of the region were obtained. It is necessary to be careful here since a bad keyword could produce a useless map and lots of wasted hours in the computer.

---

[1] All the programs used to do the reduction and analysis of millimeter data are available upon request to the head of the AzTEC instrument, Grant Wilson, *wilson@astro.umass.edu*

Table 3.1: Keyword values used in *full_nk_pipeline* program.

| Keyword | Description | Used value |
|---|---|---|
| time_chunk | Used to set the type of observation used to make the netCDF files [a] | 0 |
| despike | Useful for detect weak sources and blank fields | 7 |
| lowpass_freq | Depends of the telescope used in the observations[b] | 12 |
| cut_std | Useful to find weak point sources | 2.5 |
| mastergrid | Use to indicate the center coordinates of the map | [160.500000d, -59.416667d] |
| pixelsize | Depends of the telescope used in the observations[c] | 6.d |
| title | Put a title in the graphs that appear in the process of make the map | Eta Car |
| beam_fwhm | The beam size used in the observations | 30 |
| coverage_threshold | Type of coverage cut made just for plotting, depends on the type of the observed object | 0.75 |

---

[a] Rastering or Lissajous observations

[b] 12 for ASTE and 16 for JCMT

[c] $\leq 6$ for ASTE and $\leq 3$ for JCMT

Table 3.1 shows the list of these parameters and the values used to make the map. This script was ran 3 times to see which parameters are the best, not only for making the map, but also to know how many sources was possible to detect using the program *aztec_source_locate* (explained below) in each of the obtained maps. The first run of the script was made using a *time_chunk=0* and a *coverage_threshold=0.5*, the second one was made using a *time_chunk=10* and a *coverage_threshold=0.75*, and finally the third one was made with a *time_chunk=0* and a *coverage_threshold=0.75*. The other parameters were left equal in all the runs (See Table 3.2).

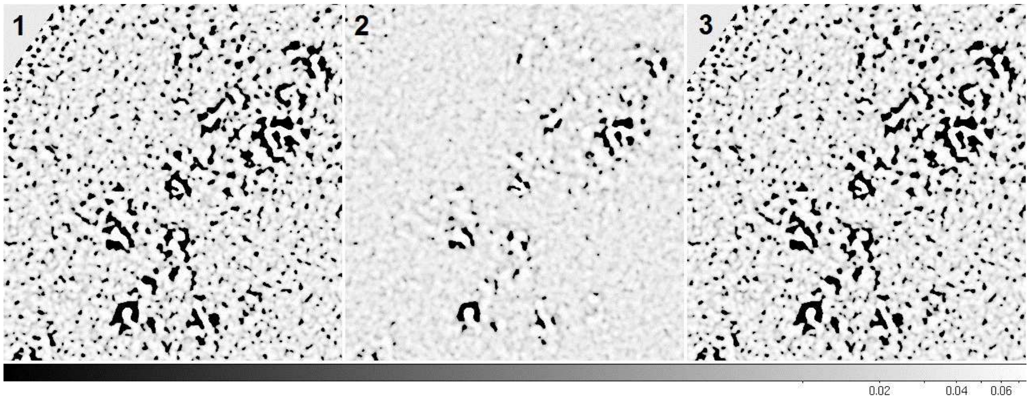

Figure 3.1: A snapshot of the three millimeter maps created, used parameters are listed in Table 3.2.

The better compromise between map quality and number of detected sources was **map 3**. The reasons are because it has more sources that the other two catalogs and besides, after investigate the way in which the netCDF files of $\eta$ Car were obtained, the used parameters to build this map were more accurate to reflect this that in the other two maps. Figure 3.1 displays a small region in the three maps, showing different textures.

Table 3.2: Time chunk and coverage cut used in each run of aztec_source_locate. Also, the total number of sources obtained is listed. The map in bold was used in this work.

| **Map** | **Time chunk** | **Coverage cut** | **Sources in the map** |
|---|---|---|---|
| 1 | 10 | 0.75 | 354 |
| 2 | 0 | 0.75 | 333 |
| **3** | **0** | **0.50** | **372** |

The program *aztec_source_locate* uses the sav files from the above maps, and is called by the batch *main0*[2] , which also includes the list of keywords used, as well as the elected values, and to be run in IDL must be written @main0. The keyword values used to find sources are described in Table 3.3. The resulting catalog from running main0 is written in the same working directory, and will have the name *EtaCarina_v 3.00000_sources.txt* by default and the sources will be ordered by S/N.

Table 3.3: Keyword values used in aztec_source_locate program.

| **Keyword** | **Description** | **Used value** |
|---|---|---|
| sourcename | The name of the studied object. | 'Eta Carina' |
| signal_map | The name and location of the map obtained after run full_pipeline_nk.pro. | 'signal_wfilt.sav' |
| source_sigma | Number of sigmas that will be used to consider a source [a] | 3 |
| coverage_cut | The fraction considered as maximum coverage [b] | |
| beamsize | Same that beam_fwhm. | |
| centroid_sources | Get centroid position of source using flux$^2$ weighting of the pixel positions within a window [c] | 1.0 |
| suppress_graphics | Set this to prevent any plots from appearing in the process | |
| single_source_window | This is the radius employed to mask out around a found source. [d] | 15 |

[a] For example, source_sigma=3 means any pixels over 3 sigma are flagged as a potential source.

[b] It is the same value that the coverage_threshold used in the previous step.

[c] By default (setting centroid sources to 1 or /centroid_sources), window is any pixel that falls within beamsize/2 of the original (brightest pixel) source position.

[d] That specified radius don't allow any other 'sources' to be identified within this radius, set in arcsec

---

[2] All the scripts mentioned in this chapter are available in the electronic version of this thesis

The total number of sources in the 1.1 mm AzTEC map chosen (map 3) is 372, but only 118 lie in the southern region under our study (result of the program *truebox.pro* used in Chapter 2.3). The catalog includes the following columns:

i) AzTEC number, which is not consecutive since some sources were located in the northern region
ii) Coordinates in degrees
iii) Signal to Noise ratio, which gives the descendant order of sources
iv) Flux in Janskys
v) rms noise in Janskys.

The catalog of the 118/372 southern sources that lie in our region of interest is given in Table 3.4. Note that the Signal to Noise (S/N) ranges from 3 to about 50, but only 52 sources have S/N greater than 4. The resulting map is shown in Fig. 3.2 together with the 24 and 8 $\mu$m maps.

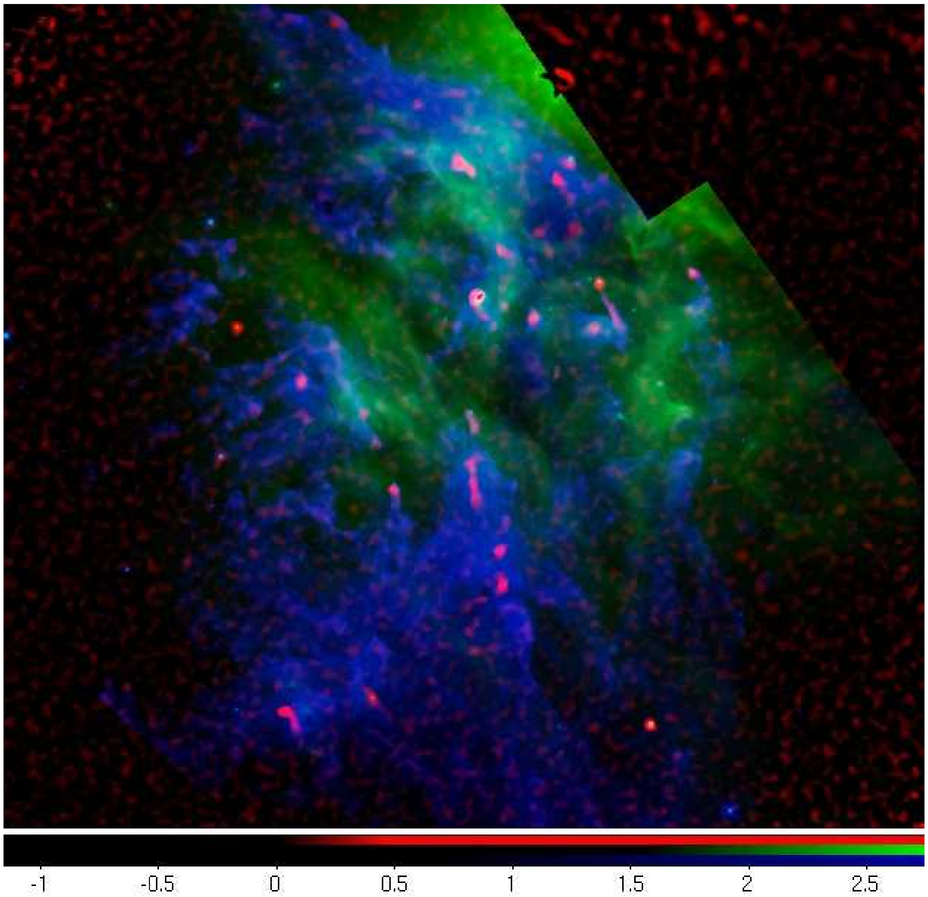

Figure 3.2: RGB image of the studied region. Colors are the following: Red=1.1mm, Green=24 $\mu$m and Blue=8 $\mu$m. Red map is the same as the bold one in Table 3.2.

Table 3.4: List of millimeter sources found within Carina South Pillars.

| **# Source** | $\alpha$ | $\delta$ | **S/N** | **Flux[Jy]** | **Noise[Jy]** |
|---|---|---|---|---|---|
| 002 | 161.481634 | -59.947967 | 47.644817 | 2.289044 | 0.048045 |
| 004 | 161.959481 | -60.440530 | 24.415546 | 1.224156 | 0.050139 |
| 006 | 161.517174 | -59.790932 | 19.989909 | 1.006852 | 0.050369 |
| 015 | 161.434444 | -60.254904 | 14.189391 | 0.656227 | 0.046249 |
| 017 | 161.074862 | -60.463775 | 13.502830 | 0.696659 | 0.051594 |
| 022 | 161.288547 | -59.810820 | 12.743529 | 0.581367 | 0.045622 |
| 023 | 161.188870 | -59.934953 | 12.465323 | 0.635250 | 0.050962 |
| 024 | 161.346224 | -59.975510 | 12.310188 | 0.575589 | 0.046758 |
| 026 | 160.965573 | -59.924210 | 12.055712 | 0.565226 | 0.046885 |
| 027 | 161.494050 | -59.796550 | 12.043900 | 0.607990 | 0.050482 |
| 030 | 161.255455 | -59.791310 | 11.021674 | 0.524419 | 0.047582 |
| 031 | 161.905189 | -60.045891 | 10.998934 | 0.577986 | 0.052550 |
| 033 | 161.686798 | -60.178243 | 10.779067 | 0.540437 | 0.050139 |
| 034 | 161.423224 | -59.893635 | 10.593238 | 0.547057 | 0.051643 |
| 035 | 162.055796 | -59.980800 | 10.123555 | 0.495533 | 0.048949 |
| 040 | 161.495287 | -60.172835 | 9.593107 | 0.512640 | 0.053439 |
| 042 | 161.428328 | -60.296518 | 9.395481 | 0.477158 | 0.050787 |
| 044 | 161.501439 | -60.151163 | 8.867200 | 0.459082 | 0.051774 |
| 046 | 161.491836 | -60.189443 | 8.657636 | 0.441320 | 0.050976 |
| 048 | 161.199722 | -59.989747 | 8.360591 | 0.399036 | 0.047729 |
| 052 | 161.749472 | -60.425733 | 8.111751 | 0.394885 | 0.048681 |
| 057 | 161.149626 | -59.976777 | 7.246775 | 0.403086 | 0.055624 |
| 060 | 161.938934 | -60.458594 | 7.101871 | 0.354184 | 0.049873 |
| 063 | 161.330243 | -59.873811 | 6.908258 | 0.325157 | 0.047069 |
| 065 | 161.159569 | -59.965173 | 6.670978 | 0.343257 | 0.051456 |
| 066 | 161.489942 | -60.106246 | 6.632764 | 0.312825 | 0.047164 |
| 070 | 161.756363 | -60.087095 | 6.379595 | 0.339762 | 0.053258 |
| 071 | 161.416249 | -59.961585 | 6.361974 | 0.342833 | 0.053889 |
| 074 | 161.611430 | -59.718756 | 6.234504 | 0.302556 | 0.048530 |
| 075 | 161.496316 | -60.099497 | 6.185467 | 0.306112 | 0.049490 |
| 079 | 161.479433 | -60.311384 | 6.071794 | 0.269944 | 0.044460 |
| 081 | 161.462119 | -59.973086 | 5.974871 | 0.306952 | 0.051375 |
| 083 | 161.823884 | -60.005040 | 5.700870 | 0.291123 | 0.051067 |
| 086 | 161.802097 | -59.618493 | 5.656067 | 0.268235 | 0.047425 |
| 087 | 161.497976 | -60.371310 | 5.540802 | 0.279076 | 0.050368 |
| 089 | 161.331805 | -59.783986 | 5.499718 | 0.278612 | 0.050660 |
| 091 | 161.476179 | -59.750954 | 5.431793 | 0.275519 | 0.050724 |
| 095 | 161.513783 | -60.349404 | 5.273736 | 0.244256 | 0.046316 |
| 098 | 161.250059 | -59.869511 | 5.163634 | 0.269154 | 0.052126 |
| 099 | 161.379691 | -59.742276 | 5.120012 | 0.253560 | 0.049524 |

Table 3.4: *Continued.*

| **# Source** | $\alpha$ | $\delta$ | **S/N** | **Flux[Jy]** | **Noise[Jy]** |
|---|---|---|---|---|---|
| 107 | 161.893576 | -60.092570 | 4.948141 | 0.225036 | 0.045480 |
| 112 | 161.730643 | -60.122449 | 4.831942 | 0.243706 | 0.050437 |
| 116 | 161.256492 | -59.829906 | 4.695556 | 0.256832 | 0.054698 |
| 117 | 161.364569 | -59.793609 | 4.695212 | 0.238117 | 0.050716 |
| 119 | 161.419769 | -60.218337 | 4.624337 | 0.212837 | 0.046026 |
| 123 | 161.527554 | -59.704501 | 4.556718 | 0.243617 | 0.053464 |
| 128 | 161.513107 | -60.320931 | 4.515394 | 0.218068 | 0.048295 |
| 130 | 161.409780 | -60.608425 | 4.493481 | 0.212563 | 0.047306 |
| 131 | 160.975971 | -59.967488 | 4.478235 | 0.210714 | 0.047054 |
| 132 | 162.099976 | -60.135371 | 4.467966 | 0.245097 | 0.054857 |
| 135 | 161.638697 | -59.773722 | 4.385043 | 0.222586 | 0.050761 |
| 148 | 161.532860 | -59.984156 | 4.022470 | 0.188993 | 0.046985 |
| 150 | 161.432231 | -60.228391 | 3.996916 | 0.183145 | 0.045822 |
| 151 | 161.418942 | -59.939889 | 3.963289 | 0.200755 | 0.050654 |
| 152 | 161.176325 | -59.806517 | 3.961501 | 0.212724 | 0.053699 |
| 153 | 161.375734 | -60.343897 | 3.946052 | 0.188626 | 0.047802 |
| 157 | 161.914402 | -59.612472 | 3.865042 | 0.199072 | 0.051507 |
| 163 | 162.612161 | -60.140151 | 3.793743 | 0.192943 | 0.050859 |
| 170 | 161.443274 | -59.985005 | 3.727703 | 0.190317 | 0.051055 |
| 172 | 161.693006 | -59.896441 | 3.718606 | 0.182711 | 0.049135 |
| 176 | 162.343059 | -60.408833 | 3.693622 | 0.180378 | 0.048836 |
| 178 | 160.982016 | -59.869435 | 3.659131 | 0.185622 | 0.050729 |
| 181 | 161.308020 | -59.897416 | 3.641061 | 0.184389 | 0.050642 |
| 182 | 162.013645 | -60.079776 | 3.628024 | 0.203921 | 0.056208 |
| 185 | 162.393626 | -60.055934 | 3.612317 | 0.174597 | 0.048335 |
| 190 | 161.278448 | -59.699690 | 3.595087 | 0.196374 | 0.054624 |
| 191 | 160.979165 | -60.147216 | 3.594944 | 0.159265 | 0.044303 |
| 197 | 161.614328 | -60.344848 | 3.545257 | 0.167786 | 0.047328 |
| 205 | 160.777894 | -60.044293 | 3.514098 | 0.172686 | 0.049142 |
| 207 | 162.064818 | -59.885939 | 3.501557 | 0.188321 | 0.053783 |
| 211 | 161.498949 | -59.749590 | 3.469359 | 0.169185 | 0.048766 |
| 222 | 161.293717 | -60.044161 | 3.418575 | 0.170306 | 0.049819 |
| 223 | 161.755182 | -59.689311 | 3.417772 | 0.165428 | 0.048403 |
| 225 | 161.511391 | -59.705886 | 3.412267 | 0.186036 | 0.054520 |
| 227 | 160.547072 | -60.250078 | 3.393588 | 0.202339 | 0.059625 |
| 229 | 161.468867 | -60.291116 | 3.391909 | 0.159559 | 0.047042 |
| 230 | 161.575444 | -59.950701 | 3.389547 | 0.176747 | 0.052145 |
| 237 | 161.024315 | -60.455278 | 3.371694 | 0.153356 | 0.045484 |
| 238 | 160.735793 | -59.963195 | 3.371685 | 0.150593 | 0.044665 |
| 245 | 161.314818 | -60.314220 | 3.340395 | 0.160690 | 0.048106 |

Table 3.4: *Continued.*

| **# Source** | $\alpha$ | $\delta$ | **S/N** | **Flux[Jy]** | **Noise[Jy]** |
|---|---|---|---|---|---|
| 246 | 161.662353 | -60.070002 | 3.337199 | 0.159213 | 0.047709 |
| 249 | 162.188437 | -59.992456 | 3.329181 | 0.153542 | 0.046121 |
| 252 | 161.607242 | -60.407063 | 3.319348 | 0.156070 | 0.047019 |
| 256 | 161.704372 | -60.045787 | 3.302477 | 0.165213 | 0.050028 |
| 262 | 161.257142 | -60.038065 | 3.270494 | 0.161946 | 0.049518 |
| 266 | 161.515856 | -60.279097 | 3.259642 | 0.151536 | 0.046489 |
| 273 | 161.216391 | -60.466160 | 3.236712 | 0.157153 | 0.048554 |
| 275 | 160.509276 | -60.058265 | 3.234291 | 0.161500 | 0.049934 |
| 278 | 161.722500 | -60.442393 | 3.219853 | 0.151460 | 0.047040 |
| 279 | 160.852851 | -60.262789 | 3.212460 | 0.158954 | 0.049481 |
| 283 | 162.122898 | -59.933431 | 3.209497 | 0.158809 | 0.049482 |
| 289 | 161.817896 | -60.018235 | 3.193563 | 0.155624 | 0.048731 |
| 294 | 162.005607 | -60.342924 | 3.182212 | 0.156269 | 0.049108 |
| 298 | 161.814666 | -60.041561 | 3.177452 | 0.151609 | 0.047715 |
| 301 | 161.571749 | -60.365594 | 3.165214 | 0.155428 | 0.049106 |
| 302 | 162.002019 | -60.203005 | 3.163021 | 0.153594 | 0.048560 |
| 308 | 162.149573 | -60.576140 | 3.159974 | 0.150833 | 0.047733 |
| 313 | 161.947687 | -60.017219 | 3.147186 | 0.179414 | 0.057009 |
| 314 | 162.219162 | -60.505486 | 3.144354 | 0.160007 | 0.050888 |
| 317 | 161.156024 | -60.281989 | 3.134797 | 0.143657 | 0.045827 |
| 319 | 162.696575 | -60.145362 | 3.130433 | 0.153830 | 0.049141 |
| 321 | 161.801247 | -59.876788 | 3.127596 | 0.153564 | 0.049100 |
| 323 | 161.318737 | -60.505741 | 3.114306 | 0.147389 | 0.047327 |
| 324 | 162.022266 | -60.045963 | 3.112301 | 0.150897 | 0.048485 |
| 330 | 161.854817 | -60.211602 | 3.090053 | 0.155457 | 0.050309 |
| 331 | 160.883846 | -60.044195 | 3.088910 | 0.142968 | 0.046285 |
| 336 | 161.419080 | -60.320015 | 3.067980 | 0.155441 | 0.050666 |
| 337 | 162.489404 | -59.946517 | 3.067062 | 0.182393 | 0.059469 |
| 342 | 161.332139 | -59.685547 | 3.056722 | 0.148603 | 0.048616 |
| 345 | 161.339365 | -60.491017 | 3.051602 | 0.137775 | 0.045149 |
| 352 | 161.492412 | -59.729439 | 3.033656 | 0.148054 | 0.048805 |
| 353 | 162.389451 | -60.400117 | 3.033095 | 0.141916 | 0.046790 |
| 354 | 161.372330 | -59.813941 | 3.032817 | 0.163558 | 0.053930 |
| 360 | 161.749151 | -59.783839 | 3.017229 | 0.154488 | 0.051203 |
| 363 | 160.623854 | -60.146779 | 3.013232 | 0.156009 | 0.051775 |
| 364 | 161.109183 | -59.780077 | 3.010645 | 0.152435 | 0.050633 |
| 366 | 161.196495 | -59.706415 | 3.009616 | 0.165733 | 0.055068 |
| 371 | 161.717531 | -60.392461 | 3.002314 | 0.150079 | 0.049989 |

## 3.4 Monte Carlo Simulations to Characterize the 1.1 Millimeter Catalog

Once selected the map, is convenient to see and determine various characteristics of the signal map selected and the source identification process via Monte Carlo simulations. The results of the simulations[1] done in this work are the following.

### 3.4.1 False detection rate

A False Detection Rate (FDR) is the number of peaks $> N\sigma$ (S/N) caused purely by noise and therefore appear at locations where there are no real sources (Scott et al., 2008, § 5.2). To run this test, a program *aztec_false_detection_rate.pro* called by a script *main1* is used. This script writes the keyword values to run the program in order to make the simulation. The keywords used are described in Table 3.5. The keywords *centroid_sources*, *single_source_window*, *beamsize* and *suppress_graphics* have the same values that in Table 3.3.

To run this in IDL, is necessary to follow the steps: 1) *@aztec_startup* to read all the aztec libraries, 2) compile the script using *.compile main1*, and 3) run the simulation with *.run main1*. The archive with the catalog sources has a column of Signal to Noise (S/N, see Table 3.4) and this parameter is used in the simulation to give the approximated value of S/N from which the real sources are not contaminated with false detections. The programs were initially designed to find galaxies, however, in our map there are very bright point sources, several of them with S/N $\geq$ 10. The first FDR obtained gave unreasonable results compared with the ones obtained by Scott et al. (2008). We were getting serious overestimates in the false detections using our original noise maps, since the first result gave us approximately 80 false detections in a S/N $= 6$, which does not make sense with the total number of detections in the $\eta$ Car map, while Scott et al. (2008) obtained around 2 false detections above a S/N $= 4$. To avoid this problem, it was necessary to mask some of these bright sources in the noise maps previously obtained, by using an IDL program (masknoise.pro) which was created by David Omar Sánchez[2] . Briefly, the program reads from the millimeter catalog the positions of the sources, and depending of the value of S/N chosen, the sources with that value or higher will be masked. In our case, was chosen a S/N $= 6$. Also, it was necessary to define a radius to mask the sources equal to 120.0 arcsec. Since the FDR test takes the filtered maps obtained in the map creation, it was mandatory that the program reads and masks the sources previously selected. Fig. 3.3 shows a more satisfactory result for the FDR test.

---

[1] The following Monte Carlo simulations have been created to characterize the quality of extragalactic AzTEC observations(Scott et al., 2008) and are part of the AzTEC software

[2] PhD student from the Cosmology and Millimeter Instrumentation group at INAOE

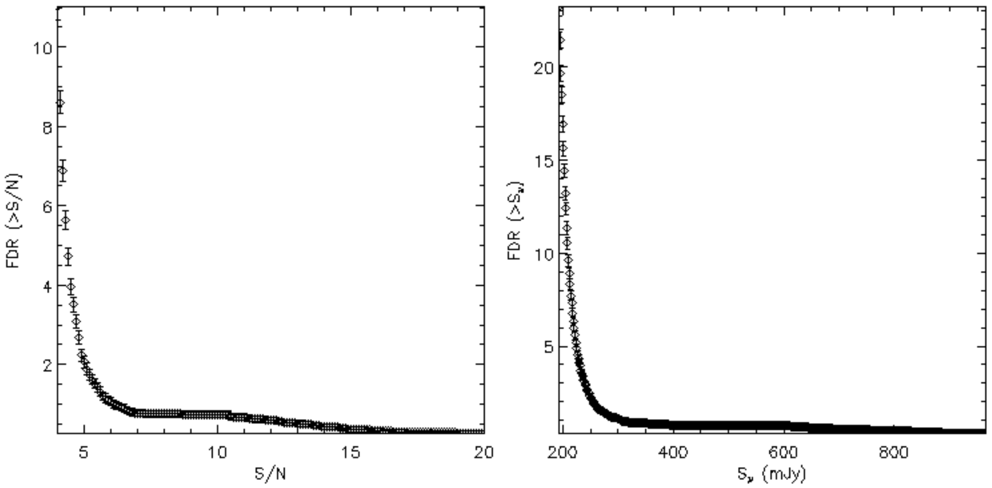

Figure 3.3: Resulting graph from the false detection rate simulation, which gives the number of expected false detections given a S/N (left panel) and a measured source flux (right panel)

The main result is that from a $S/N = 6$ and a $S_\nu = 300$ mJy is detected least one false source. Although a S/N $>$ 6 completely guarantees that the detected sources are real, objects with S/N $>$ 4 also were studied, due that several of them have more than one counterpart in the IR catalogs.

Table 3.5: Keywords and values used in the *AzTEC_false_detection_rate* simulation.

| **Keyword** | **Description** | **Used value** |
|---|---|---|
| source_sigma | The signal to noise threshold to use to search for sources, in arcsec. | 3 |
| coverage_cut | The coverage region to use, same that the previous value | 0.5 |
| title | The title on the plot | 'Eta Carina' |
| output_savfile | The name and location where will be output an IDL saveset | Location of output |
| output_pngfile | The name and location where will be output a pngfile showing the false detection rate | Location of output |
| coadded_noisemaps | The location of an array of noise realizations that have already been created making the map, called with *to_coadd.sav | Location of the files *to_coadd.sav |
| min_s2n | The minimum signal to noise to plot. | 6.0 |
| max_s2n | The maximum signal to noise to plot. | 10.0 |
| bsize_s2n | The binsize of signal to noise bins. | 0.1 |
| bsize_flux | The binsize of flux values to use for bins in mJy | 0.05 |

### 3.4.2 Completeness

The completeness of the map is estimated by injecting sources, one at a time, into the (sparsely populated) real signal map at random positions and checking if they are retrieved by the standard source identification algorithm of the program that will be used (Scott et al., 2008, § 5.3). Adding one source at a time to the real signal map provides a valid estimate of the completeness because:

1. Accounts for the effects of random and confusion noise present in the real map.
2. does not significantly alter the properties of the real map (only one source input at a time)
3. is not dependent on a model of the source population since is necessary for fully simulated data sets using noise maps.

A total of 1000 sources were injected per flux value, ranging from 0.5 to 12 mJy in steps of 0.5 mJy. A source is considered to be recovered if it is detected with S/N $\geq$ 3.5 within 10 arcsec of the input source position. The program used is called *aztec_calc_completeness* and the script used to run this program is named *main2*. The steps to run the program are the same that in the above simulation.

In the same way that the False Detection Rate simulation, the program uses the values of the keywords from the script to run the simulation. These are described in Table 3.6, and the differential completeness as a function of input source flux is shown in Figure 3.4. The main conclusion of this simulation is that from a input flux approximately equal to 300 mJy, all the injected sources are detected in the simulation, thus in our map, sources with an equal or higher flux are well detected.

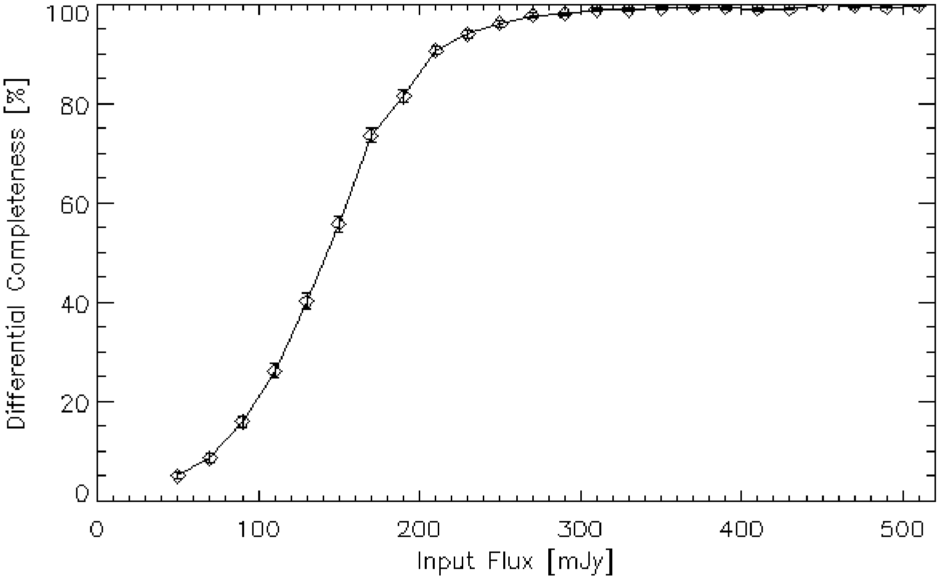

Figure 3.4: Resulting graph in the simulation showing the differential completness versus intrinsic source flux density.

Table 3.6: Keywords and values used in the *AzTEC_completeness* simulation.

| **Keyword** | **Description** | **Used Value** |
|---|---|---|
| min_flux | The minimum flux bin to use in mJy. | 50 |
| max_flux | The maximum flux bin to use in mJy. | 510 |
| binsize_flux | The binsize to use for the flux bins. | 20 |
| nfake | The number of fake sources to insert per flux bin. | 1000 |
| real_source_s2n | The signal to noise threshold for detection of real sources in the map. | 3 |
| recov_s2n | The signal to noise threshold for determining whether an input source was recovered. | 3 |
| recov_radius | The distance from the input source location in which the output source is considered to be recovered in arcsec. | 20 |
| coverage_cut | The percent coverage to use in determining the uniform coverage region in the map. [a] | 0.5 |
| centroid_sources | Used to centroid the source locations, rather than use the pixel value | 1. |
| beamsize | The search radius (in arcsec) used when looking for local max/min (default=18 arcsec), if centroid_ sources is not set. If centroid_sources is set and equal to 1, will use pixels within beamsize/2. | 30 |
| single_source_window | The radius to mask out in determining a single source in arcsec. | 15. |
| output_savfile | The name and location where will be put the sav file after finish the simulation | ’c.sav’ |
| title | The title on the output plot. | ’Eta Car South Reg.’ |
| bayesnc_format | Used to have variables in the output saveset named as expected for use in Bayesian number counts procedure. | 0. |
| noplot | Set this to suppress plot of completeness. | 0. |
| peak_bias | Try to remove bias to peak location in the map | . |

---

[a] Only the uniform coverage region will be considered in the analysis.

### 3.4.3 Positional uncertainty

The above simulation offers a measure of the error on the position of sources identified in the AzTEC map due to effects on random and confusion noise. For the synthetic sources that are recovered, it is possible to calculate the distance between the input and output source positions and to construct the probability $P\,(>D; S/N)$, that an AzTEC source detected with a significance of S/N will be detected outside a distance $D$ of its true position (Scott et al., 2008, $\S$ 5.4). The simulation used to calculate this is called positional uncertainty, and its measurement is not sensitive to the contribution from positional errors (systematic or random) introduced through corrections.

To run this simulation it is necessary to assume Gaussian random pointing errors of 2 arcsec in $\alpha$ and $\delta$, and generate 100 random variates for each recovered source to simulate pointing errors, which are added to the measure output source position. A program called *aztec_positional_uncertainty* was ran by reading the keywords to use in a script called *main3* to run this simulation in IDL with the same procedure. The keywords used in this simulation are explained in Table 3.7.

Table 3.7: Keywords and values used in the *AzTEC_positional_uncertainty_simulation* program.

| **Keyword** | **Description** | **Used Value** |
|---|---|---|
| nsim | The number of random numbers to generate per recovered source [a] | 0. |
| random_xerr | The 1-sig value of random pointing error in right ascension (arcsec). | 0.d |
| random_yerr | The 1-sig value of random pointing error in declination (arcsec). | 0.d |
| dist_binsize | The binsize to use for distance bins (arcsec). | 1.5d |
| s2n_binsize | The binsize to use for signal to noise bins. | 0.25d |
| mns2n | The min value of signal to noise for the histogram. | 4.0d |
| mxs2n | The max value of signal to noise for the histogram. | 12.0d |
| mndist | The min value of distance for the histogram (arcsec). | 0. |
| mxdist | The min value of distance for the histogram (arcsec). | 20. |
| title | The title to appear at the top of the plot | 'Positional Uncertainty' |
| output_savfile | The name and location of the output idl saveset for the simulation. | 'pu.sav' |
| output_pngfile | The name and location of the output png file showing the pointing uncertainty distribution for a few sample signal to noise bins. | 'pu.png' |

---

[a] To simulate random pointing errors

A plot of the positional uncertainty distribution as a function of distance for 4 different S/N bins is shown in Figure 3.5. For all $\geq 4.50\sigma$ (S/N) AzTEC sources detected, the probability that one of them will be detected within a radius of **6 arcsec** of its true position is $\gtrsim$ 80%. In general, all AzTEC sources will have a positional uncertainty of 10 arcsec maximum, this value will be considered the tolerance to match the AzTEC catalog and the Big IR catalog.

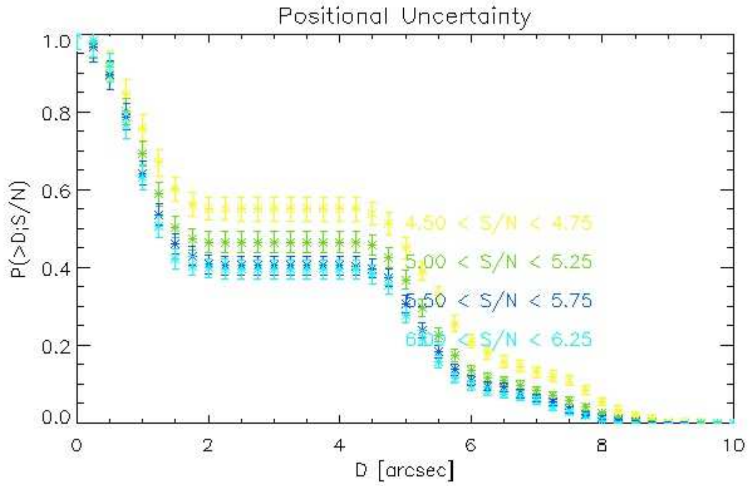

Figure 3.5: Resulting plot of the simulation which shows the positional uncertainty distribution (P is the probability to find a source out of a distance D), for 4 sample S/N bins.

## 3.5 The Final Catalog

TOPCAT's tool Matching tables is used again to compare IR catalogs (IRAC+2MASS, AKARI, MSX, MIPS24) with the AzTEC sources found in the same area (Table 3.8 shows the number of sources in each catalog used to construct the Final Catalog). This time a tolerance of 10 arcsec was used, based on the results of the Positional Uncertainty test. The option *Best Match Only* was selected as output instead of *Shows All Rows* (previously used to get the Big IR catalog), in order to know only the AzTEC sources that have counterparts in each IR catalog.

| **Catalog** | **Total sources** |
|---|---:|
| IRAC+2MASS | 36539 |
| AKARI | 332 |
| MIPS | 1198 |
| MSX | 821 |
| AzTEC | 118 |
| Big IR | 37973 |
| Final Catalog | 37998 |

Table 3.8: Total number of sources in each catalog used.

After that, the 4 matched tables were saved and arranged using a spreadsheet application according to the previously formed Big IR catalog. As a result, a Final Catalog with both, IR and millimeter fluxes is obtained. A copy of this Final Catalog is attached to the electronic form of this thesis.

Table 3.9 shows the AzTEC sources which have the most counterparts in all the catalogs. This data will be used to build Spectral Energy Distributions (SEDs), and to see which is their evolutionary stage.

Table 3.9: In this and next page, are shown the fluxes of AzTEC sources and their IR counterparts within a radius of 10 arcsec, together with the respective errors. Units for all the bands are in mJy. The last column shows the maximum separation between the millimeter source and its IR counterpart in arcsec.

| # Source | J | e_J | H | e_H | K | e_K | I1 | e_I1 | I2 | e_I2 | I3 | e_I3 | I4 | e_I4 | S9W | e_S9W |
|---:|---:|---:|---:|---:|---:|---:|---:|---:|---:|---:|---:|---:|---:|---:|---:|---:|
| 004 | - | - | - | - | - | - | 0.5647 | 0.0261 | 0.4877 | 0.0354 | - | - | - | - | - | - |
| 006 | 28.2300 | 0.5477 | 20.9300 | 0.4240 | 14.2700 | 0.3022 | 6.5100 | 0.1479 | 4.1319 | 0.1313 | - | - | - | - | - | - |
| 015 | - | - | - | - | - | - | 0.6004 | 0.0199 | 0.9593 | 0.0408 | - | - | - | - | - | - |
| 017 | - | - | 1.0620 | 0.1194 | 14.7900 | 0.5857 | 431.0000 | 11.2700 | - | - | 2069.000 | 26.200 | - | - | 1720.0 | 30.5 |
| 023 | - | - | - | - | - | - | - | - | 74.3900 | 6.6460 | 215.500 | 6.360 | 295.300 | 8.255 | 739.4 | 62.4 |
| 024 | 1.3450 | 0.0471 | 2.1870 | 0.0846 | 1.7180 | 0.1029 | 1.1760 | 0.0709 | 0.6743 | 0.049 | - | - | - | - | - | - |
| 026 | 0.8679 | 0.0560 | 4.9370 | 0.1410 | 31.5600 | 0.6686 | 114.6000 | 2.6360 | 206.8000 | 5.1290 | 358.700 | 5.410 | 442.400 | 9.406 | - | - |
| 027 | - | - | - | - | - | - | - | - | - | - | - | - | - | - | - | - |
| 030 | - | - | - | - | - | - | 2.2680 | 0.1107 | 2.8770 | 0.1550 | 5.876 | 0.445 | - | - | - | - |
| 031 | - | - | - | - | - | - | - | - | - | - | - | - | - | - | - | - |
| 033 | - | - | - | - | - | - | - | - | - | - | - | - | - | - | - | - |
| 034 | - | - | - | - | - | - | 0.4829 | 0.0341 | 0.6507 | 0.0417 | - | - | - | - | - | - |
| 035 | - | - | - | - | 1.4390 | 0.1219 | 2.9480 | 0.1285 | 8.6860 | 0.4121 | 7.676 | 0.283 | 8.713 | 0.344 | - | - |
| 044 | - | - | - | - | - | - | 1.6660 | 0.0935 | 2.2530 | 0.1388 | - | - | - | - | - | - |
| 046 | - | - | - | - | - | - | 0.6074 | 0.0335 | 1.6540 | 0.0628 | 2.801 | 0.202 | 4.946 | 0.642 | - | - |
| 048 | - | - | 0.5997 | 0.0646 | 1.1980 | 0.0960 | 1.1550 | 0.0439 | 0.9104 | 0.0494 | - | - | - | - | - | - |
| 052 | 1.3960 | 0.0694 | 4.3600 | 0.2972 | 8.0380 | 0.4664 | 12.4900 | 0.5260 | 13.0600 | 0.5609 | 11.530 | 0.387 | 11.520 | 0.578 | - | - |
| 057 | 3.5360 | 0.0977 | 2.3180 | 0.1153 | 1.6810 | 0.1006 | 0.9906 | 0.0452 | 0.5731 | 0.0425 | - | - | - | - | - | - |
| 060 | - | - | - | - | - | - | 1.1920 | 0.0406 | 2.2350 | 0.0873 | 3.390 | 0.150 | 5.200 | 0.374 | - | - |
| 063 | - | - | - | - | - | - | 0.4056 | 0.0187 | 0.4997 | 0.0284 | - | - | - | - | - | - |
| 065 | - | - | - | - | - | - | 1.2710 | 0.0766 | 0.8717 | 0.0788 | 7.100 | 0.495 | 15.560 | 1.006 | - | - |
| 066 | - | - | - | - | - | - | 1.6480 | 0.0568 | 1.5030 | 0.0631 | - | - | - | - | - | - |
| 070 | - | - | - | - | - | - | 1.4550 | 0.0727 | 0.9507 | 0.0725 | 6.967 | 0.636 | - | - | - | - |
| 071 | 2.9980 | 0.0994 | 7.4320 | 0.2738 | 13.3000 | 0.4043 | 55.3800 | 0.8127 | 87.3800 | 1.3240 | 127.200 | 1.684 | 166.100 | 2.618 | - | - |
| 075 | 3.5290 | 0.0878 | 9.1680 | 0.2956 | 10.7800 | 0.3277 | 7.0410 | 0.1446 | 4.3870 | 0.1183 | 3.349 | 0.167 | - | - | - | - |
| 081 | - | - | - | - | - | - | 1.0850 | 0.0558 | 0.5211 | 0.0468 | 6.201 | 0.369 | 13.970 | 0.992 | - | - |
| 086 | - | - | 3.8260 | 0.1409 | 5.4440 | 0.1755 | 4.0240 | 0.0830 | 2.8590 | 0.1023 | 1.970 | 0.129 | - | - | - | - |
| 087 | - | - | 1.2130 | 0.0726 | 2.4140 | 0.1201 | 2.4660 | 0.0751 | 1.5380 | 0.0722 | 2.712 | 0.327 | - | - | - | - |
| 095 | - | - | - | - | - | - | 0.7206 | 0.0255 | 0.6401 | 0.0326 | - | - | - | - | - | - |
| 098 | 3.5030 | 0.0968 | 2.8050 | 0.0930 | 2.0770 | 0.1167 | 1.0790 | 0.0333 | 0.6483 | 0.0313 | - | - | - | - | - | - |
| 099 | - | - | 1.2680 | 0.0782 | 2.8180 | 0.1142 | 3.3270 | 0.1471 | 2.3840 | 0.1086 | - | - | - | - | - | - |
| 112 | 13.2000 | 0.3890 | 10.8100 | 0.5377 | 7.5290 | 0.3190 | 4.2690 | 0.1940 | 2.5700 | 0.1371 | - | - | - | - | - | - |
| 116 | - | - | - | - | - | - | 0.4072 | 0.0221 | 0.4465 | 0.0390 | - | - | - | - | - | - |
| 117 | - | - | - | - | 0.6879 | 0.1020 | 2.1730 | 0.0491 | 2.8080 | 0.0796 | 2.886 | 0.152 | - | - | - | - |
| 119 | 0.4917 | 0.0494 | 1.5260 | 0.0998 | 1.8480 | 0.0936 | 1.3940 | 0.0441 | 0.9607 | 0.0429 | - | - | - | - | - | - |
| 123 | - | - | 2.6270 | 0.1573 | - | - | 6.1660 | 0.1356 | 4.2830 | 0.1165 | 5.588 | 0.424 | - | - | - | - |
| 128 | 1.1730 | 0.0616 | 5.8550 | 0.1887 | 11.1900 | 0.3194 | 10.3700 | 0.1942 | 7.8950 | 0.1584 | 5.720 | 0.156 | 3.567 | 0.130 | - | - |
| 130 | 9.1640 | 0.3123 | 9.6360 | 0.4704 | 7.0780 | 0.2803 | 3.0250 | 0.0576 | 1.8770 | 0.0704 | 1.277 | 0.116 | - | - | - | - |
| 132 | - | - | 4.1950 | 0.3670 | 8.6840 | 0.4639 | - | - | 19.6200 | 1.4310 | 73.120 | 4.327 | 229.500 | 13.000 | 1347.0 | 23.7 |
| 135 | - | - | 1.8500 | 0.0784 | 3.5770 | 0.1318 | 3.6550 | 0.0824 | - | - | 2.316 | 0.188 | - | - | - | - |

Table 3.9: *Continued.*

| # Source | L18W | e_L18W | A | e_A | C | e_C | D | e_D | E | e_E | 24 $\mu$m | e_24 $\mu$m | 1.1 mm | e_1.1 mm | Separation |
|---|---|---|---|---|---|---|---|---|---|---|---|---|---|---|---|
| 004 | - | - | - | - | - | - | - | - | - | - | 14.040 | 2.106 | 1224.16 | 50.14 | 3.67 |
| 006 | - | - | - | - | - | - | - | - | - | - | - | - | 1006.85 | 50.37 | 9.95 |
| 015 | - | - | - | - | - | - | - | - | - | - | - | - | 656.23 | 46.25 | 5.81 |
| 017 | 8862.0 | 84.4 | 2071.80 | 84.94 | 3409.80 | 180.72 | 5475.80 | 334.02 | 13408.00 | 804.50 | 469.205 | 27.180 | 696.66 | 51.59 | 4.12 |
| 023 | - | - | 631.03 | 27.13 | 1267.60 | 91.27 | 1300.70 | 91.05 | 2873.10 | 189.63 | 309.082 | 33.100 | 635.25 | 50.96 | 6.58 |
| 024 | - | - | - | - | - | - | - | - | - | - | - | - | 575.59 | 46.76 | 6.22 |
| 026 | 1840.0 | 60.5 | 1695.10 | 69.50 | 2748.40 | 151.16 | 1878.40 | 122.10 | 2273.00 | 159.11 | 117.184 | 31.390 | 565.23 | 44.69 | 4.78 |
| 027 | - | - | 1858.30 | 76.19 | 2860.40 | 154.46 | - | - | - | - | - | - | 607.99 | 50.48 | 7.44 |
| 030 | - | - | - | - | - | - | - | - | - | - | - | - | 524.42 | 47.58 | 5.84 |
| 031 | - | - | 1909.30 | 78.28 | 3128.70 | 168.95 | 1202.30 | 85.36 | 2543.10 | 172.93 | - | - | 577.99 | 52.55 | 9.01 |
| 033 | - | - | 988.17 | 41.50 | 1738.50 | 113.00 | 1143.80 | 147.55 | - | - | - | - | 540.44 | 50.11 | 6.74 |
| 034 | - | - | - | - | - | - | - | - | - | - | - | - | 547.06 | 51.64 | 8.40 |
| 035 | 372.0 | 16.0 | - | - | - | - | - | - | - | - | 103.556 | 13.830 | 495.53 | 48.95 | 3.99 |
| 044 | - | - | - | - | - | - | - | - | - | - | - | - | 459.08 | 51.77 | 7.35 |
| 046 | - | - | - | - | - | - | - | - | - | - | - | - | 441.32 | 50.98 | 8.99 |
| 048 | - | - | - | - | - | - | - | - | - | - | - | - | 339.04 | 47.73 | 9.27 |
| 052 | - | - | - | - | - | - | - | - | - | - | 67.819 | 1.196 | 394.89 | 48.68 | 3.60 |
| 057 | - | - | - | - | - | - | - | - | - | - | - | - | 403.09 | 55.62 | 2.71 |
| 060 | - | - | - | - | - | - | - | - | - | - | - | - | 354.18 | 49.87 | 5.47 |
| 063 | - | - | - | - | - | - | - | - | - | - | - | - | 325.16 | 47.07 | 1.36 |
| 065 | - | - | - | - | - | - | - | - | - | - | - | - | 343.26 | 51.46 | 4.98 |
| 066 | - | - | - | - | - | - | - | - | - | - | - | - | 312.83 | 47.16 | 6.04 |
| 070 | - | - | - | - | - | - | - | - | - | - | - | - | 339.76 | 53.26 | 5.24 |
| 071 | - | - | 826.32 | 34.71 | 1584.10 | 102.97 | 1844.00 | 121.70 | 2467.00 | 170.22 | 68.744 | 14.788 | 342.83 | 53.89 | 4.63 |
| 075 | - | - | - | - | - | - | - | - | - | - | - | - | 306.11 | 49.49 | 1.87 |
| 081 | - | - | - | - | - | - | - | - | - | - | - | - | 306.95 | 51.38 | 4.94 |
| 086 | - | - | - | - | - | - | - | - | - | - | - | - | 268.24 | 47.43 | 8.14 |
| 087 | - | - | - | - | - | - | - | - | - | - | - | - | 279.08 | 50.37 | 5.40 |
| 095 | - | - | - | - | - | - | - | - | - | - | - | - | 244.26 | 46.32 | 2.15 |
| 098 | - | - | - | - | - | - | - | - | - | - | - | - | 269.15 | 52.13 | 6.19 |
| 099 | - | - | - | - | - | - | - | - | - | - | - | - | 253.56 | 49.52 | 1.51 |
| 112 | - | - | - | - | - | - | - | - | - | - | - | - | 243.71 | 50.44 | 2.45 |
| 116 | - | - | - | - | - | - | - | - | - | - | - | - | 256.83 | 54.70 | 4.89 |
| 117 | - | - | - | - | - | - | - | - | - | - | - | - | 238.12 | 50.72 | 3.76 |
| 119 | - | - | - | - | - | - | - | - | - | - | - | - | 212.84 | 46.03 | 6.36 |
| 123 | - | - | - | - | - | - | - | - | - | - | - | - | 243.62 | 56.46 | 9.06 |
| 128 | - | - | - | - | - | - | - | - | - | - | - | - | 218.07 | 48.30 | 3.88 |
| 130 | - | - | - | - | - | - | - | - | - | - | - | - | 212.56 | 47.31 | 2.62 |
| 132 | 3530.0 | 162.0 | 766.34 | 32.19 | 1089.50 | 84.98 | 1478.90 | 100.57 | 4694.00 | 295.72 | 332.848 | 23.510 | 245.10 | 54.86 | 5.60 |
| 135 | - | - | - | - | - | - | - | - | - | - | - | - | 222.59 | 50.76 | 1.04 |

# Chapter 4

# Young Stellar Object classification

## 4.1 Theory and Observations

The theory that explains the protostar structure is mainly based in the physical processes that take place in the stellar evolution, however there are some difficulties regarding this topic. As seen in the first chapter, it is known that these objects are deeply embedded in the dense cores where they are born, not to mention the dust in their surroundings, which absorbs practically all radiation that is produced in the accretion shock, and in their stellar interior. When the energy of these objects arrives at the dust photosphere, their spectrum is going to describe us mainly the characteristics of those surrounding grains. For this reason, it is hard to verify if really there is an infall of material, and even less possible to observe the structure of the disk or its characteristics. This motivates to invent and develop several methods that permit the detection of these special sources.

The most direct method to find them uses the emitted fluxes from a protostar and then, to compare those data with fluxes from known sources with the expected results that should appear if it is supposed in an infalling environment. It is necessary to build a quantitative model that shows the data of interest. However, usually there are several models that could fit the data, which means that is possible to explain in different ways the protostellar collapse. Even more, it is not clear yet which sources are more appropriate to use and to investigate (Stahler & Palla, 2004).

## 4.2 Classification and types of Objects

It is reasonable to start this analysis knowing how to classify the protostars that is possible to detect at IR wavelengths. A common way to do that starts by using the IR excess that emits a young star, which have its origin from the closer emission to the stellar surface and not from the reddening of the surrounding distant dust (a circumstellar phenomena). Any star that is within an embedded cluster is subject to reddening by foreground dust, even if the star has or has not an IR excess. In the moment that the Spectral Energy Distribution (SED) (which describes how much energy in flux or density emits an stellar object as a function of wavelength or frequency) of the studied source is build using the observed fluxes or magnitudes, it is possible to use the estimated extinction in the V passband, $A_V$, plus the extinction curve, to calculate the extinction that is present in all the other wavelengths, $A_\lambda$. Using this method, the "dereddened" energy distribution that is obtained from the circumstellar matter around the star, and of course, the star itself, can be reconstructed.

Stahler & Palla (2004) showed some stars as examples, which were detected at near IR surveys in the $\rho$ Ophiuchi dark cloud complex studied by Wilking et al. (1989). The dereddened SEDs of three representative sources of that complex are shown in the Fig. 4.1. In all the stars is plotted the flux measured per logarithmic wavelength interval, $\lambda F_\lambda$.

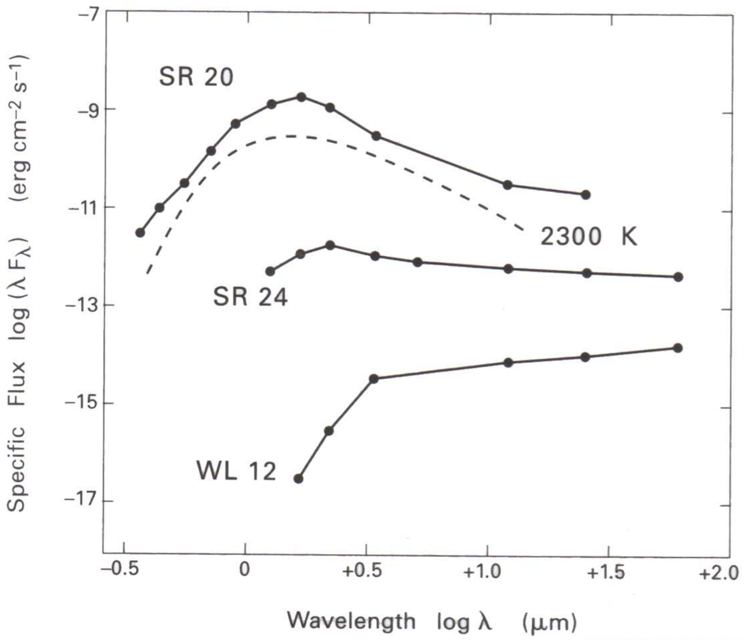

Figure 4.1: Spectral energy distribution of 3 stars within the Ophiuchi dark cloud complex showing examples for Class I, Class II and Class III sources from bottom to top, respectively. The dashed curve corresponds to a blackbody at 2300 K. From figures 3a, 3c and 3d of Wilking et al. (1989)

The remarked IR excess emission in first two sources have its origin from heated dust grains. From Wien's displacement law, $\lambda_{max} T = 0.29$ cm K, it is observed that the thermal radiation, which peaks at 10 $\mu$m, has a temperature close to 300 K. This IR excess does not show a true blackbody spectrum, which means that those stars necessarily have a considerable range of temperatures. Additionally, these temperatures are high enough that the dust around must be close to the star. Probably, these grains that come from a cloud are feeding the protostar, participating in its collapse or is just material left behind after this collapse was terminated.

Following this idea, it is possible to use the IR excess as an empirical measure of stellar youth. This method was introduced by Lada (1987) quantifying the matter by using an index called the IR spectral index $\alpha_{IR}$, defined by the following expression:

$$\alpha_{IR} \equiv \frac{d \log{(\lambda F_\lambda)}}{d \log \lambda} \tag{4.1}$$

The evaluation of this index generally is arbitrary, in this thesis the wavelengths that will be used range between 2.2 and and 24 $\mu$m to derive both, $\alpha_{IR}$ and to plot color-color diagrams, which give useful information about the evolutionary stage of the studied sources. By evaluating this index in each of the cataloged sources, is possible to classify them depending of the $\alpha_{IR}$ value. An IR source with $\alpha_{IR} > 0$ is said to be in Class I, star WL 12 is an example of this (see Fig. 4.1). An IR source with $-1.5 < \alpha_{IR} < 0$ is within Class II classification, star SR 24 belongs to this group. Finally, a source that have $\alpha_{IR} < -1.5$ is said to be in Class III classification, star SR 20 belongs to this set. Andre et al. (1993) noted that several sources have not been detected in the near-IR and have blackbody-like SEDs that peak in the submillimeter range, suggesting extremely low dust temperatures (∼20−30 K). They called these sources Class 0 because their cold temperature suggested an object even younger than typical Class I objects (see Fig. 4.2).

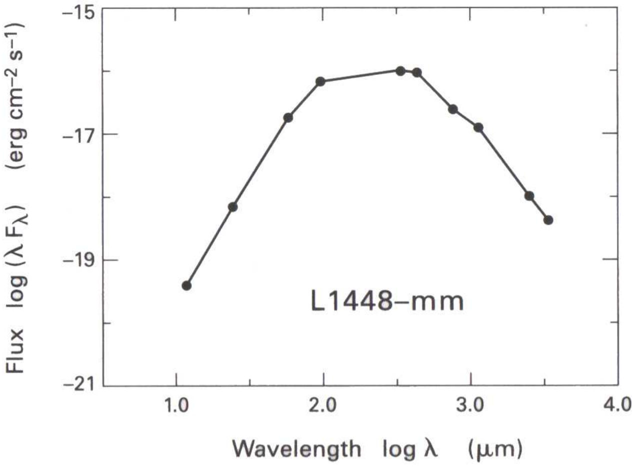

Figure 4.2: Spectral energy distribution of Class 0 source L1448/mm in Perseus. From unpublished data by Barsony et al. (1997). Figure done by J. O'Linger.

This type of source has been added in the above classification, and includes sources that are deeply buried in the cores and can only be detected at far-IR and millimeter wavelengths. L1448/mm is in the Perseus region, 300 pc distant (See Barsony et al., 1997). Note that the SED of this object is shifted to much longer wavelengths than the other sources shown in Fig. 4.1.

## 4.3 YSOs in Carina South Pillars Region (SPR)

The previous classification of Class 0/I, II, and III has been used preferentially in regions of low-mass star formation, but since it reflects the shape of SEDs of young objects, it is possible to use the same approach for all the IR-mm sources in the Final Catalog of SPR (see Chapter 3), without *a priori* knowledge of their stellar mass. Besides, the main difference between high-mass and low-mass star formation via accretion is the mass accretion rate (Garay, 2004), as it was mentioned at the end of section 1.2.

As a first approximation to YSO classification, an IR spectral index $\alpha_{IR}$ with 2.12 $\lesssim \lambda \lesssim$ 24 $\mu$m using Equation 4.1, is used to classify the nature of the evolutionary stage of YSO candidates. As a result, 675 Class 0/I, 2251 Class II, and 30068 Class III objects were obtained. The classification suggested by Lada is used because the aims are:

1. To know how the studied sources are distributed in color-color diagrams, which of them are reddened (embedded), and what is their evolutionary stage
2. To compare if that evolutionary stage is in agreement with the information that will be obtained in the construction of the SEDs for those millimeter sources that have counterparts in the IR catalogs (see Chapter 5).

Table 4.1 gives the total number of sources by class in the catalogs and in the diagnostic diagrams.

Table 4.1: Statistics of Lada classification sources.

| **Source Class** | **In Final catalog** | **In AzTEC catalog** | **In I1-I2 vs. I3-I4 diagram** | **In I2-I3 vs. I4-24$\mu$m diagram** |
|---|---:|---:|---:|---:|
| 0/I | 675 | 19 | 80 | 15 |
| II | 2251 | 10 | 472 | 83 |
| III | 30068 | 11 | 6500 | 196 |
| Cores | - | 12 | - | - |

Since mm-emission traces dust in the form of disks and envelopes around YSOs, millimeter objects (S/N $>$ 4 [1] ) with two or more fluxes within 2.12 and 24 $\mu$m were classified. A total of 19 Class 0/I, 10 Class II and 11 Class III millimeter objects were classified. The rest of 12 objects could not be classified, and they will be considered as millimeter cores (to be treated in Chapter 6).

40 AzTEC sources with *a priori* Lada classification of YSOs –except AzTEC 002, which is a cluster of IR sources with a bright millimeter counterpart (the Treasure Chest, see Chapter 7)–, are listed in Table 4.2. This classification was done without considering the local extinction due to nebulosity around YSOs as part of the molecular maternal cloud.

---

[1] Even the results of the Monte Carlo simulations in Chapter 3 suggested that real millimeter sources have S/N $>$ 6 (false detection rate = 1), remember that a lower value of S/N $>$ 4 is used because IR counterparts were found for these sources.

Also in this table are shown the interstellar extinction, $A_V$, obtained from NIR data, and the number of stars to get this value.

Table 4.2: AzTEC sources (S/N $>$ 4) and *a priori* Lada classification.

| **AzTEC Source** | $\alpha_{IR}$[1] | **Class**[2] | $A_V$[3] | **# stars**[4] |
|---:|---:|---:|---:|---:|
| 002 | - | - | 15.00 | 79 |
| 004 | 0.816 | 0/I | 15.00 | 93 |
| 006 | -2.623 | III | 19.00 | 66 |
| 015 | 0.986 | 0/I | 16.00 | 64 |
| 017 | 0.905 | 0/I | 15.00 | 112 |
| 023 | 0.927 | 0/I | 15.00 | 101 |
| 024 | -2.190 | III | 15.50 | 102 |
| 026 | 0.365 | 0/I | 15.00 | 77 |
| 027 | 0.130 | 0/I | 15.00 | 64 |
| 030 | 1.046 | 0/I | 15.00 | 61 |
| 031 | -0.903 | II | 14.00 | 77 |
| 033 | -0.575 | II | 14.50 | 92 |
| 034 | 0.264 | 0/I | 17.00 | 84 |
| 035 | 1.178 | 0/I | 15.00 | 102 |
| 044 | 0.279 | 0/I | 17.00 | 70 |
| 046 | 1.557 | 0/I | 18.00 | 68 |
| 048 | -1.325 | II | 18.00 | 94 |
| 052 | 0.513 | 0/I | 14.00 | 103 |
| 057 | -2.401 | III | 16.00 | 96 |
| 060 | 0.824 | 0/I | 15.50 | 112 |
| 063 | -0.116 | II | 17.00 | 78 |
| 065 | 2.684 | 0/I | 16.00 | 95 |
| 066 | -1.390 | II | 14.00 | 86 |
| 070 | 2.417 | 0/I | 16.00 | 111 |
| 071 | 0.633 | 0/I | 14.00 | 81 |
| 075 | -2.230 | III | 14.00 | 90 |
| 081 | 2.895 | 0/I | 14.00 | 91 |
| 086 | -2.026 | III | 15.00 | 55 |
| 087 | -1.061 | II | 16.00 | 88 |
| 095 | -1.502 | III | 16.00 | 84 |
| 098 | -2.543 | III | 15.00 | 85 |
| 099 | -1.136 | II | 17.00 | 83 |

Table 4.2: *Continued.*

| **AzTEC Source** | $\alpha_{IR}$[1] | **Class**[2] | $A_V$ [3] | **# stars**[4] |
|---:|---:|---:|---:|---:|
| 112 | -2.412 | III | 14.00 | 113 |
| 116 | -0.609 | II | 16.00 | 64 |
| 117 | 0.566 | 0/I | 17.00 | 91 |
| 119 | -1.838 | III | 16.00 | 92 |
| 123 | -1.208 | II | 16.00 | 70 |
| 128 | -1.887 | III | 17.00 | 81 |
| 130 | -2.789 | III | 16.00 | 131 |
| 132 | 1.508 | 0/I | 16.25 | 76 |
| 135 | -1.443 | II | 16.00 | 81 |

[1] $\alpha_{IR} \equiv \frac{d\log(\lambda F_\lambda)}{d\log\lambda}$, $2.12 \lesssim \lambda \lesssim 24$ $\mu$m

[2] As introduced by Lada (1987).

[3] Mode of $A_V$ values from MS stars within a radius of 180 arcsec from AzTEC source.

[4] MS stars with interstellar extinction estimated from NIR data, within an 180 arcsec radius from the AzTEC source position.

To get the interstellar extinction towards AzTEC sources, we obtained the mode of $A_V$ values from a group of main sequence (MS) stars within a radius of 180 arcsec centered in each AzTEC source position. The $A_V$ values were obtained from dereddened MS stars with photometry in the J, H, and K bands. In Fig. 4.3 a color-color diagram of these bands is presented. The reddened MS sources lying between the two upper lines in the direction of the extinction vector, were dereddened to the isochrone of $10^8$ years along the extinction direction in the magnitude-color diagram K vs H-K shown in Fig. 4.4.

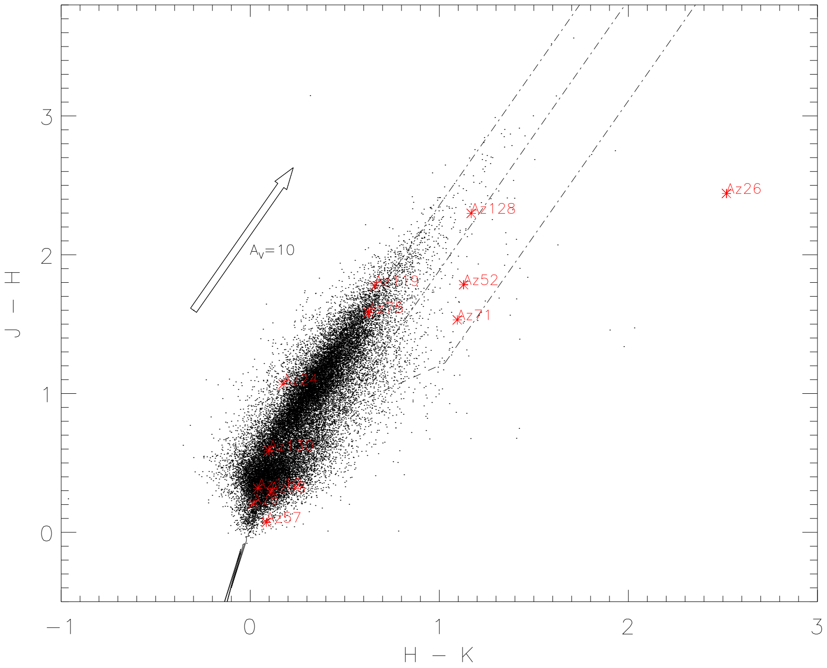

Figure 4.3: Color-color diagram H-K vs J-H of all sources in the final catalog. Some AzTEC sources with J, H, K counterparts are labeled in red color.

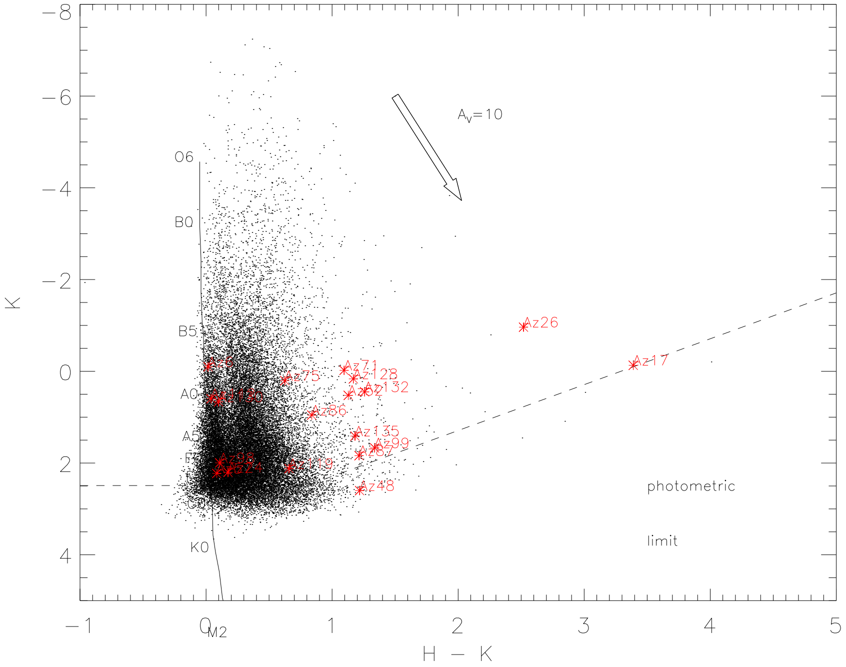

Figure 4.4: Color-magnitude diagram H-K vs K of all sources in the final catalog. Some AzTEC sources with J, H, K counterparts are labeled in red color.

The distribution of extinction values towards the SPR is shown in Fig 4.5, where foreground stars have $A_V \lesssim 10$ mag, and the average extinction to the more cloudy regions of SPR is about 16 mag. As mentioned, column 4 of the Table 4.2 gives the extinction values for these AzTEC sources. Some of the $A_V$ values were modified according to the information provided by the NIR diagrams.

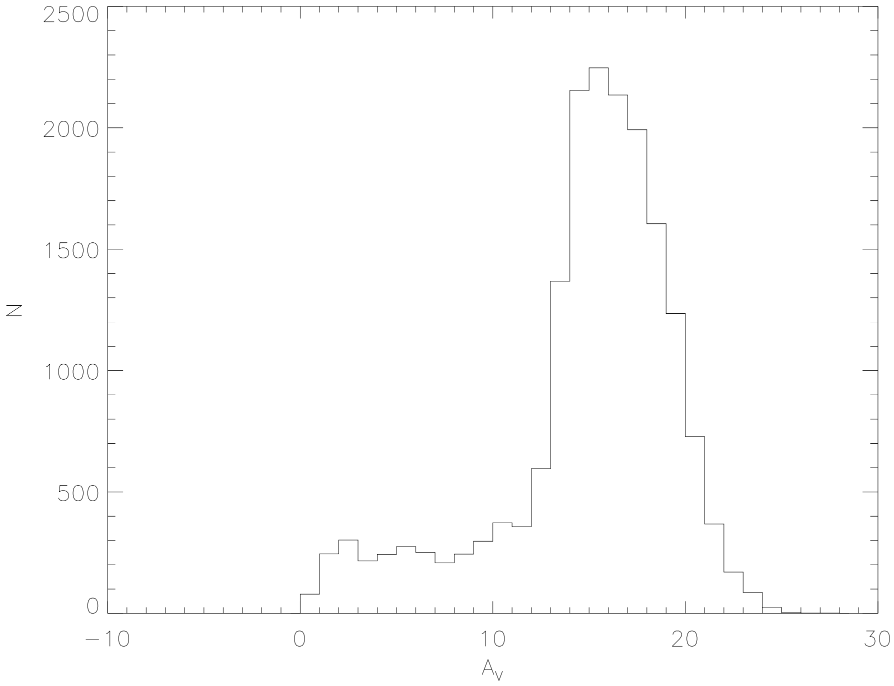

Figure 4.5: Histogram showing the frequency of sources that have certain $A_V$ values.

Nine AzTEC sources (006, 024, 057, 075, 098, 112, 119, 128, and 130) labeled in Fig. 4.3 lie in the MS locus, and are also classified as Class III in Table 4.2. The remaining sources (026, 052 and 071) in this diagram are classified as Class 0/I. From the color-magnitude NIR diagram, six of the nine AzTEC MS stars lie very close to the isochrone of $10^8$ year (continuous line with spectral type labels).

Also, two Spitzer color-color diagrams were constructed, which give a global idea on the approximated number of YSOs and their classes within our region. The first diagram (Fig. 4.6), [3.6]-[4.5] vs. [5.8]-[8.0], shows following number of plotted sources: 80 Class 0/I, 472 Class II and 6500 Class III (from which 9 of them are labeled as AzTEC sources). In the second color-color diagram (Fig. 4.7) the IRAC bands I2, I3, and I4 together with MIPS24 band were used. Note that here, the number of Class III is smaller compared with Fig. 4.6 due to fewer sources with counterpart in the MIPS24 catalog. The number of plotted sources in this diagram are: 15 Class 0/I, 83 Class II and 196 Class III sources, from which 4 AzTEC sources are labeled.

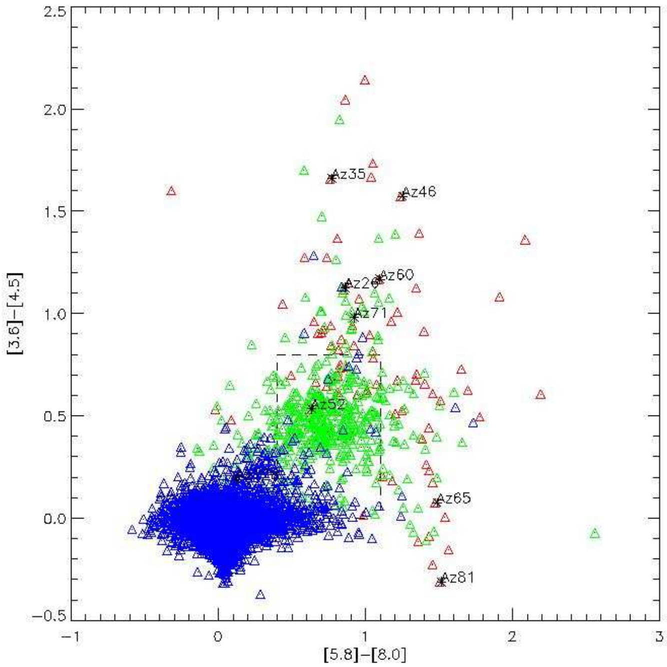

Figure 4.6: Color-color diagram using IRAC bands I1-12 vs. I3-I4. The blue triangles represent Class III sources, the green ones Class II sources and the red ones Class 0/I sources. Some AzTEC sources are identified.

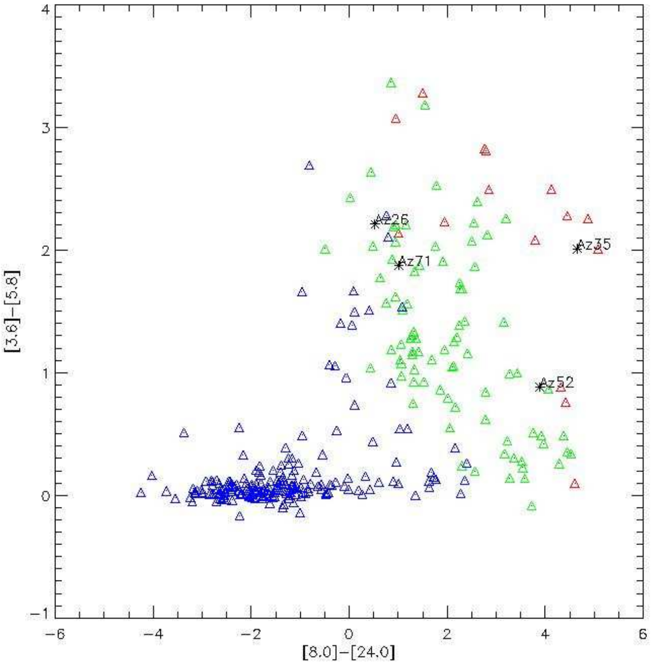

Figure 4.7: Color-color diagram using IRAC bands I2-13 vs. I4-MIPS24. The colors of the triangles are the same as in Fig. 4.6, Red Note that there are very few Class III sources due to a lack of counterparts in the MIPS24 catalog. Also, some AzTEC sources are labeled.

## 4.4 Visual Inspection of AzTEC sources

From the Final catalog of $\eta$ Car South Pillars sources, 40 matches of different evolutionary class were found (see Table 3.9), but millimeter observations have lower angular resolution than IR observations, so it is possible that the automatic matching might be erroneous in some cases where more than one IR sources can be considered as counterpart of an AzTEC source. Then, a visual inspection in several IR wavelengths is necessary in order to check the most probable IR counterpart of AzTEC sources, and thus, to identify their YSO or mm-core nature. The goal will be to analyze the characteristics of true millimeter YSOs.

The visual inspection of several snapshots in the IRAC, 2MASS, MIPS and AzTEC maps was made and several matches were discarded as it is detailed below:

1. Sources classified as Class III, which are probably close foreground stars, but not closely linked to the mm-emission (e.g. AzTEC 057, 075).
2. Some Class II sources in the above situation (e.g. AzTEC 048, 066).
3. Visible star clusters in IRAC 1 and 2 bands $-$frequently around the AzTEC source$-$, it is difficult to associate a source to the mm-emission (e.g. AzTEC 046)
4. Millimeter emission that coincides with a visible cavity in 8 and 24 micron bands, close but not coincident with Class 0/I source in the structure's peak, formed by the radiation pressure of UV photons (e.g. AzTEC 119)

The result of this visual inspection modifies the number of cores by increasing it to 40, leaving only 10 Class 0/I, 2 Class II and none Class III stellar sources associated with mm-emission. Note that the AzTEC map does not include extended mm-emission, which will be used in a further study. Besides, to guarantee that cores in the new list do not have stellar signatures, data in IR and sub-mm would be required, and in some cases, also millimeter observations with higher angular resolution. In Table 4.3 are listed the classes of the studied AzTEC sources before (only using the matching data from the Final Catalog), and after the visual inspection, which helps to know if the association made by TOPCAT was correct or not.

Table 4.3: Counts of source classification, but now including results from visual inspection.

| **Source Class** | **In Final catalog** | **In AzTEC catalog** | |
|---|---|---|---|
| | | **before VI**[2] | **after VI** |
| 0/I | 675 | 19 | 10 |
| II | 2251 | 10 | 2 |
| III | 30068 | 11 | 0 |
| Cores | - | 12 | 40 |

The 12 AzTEC objects that both, fall within the box defined in Table 2.3, and most probably have an IR counterpart after the visual inspection, are considered **YSO candidates** (here after **YSOc**). Fig. 4.8 shows these 12 YSOc in snapshots of *Spitzer* bands, millimeter and NIR frames.

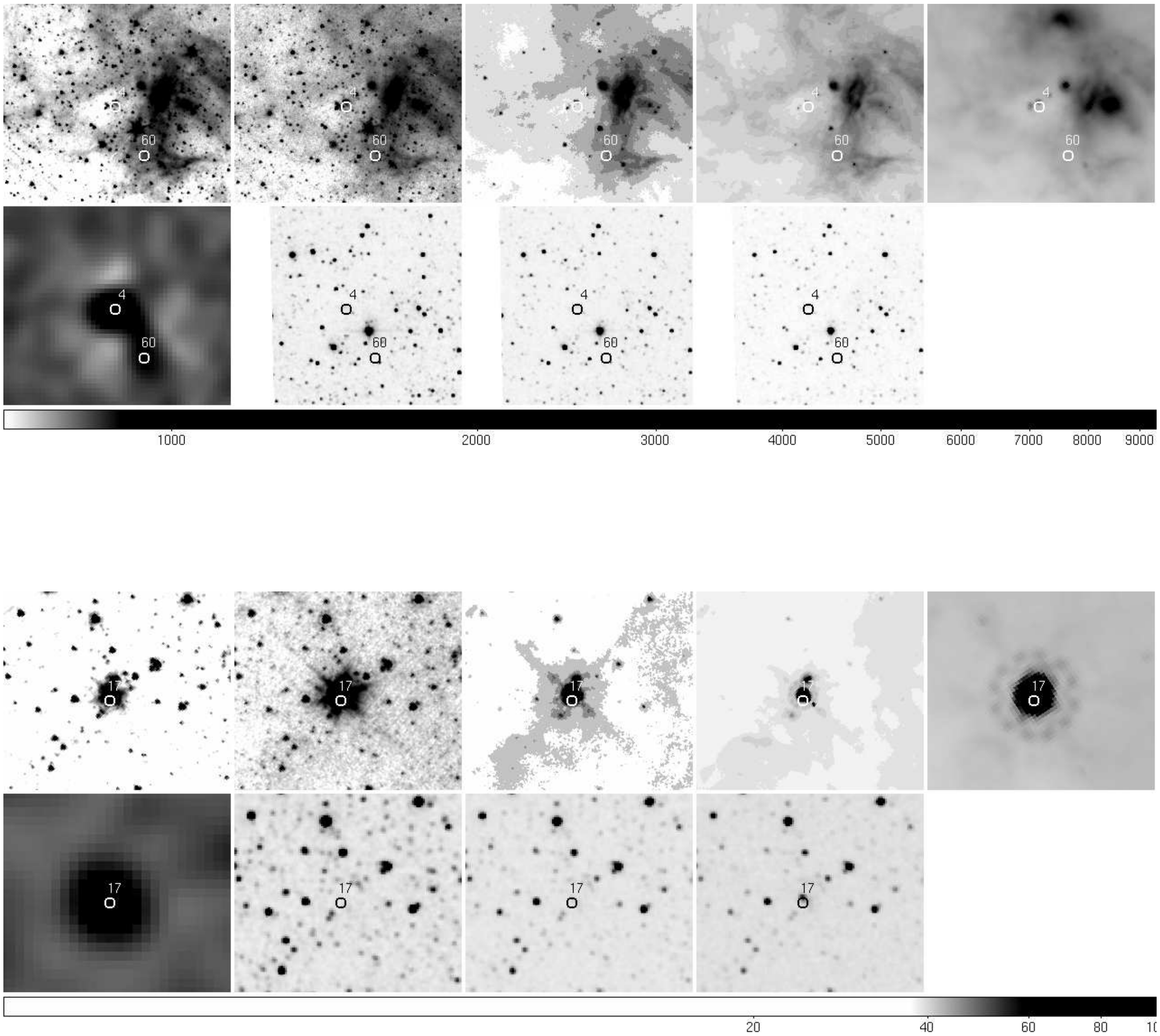

Figure 4.8: Detailed images from fields of AzTEC sources 004 and 015 in the bands: IRAC (1, 2, 3, 4), MIPS 24 $\mu$m, AzTEC 1.1 mm, and J, H and K of 16 AzTEC sources with IR counterparts. This images help to determinate if the association between the IR source and the mm-emission is highly probably or not. Some fields include more than one AzTEC source. The North is up and the East to the left.

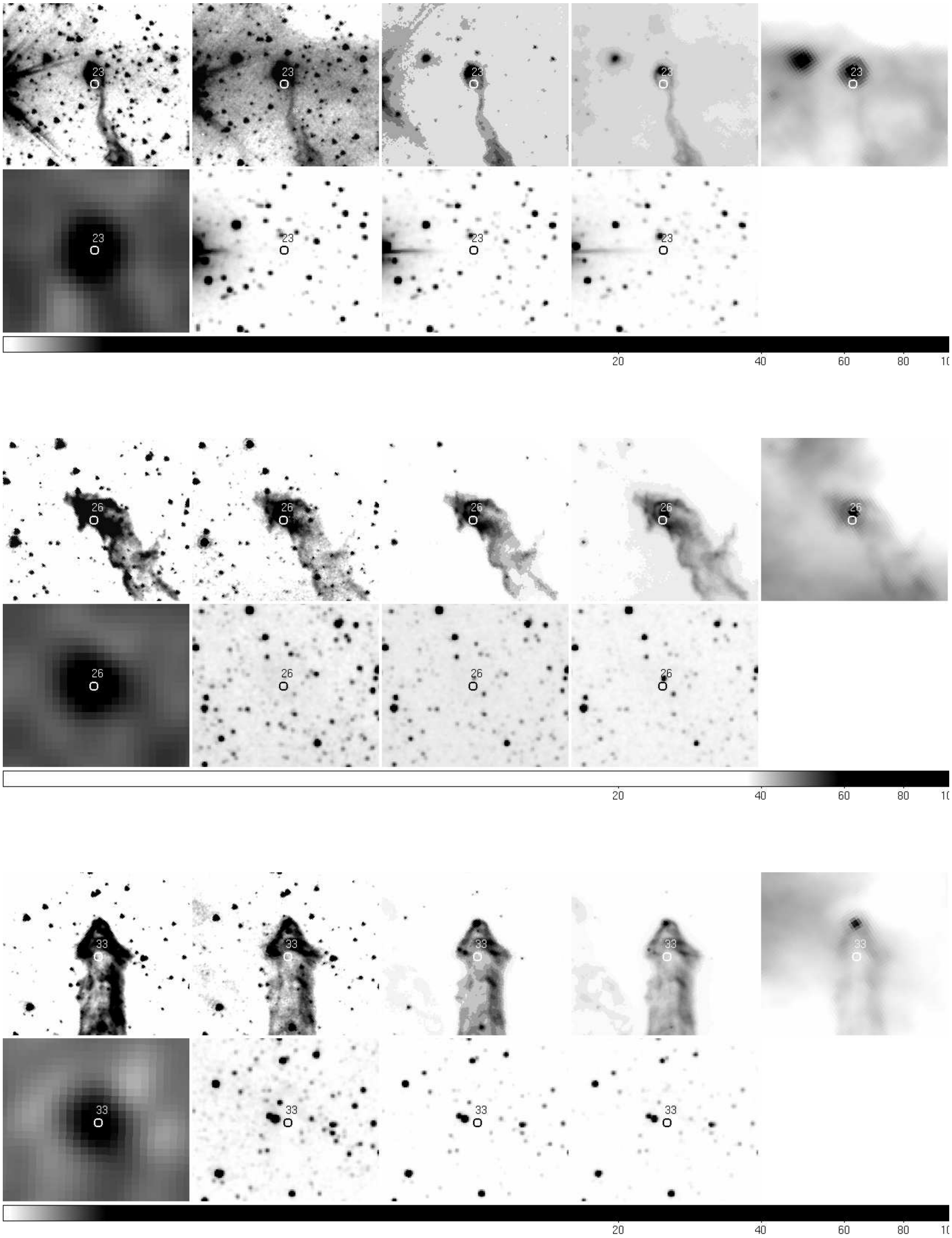

Figure 4.8: *Continued for AzTEC sources 023, 026 and 033.*

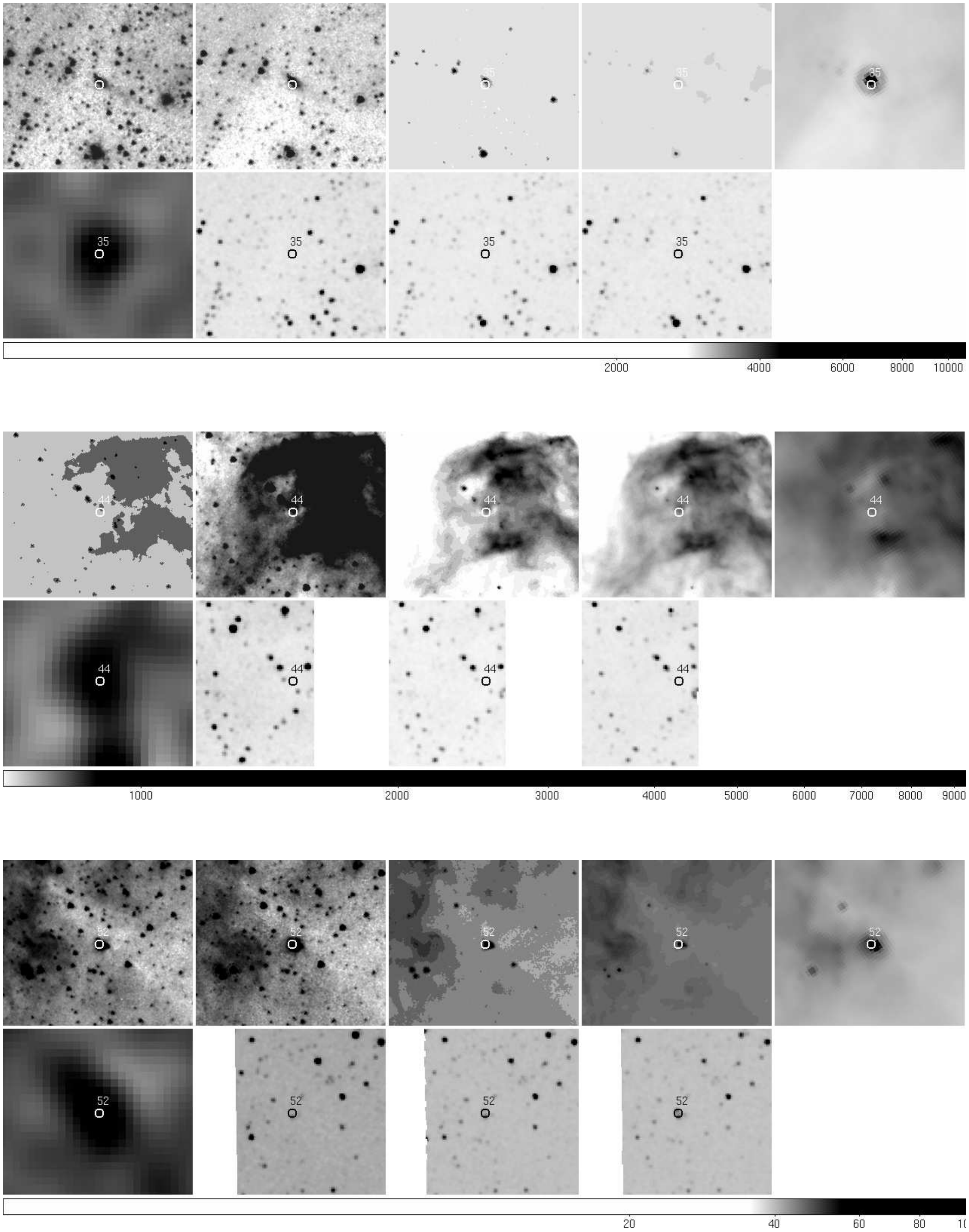

Figure 4.8: *Continued for AzTEC sources 035, 044 and 052.*

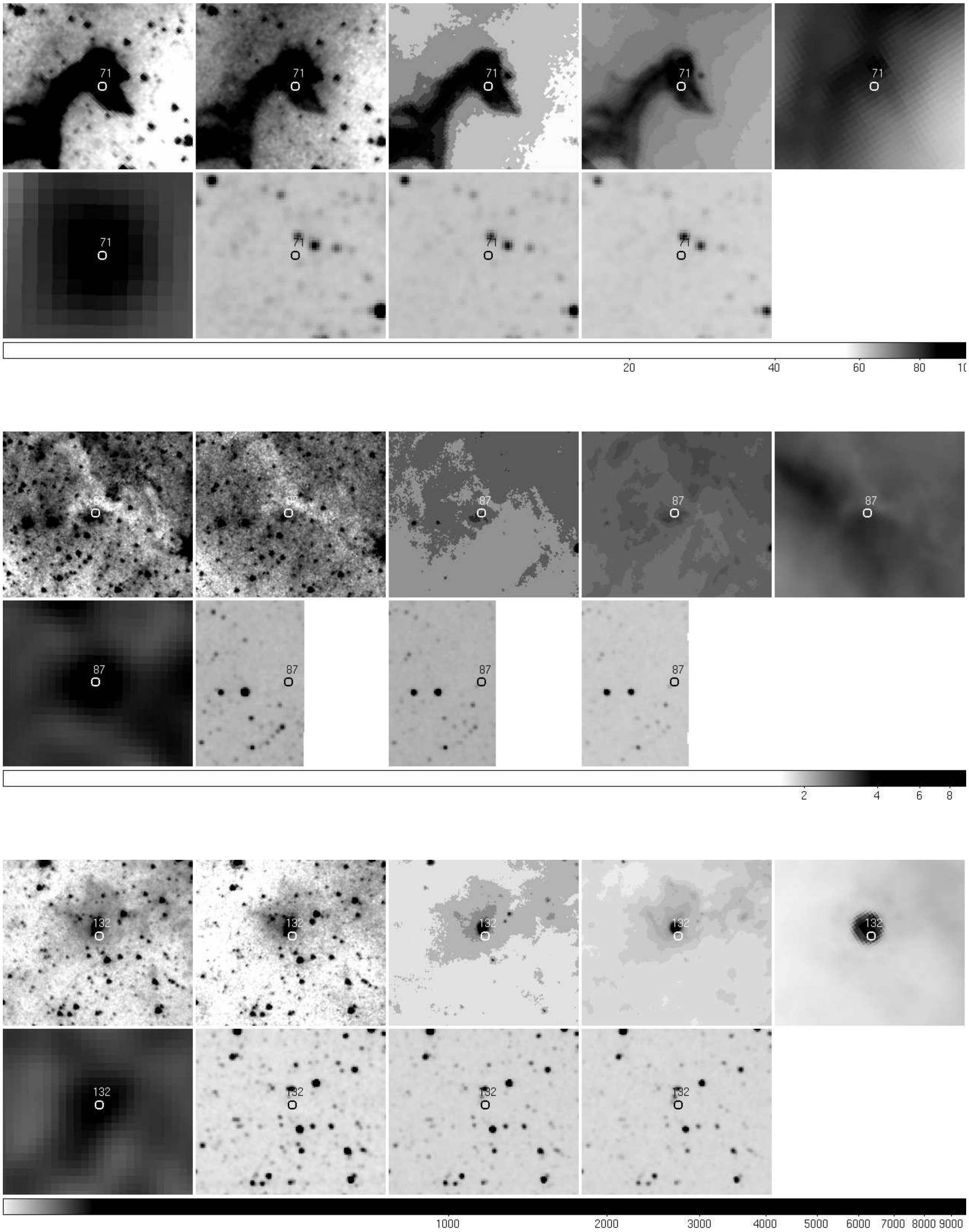

Figure 4.8: *Continued for AzTEC sources 071, 087 and 132.*

Fig. 4.9 shows some examples of AzTEC sources (024 and 119) that **do not** have a clear association with any IR source, and thus considered as mm-cores, which will be treated on Chapter 6.

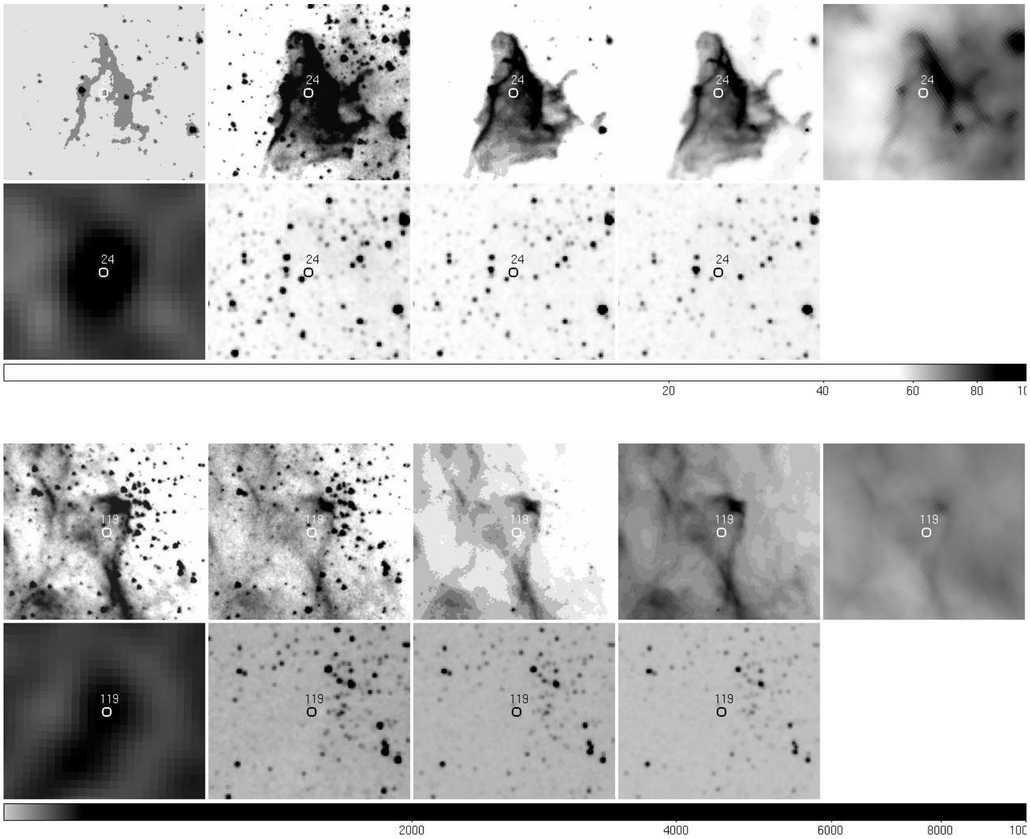

Figure 4.9: Same as Figure 4.8, but now showing a pair of AzTEC sources without a visible source that could be associated.

Individual comments about different characteristics from the visual appearance of each AzTEC source, and the consideration to be YSOc or mm-core are shown in the last column of Table 4.4. Four pillar-like structures are seen in MIR images, in Table 4.4 there are 9 AzTEC sources within a pillar body (PB), only 3 are in the pillar head (PH) and one behind a PH. Also, 8 sources are located within an irradiated edge structure (BIE). 22 millimeter cores show sources around them. The sources under the MSC label show multiple sources where one of them was chosen as the most probably to be the IR counterpart, since the others could be foreground sources according with their snapshots. Finally, sources with IR-c label are double sources that are difficult to separate, for this reason, a limiting millimeter flux value with 50% confidence was considered in the fitting of SEDs (see Chapter 5).

Table 4.4: AzTEC sources (S/N > 4) and *a priori* Lada classification.

| **AzTEC Source** | **YSOc** | **Millimeter Core** | **Comments** [1] |
|---|---|---|---|
| 002 | N | N | MSC, Treasure Chest[2] |
| 004 | Y | N | IR-c |
| 006 | N | Y | SAC, HII-AC |
| 015 | N | Y | SAC, PB |
| 017 | Y | N | IR-c, SAC |
| 023 | Y | N | PH |
| 024 | N | Y | PH |
| 026 | Y | N | PH, SAC |
| 027 | N | Y | SAC |
| 030 | N | Y | BIE, HII-AC |
| 031 | N | Y | BIE, SAC |
| 033 | Y | N | BIE, SAC |
| 034 | N | Y | SAC |
| 035 | Y | N | IR-c, SAC |
| 044 | Y | N | MSC, PB |
| 046 | N | Y | SAC, PB |
| 048 | N | Y | N |
| 052 | Y | N | SAC, MSC |
| 057 | N | Y | PB |
| 060 | Y | N | SAC |
| 063 | N | Y | MSC |
| 065 | N | Y | SAC, PB |
| 066 | N | Y | SAC, PB |
| 070 | N | Y | MSC |
| 071 | Y | N | IR-c, BIE |
| 075 | N | Y | SAC, PB |
| 081 | N | Y | BIE |
| 086 | N | Y | BIE |
| 087 | Y | N | PB |
| 095 | N | Y | SAC |
| 098 | N | Y | MSC |
| 099 | N | Y | BIE |
| 112 | N | Y | MSC |
| 116 | N | Y | N |
| 117 | N | Y | SAC |
| 119 | N | Y | BIE, SAC |
| 123 | N | Y | SAC |

Table 4.4: *Continued.*

| AzTEC Source | YSOc | Millimeter Core | Comments [1] |
|---|---|---|---|
| 128 | N | Y | MSC, PB |
| 130 | N | Y | SAC, MSC |
| 132 | Y | N | SAC |
| 135 | N | Y | SAC |

[1] Comments after visual inspection (See Section 4.4). *IR-c*: Double IR counterpart, *SAC*: Sources around the millimeter core, *MSC*: Multiple IR sources within the core, *BIE*: Behind an irradiated edge, *HII-AC*: HII region from (Rathborne et al., 2004) around the core, *N*: Within a nebulosity, *PB*: Within the pillar body, *PH*: Within the pillar head.

[2] Multiple YSOs (Smith et al., 2005)

## 4.5 Spatial distribution of YSOc

In order to investigate the level of influence from $\eta$ Car in the star formation history of the Pillars Region, it is useful to visualize the spatial distribution of millimeter sources that have been classified in previous sections. Figure 4.10 shows the location of 40 AzTEC sources from automatic matching in the Final catalog, classified as Class 0/I, II or III, while Figure 4.11 shows the scenery of 16 AzTEC sources after the visual inspection was performed.

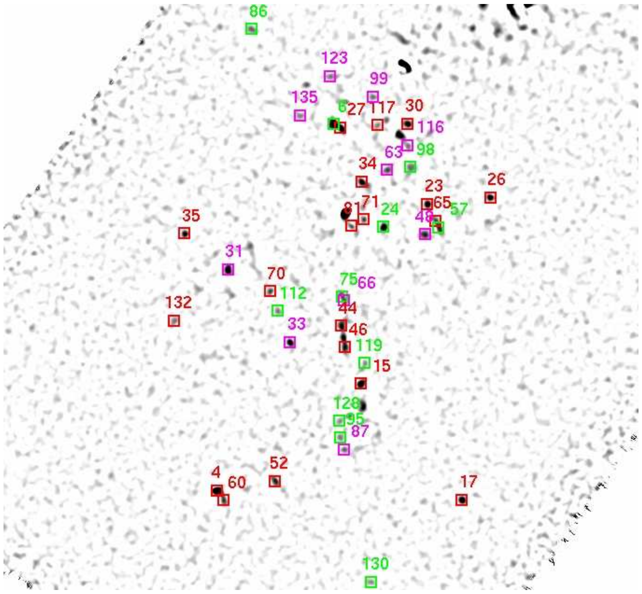

Figure 4.10: Spatial distribution of AzTEC sources as they were automatically matched with IR counterparts. Square symbols over the millimeter AzTEC map have colors Red: Class 0/I, Magenta: Class II and Green: Class III.

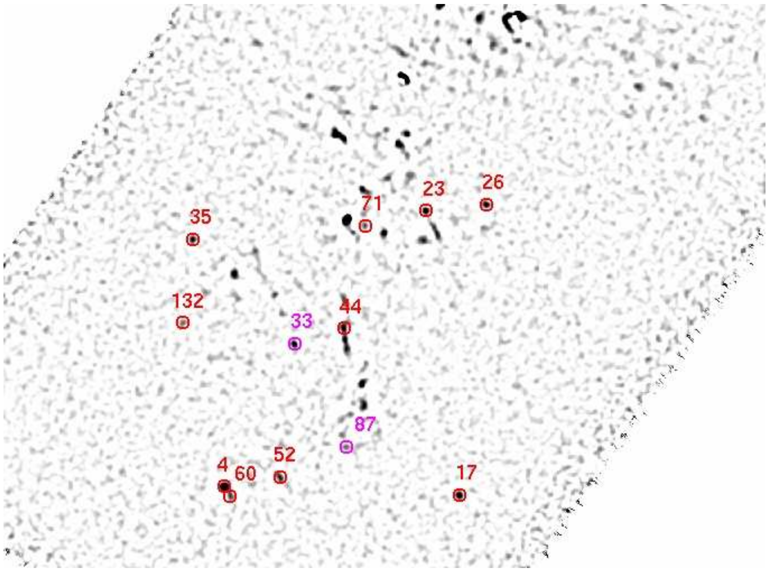

Figure 4.11: Spatial distribution of AzTEC YSOc after visual inspection (See Section 4.4). Colors of circle symbols are the same as seen in Fig. 4.10, Red: Class 0/I, Magenta: Class II

Note that in this case, only Class 0/I and II YSOc remain classified, which is in agreement with the fact that Class III sources are not observed at millimeter wavelengths. From Figure 4.11, it appears that there is not a clear sequential star formation history from the position of $\eta$ Car, since all the sources are more or less spread through the region. Nevertheless, it is remarkable that most sources close to the head of a pillar show millimeter emission and a young evolutionary stage. To go into a deeper analysis of the physical characteristics of these YSOc, theoretical models to fit the observational data are necessary (See Chapter 5).

# Chapter 5

# YSOc Spectral Energy Distributions

## 5.1 Main features of Class I Objects

As seen in Chapter 4, typically young stars may conveniently be classified according to their broadband spectral energy distributions (SEDs). In the case of low-mass stars, one useful feature in Class II and III objects is their significant optical emission, which can be associated with T-Tauri stars, either classical or with weak-lines. Besides, their visual spectra do not show significant departures from those that can be obtained from main-sequence stars, taking into account that $A_V$ has already being removed. If there is radiation of these sources at infrared and millimeter wavelenghts, this can be interpreted as an "excess" with respect to main-sequence objects which have a comparable spectral type.

However, the situacion changes radically for more embedded sources: Class 0/I sources. Here the emission at longer wavelengths dominates the energy output, and also, the product $\lambda F_\lambda$ is rising steadily for wavelengths greater than 2.2 $\mu$m. These sources are generally located in the center of the dense cores where the stellar formation takes place, but it is not possible yet call them protostars.

The IR emission of a protostar stems from its dust photosphere, located roughly 10 AU from the star with an effective temperature, $T_{phot}$, of about 300 K. Assuming that the spectrum is a perfect black body characterized by $T_{phot}$, $\lambda F_\lambda$ would peak near $\sim 10\mu$m. However, the emiting regions of that envelope actually include a broad range of temperatures, especially those temperatures are $< T_{phot}$. The net result is that $\lambda F_\lambda$ is predicted to reach its maximum beyond 10 $\mu$m, but should be declining for $\lambda \gtrsim 100$ $\mu$m (Stahler & Palla, 2004). This has been observed in Class I sources, which lead investigators to model their SEDs based on the fact that this sources born from collapsing spherical clouds with or without rotation.

By solving the stellar structure equations (Stahler & Palla, 2004, chapter 11.2.1), a Class I source could be more luminous than a source from Class II or III, if the former is indeed a protostar, and to probe this conclusion, it is necessary to use data from young clusters. These authors cite 2 cases: Taurus-Auriga (Kenyon et al., 1990) and $\rho$ Ophiuchi (Wilking et al., 1989).

In the first case, the conclusion is that Class I sources are not brighter, since their bolometric luminosity function is quite similar to Class II. The second case shows that Class I sources are brighter than Class II objects. Besides, here Class III sources have higher luminosity that the other two sets. It is important to note that this system has more stars than Taurus-Auriga and the extinction in the optical and IR wavelengths is higher, so it is necessary to be careful with the observed spectra and differentiate the circumstellar dust emission with the interstellar one. The sources from Class I in this region can represent a set of bright stars heavily oscured that are near the Zero Age Main Sequence (ZAMS). So, in principle, Class I sources and protostars are not the same, since these sources represent pre-main sequence objects heavily extincted without optical spectra. The typical luminosity of a Class I source with milimeter data gives information about the amount of dust warmed by the star.

## 5.2 Modeling Spectral Energy Distributions in Class I objects

Suppose a case where a Class I source can be considered as a pre-main-sequence star located inside a residual, dusty envelope.

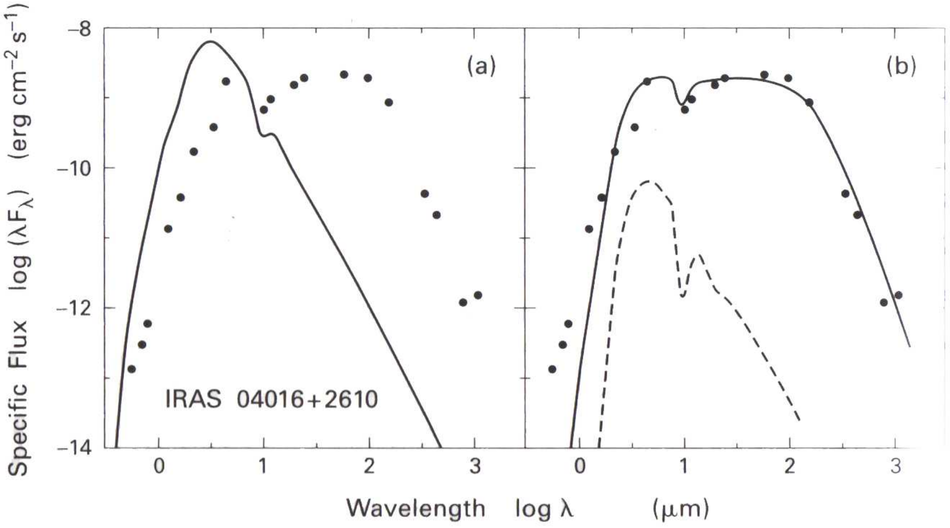

Figure 5.1: Spectral energy distributions of the Class I source IRAS 04016+2610 in L1489. (a) The solid curve shows the spectrum from an extincted, background star. (b) The spectrum from a star embedded within an optically thick dust shell. The dashed curve is the contribution from attenuated starlight alone. Empirical data from Figure 1 of Ladd et al. (1991). Profiles are based on numerical calculations by Stahler & Palla (2004).

Although there is not enough theory yet which can give enough information about the remanent dense core that survives in the main accretion phase, it is useful to know from an empirical point of view how to set the elements from a model with the aim to match the observed IR emission.

Fig. 5.1 shows the spectral energy distribution of the IRAS source 04016+2610 from the dense core of Taurus-Auriga (Kenyon et al., 1990) cited by Stahler & Palla (2004), where the interstellar extiction towards the center of the core is 10 mag and any other emission from the exterior should only be detectable at IR and longer wavelengths.

The important thing to note is that an attenuation of the background starlight gives as result a broadband spectrum that is very sharply peaked and narrow. For this reason, is not possible to obtain the relatively high level of emission observed at longer wavelengths. The form of the Class I spectra tell us that this objects can be formed in a large range of temperatures and they are not characterized by a single temperature that comes from the photosphere. The most probable origin of the observed components at long wavelengts are the heated dust grains, which should be near of the star embedded in the cloud.

The dust can be arranged around the star, in an spherical and optically thick shell. In this model it is feasible to assume that the density of the distribution of matter within the shell varies inversely with radial distance to the star. The use of heated dust as a source of emission can broaden the model spectrum. The attenuated starlight alone contributes to only a portion of the near-infrared flux of the spectrum, and the left part comes from hot grains and the scattering produced at shorter wavelengths. It is possible find other models with different features that can fit equally well the observed spectrum.

## 5.3 Measuring the dust emission in Class 0 Objects

The main features of Class 0 sources are the following: no flux at all is detectable for wavelengths shorter than 10 $\mu$m, these sources drive well-colimated molecular outflows and the measured velocities in these objects are much higher than those near less embedded stars. All this suggests that these sources are in a very early and vigorous phase of evolution. Their spectra at infrared and millimeter wavelenghts arises from warmed dust and have a higher luminosity than a Class I source at $\lambda > 350$ $\mu$m. In particular, millimeter data are useful to explore the internal clump structure.

An example of a typical Class 0 source is the embedded star in the Bok globule B335 (Chandler et al., 1990) cited by Stahler & Palla (2004). Fig. 5.2 displays the SED of that object. Note that in this type of sources $\lambda F_\lambda$ peaks in wavelengths longer than in a Class I source, and all the distribution is much narrower. However, is not possible that the high extinction in the near and mid infrared wavelengths be interstellar, since the globule itself appears isolated with a more extended molecular envelope.

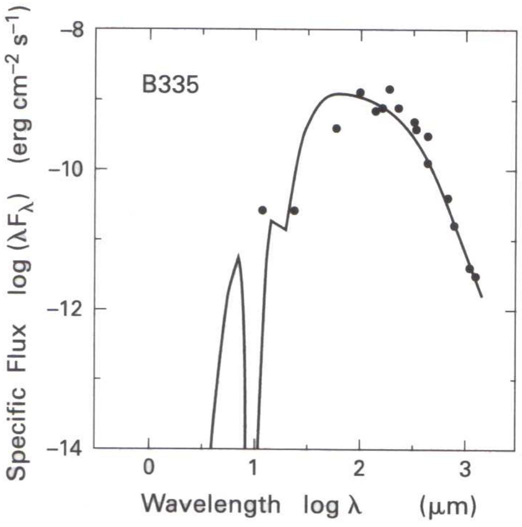

Figure 5.2: Spectral energy distribution of the Class 0 source in B335. The solid curve is the theoretical result for a star in the center of a spherical dust shell. Empirical data taken from Figure 4 of Chandler et al. (1990), and theoretical curve based on numerical calculations by Stahler & Palla (2004). It indicates the emergent flux for a model with a circumstellar extinction of $A_V = 320$ mag and the optical depth falling to unity only at $\lambda = 80\ \mu$m.

The protostar phase can be summarized in the following way. After the gathering of enough material from a cloud in a short and fast phase, a protostar starts to form at the center of a dense core in collapse. Through an accretion shock front, the cloud matter impacts in this protostar. This shock generates photons which heat the incoming gas, thus destroying dust grains in a radius of $\sim$0.1 AU. The generated luminosity spreads through the dusty envelope and emerges as radiation in infrared wavelengths.

Because of the latter, the shock front losses a lot of energy that leads to form a protostellar radius, which is not big enough yet to be considered as a star in the main sequence phase. This object starts to grow in size and mass, and reaches the point where deuterium eventually ignites and drives the convection phase. The energy obtained from deuterium fusion likely limits the stellar radius of the object as a function of the mass. In the case of an intermediate-mass object, convection phase ends while deuterium still burns in an interior shell. If more material is accreted, the protostar contracts until the hydrogen starts the ignition. In the case of a massive object, like the precursor of an O star, the protostar would repel its infalling envelope using wind and radiation pressure.

Disk arise in the protostellar evolution phase and forms from the infalling material, this material has too much angular moment and cannot impact the star itself. These structures evolve quickly and the streamlines from the outer disks collide and forms a ring, which feeds matter onto the central star. Sometime after this stage, the disk becomes gravitationally unstable. It is believed that after that, there are spiral waves that create torques and may facilitate mass transfer and continue the protostellar accretion.

## 5.4 Observed SEDs of AzTEC sources

To construct SEDs (Spectral Energy Distributions) for the 12 YSOc, the online YSO SED Fitting Tool developed by Robitaille et al. (2007) was used creating an account in the webpage: *http://caravan.astro.wisc.edu/protostars/sedfitter.php*. The tool is a grid of models covering a range of stellar masses (from 0.1 to 50 $M_\odot$) and evolutionary stages (ages from $10^3$ to $10^7$ yr), with 10 viewing angles for each model based on the position of the disk, giving a total of 200 000 models to fit. In these models, Whitney et al. (2004) assumed that disk accretion occurs for stars of any mass, with physical properties that scale with mass and agree with observations. They also mention that the outer envelope radii are left large, since the hotter stars will heat up the surrounding ambient material out to several parsec, and that envelope masses of the high stellar temperature models are large because of the large outer radii.

Once logged in, the tool was user-friendly. The page has an option called *Add a new source*, where the flux data from Table 3.9 were introduced to construct the SED for each of the 12 selected YSOc from Visual Inspection. The first step is to fill in the blank spaces with the photometric data. It is useful to specify a *Label* and the *Source Name* for an easier identification of the introduced stellar object. In *Measurement*, it must be determinated if the recolected data has a known *Broad/Narrow* band or if is *Monochromatic*. Almost all data of the YSOc have a band that can be selected in the web page, except for AKARI (9 and 18 $\mu$m) and AzTEC (1.1 mm). For these cases, the *Monochromatic* option was selected in order to put the value in $\mu$m of these bands. Follows the selection of the appropiated units in which data are expressed in the *Flux*/*Magnitudes* space, as well as to write the aperture values of each band in the *Aperture* section. Some fitting tests were made and it was found that 24 $\mu$m flux values are lower that the expected value from the fitted model. In these cases, a lower limit with a confidence of 100% was used in order to obtain a better fit from the tool. For AzTEC sources 004, 017, 035 and 071, it was observed that they could have at least two possible counterparts; in these cases, an upper limit in their millimeter flux was used with a confidence of 50%. In all other fluxes, it was not necessary to use limiting values.

Recently, this region was observed with PACS and SPIRE instruments onboard *Herschel* space telescope, and the flux in five FIR bands 70, 160, 250, 350, 500 $\mu$m (Ohlendorf et al. (2012), Gaczkowski et al. (2013)), and in some cases 870 $\mu$m from LABOCA sub-millimeter observations (Preibisch 2011) coincident –based on coordinate matching within a tolerance of 15 arcsec– with the AzTEC YSOc sample, were included in the SED fit with an uncertainty of 10%. These fluxes are detailed in Table 5.1.

In the *Distance range* space was introduced the aproximated distance in which our studied YSOc are located. The interval of distance used was from 2.254 to 2.346 kpc, assuming that all YSOc are part of the same molecular cloud located at a distance of 2.3 kpc and within a ±5 % that covers error estimations (Allen & Hillier, 1993;

Smith, 2002, 2006). In the *Interstellar* $A_V$ *range* space it is necessary to specify the aproximated extinction around the source; here, using the previously estimated values listed in Table 4.2, it was defined a range $A_V$ -5 to +10 mag.

Finally, the tool asks if *Are any of the apertures smaller than the apparent extent of the source?* The page mentions that this is useful if for example I have different flux measurements in the same filter for different apertures. But, since that is not the case for all the bands with data, the answer used is no. After filling all the spaces, the options *Save the data* or *Save and fit the data* are available. If the last one is used, the tool finds the most appropiate models that describe and fit the introduced data to build the SEDs.

The second step involves fitting the data, giving in a new page a *SED preview* of the best fitting model obtained for the introduced data. Before going to the *Results* part, the page gives the option to do *Customized SED plots*. Following the corresponding link, it is possible to change the wavelength range in $\mu$m and the flux range in ergs/cm$^2$/s, as well as download a new graph of the first SED shown. The graph range was selected to be from 0.1 to 5000 $\mu$m, and the flux range from $10^{-15}$ to $10^{-8}$ ergs/cm$^2$/s for all the millimeter sources, in order to visualize differences between their SEDs. The range of the models used to obtain the SEDs of AzTEC sources is $\chi^2/\nu - \chi^2_{best}/\nu < 3$, where $\nu$ is the number of data points. Figure 5.3 shows the SEDs of the selected 12 YSOc.

In the *Results* part, a table which lists the top 10 models that fit the data is shown. For each fit there is a link that will open up the SED at the correct viewing angle. The first one is the best fit-model, so following the link opens a new window, which shows the plot for the model and several physical parameters obtained for the fitted source.

A summary of physical parameters from the best fit of the 12 selected candidates are described in Table 5.2. The rest of AzTEC sources with S/N $\geq$ 4, but not selected in this sub-sample of YSOc, have been considered as starless cores, which will be analyzed in Chapter 6.

Table 5.1: Sub-millimeter fluxes used to fit SEDs for YSOc from Herschel data from Ohlendorf et al. (2012) and Gaczkowski et al. (2013). All fluxes are en Jy.

| **AzTEC source** | **f70** | **f160** | **f250** | **f350** | **f500** | **f870** |
|---|---|---|---|---|---|---|
| 004 | 9.06 | 49.5 | 76.0 | 44.5 | 39.0 | – |
| 017 | 129 | 132 | 67.9 | 29.7 | 12.2 | – |
| 023 | 103 | 120 | 59.9 | 23.2 | 9.32 | 1.90 |
| 026 | 25.4 | 70.5 | 43.9 | 25.6 | 11.4 | – |
| 033 | 1.98 | 44.4 | 55.0 | 26.6 | 12.0 | 1.89 |
| 035 | 33.4 | 49.8 | 36.2 | 19.6 | 10.5 | 2.09 |
| 044 | – | 35.1 | 35.9 | 10.4 | 34.4 | – |
| 052 | 5.72 | 21.2 | 22.3 | 18.3 | 10.0 | – |
| 060 | – | 12.7 | 17.4 | 11.4 | – | – |
| 071 | – | 14.1 | 14.0 | 17.7 | – | – |
| 087 | – | 7.64 | 12.2 | 12.8 | 8.18 | – |
| 132 | 11.4 | 20.9 | 17.8 | 10.9 | 7.56 | – |

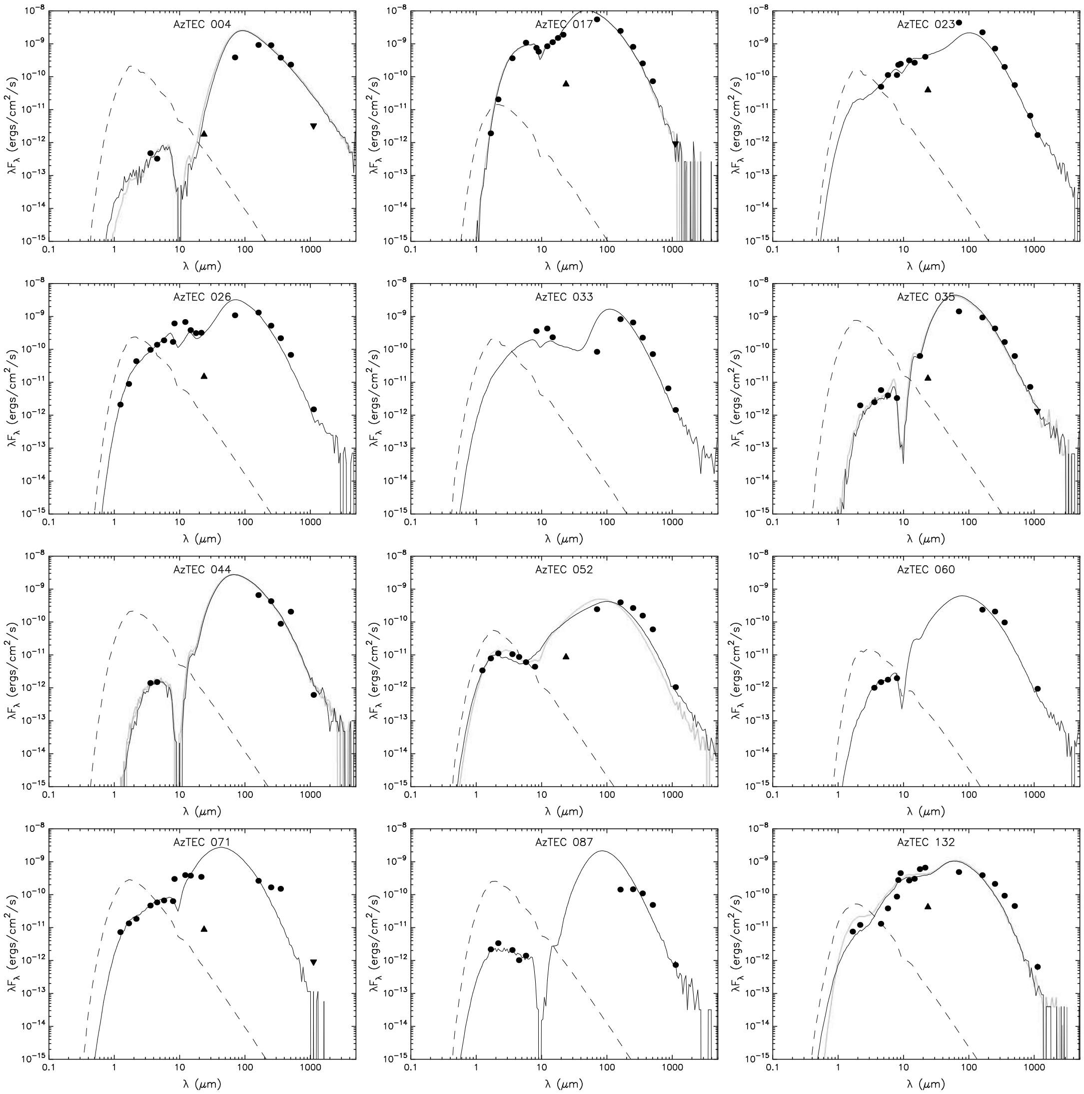

Figure 5.3: SEDs from 12 YSOc described in Table 3.9. The filled circles show the input fluxes at IR and millimeter bands. The black line shows the best fit, and the gray lines show subsequent good fits, if they are present. The dashed line shows the stellar photosphere corresponding to the central source of the best fitting model, as it would look in the absence of circumstellar dust, but including interstellar extinction.

It is important to note that the stellar mass from SED fitting indicates the final mass when the source reaches the ZAMS, and is not the protostellar mass accreted until this moment. The age is estimated from evolutionary tracks which are very basic, and they have a constant mass. Since the Robitaille et al. (2007) models have accretion from envelopes and disks, there is no really way to know the present mass at a given model (Robitaille's personal communication).

Table 5.2: Physical parameters obtained from SED fitting of the YSOc based in $A_V$ values from Table 4.2.

| **AzTEC** | **# SED** | **Stellar** | | **Disk** | | | | | **Envelope** | | | **Total** | $A_V$ | |
|---|---|---|---|---|---|---|---|---|---|---|---|---|---|---|
| **Source** | **Model**[a] | **Age** | **Mass** | **Mass** | $r_{out}$ | $r_{in}$ | **Acc. rate**[b] | **Incl.** | **Mass** | $r_{out}$ | **Acc. rate**[c] | **Lum.** | **Circ.** | **IE.** |
| | | ($10^3$ yr) | ( $M_\odot$ ) | ( $10^{-2} M_\odot$ ) | (AU) | (AU) | ($10^{-7} M_\odot/yr$) | (deg) | ( $M_\odot$ ) | ($10^4$ AU) | ($10^{-4} M_\odot/yr$) | ( $10^2 L_\odot$ ) | ($10^2$ mag) | (mag) |
| 004 | 3007873 | 2.4 | 4.23 | 15.00 | 8.0 | 7.9 | 744.00 | 41.41 | 22.9 | 0.6 | 14.50 | 5.5 | 37.4 | 10.00 |
| 017 | 3014060 | 177.0 | 8.20 | 0.02 | 54.4 | 24.9 | 0.04 | 69.51 | 145.0 | 9.3 | 3.38 | 45.6 | 0.2 | 17.33 |
| 023 | 3002592 | 10.7 | 5.22 | 34.20 | 23.3 | 1.3 | 176.00 | 18.19 | 225.0 | 2.4 | 18.80 | 3.7 | 5.8 | 11.17 |
| 026 | 3004971 | 8.9 | 7.32 | 5.69 | 57.3 | 1.6 | 26.80 | 18.19 | 160.0 | 4.3 | 6.54 | 5.9 | 4.8 | 13.38 |
| 033 | 3017324 | 7.0 | 4.63 | 0.77 | 19.4 | 1.1 | 15.30 | 18.19 | 180.0 | 1.9 | 19.50 | 2.8 | 27.2 | 9.50 |
| 035 | 3018159 | 3.3 | 7.81 | 9.35 | 3.9 | 2.2 | 74.40 | 63.26 | 104.0 | 5.2 | 3.37 | 11.2 | 5.3 | 10.00 |
| 044 | 3011148 | 51.5 | 7.90 | 0.75 | 30.3 | 1.9 | 6.96 | 87.13 | 343.0 | 10.0 | 4.30 | 7.9 | 1450.0 | 12.00 |
| 052 | 3011153 | 14.8 | 2.31 | 1.85 | 46.5 | 0.6 | 6.84 | 18.19 | 223.0 | 2.9 | 9.53 | 0.7 | 2.4 | 9.00 |
| 060 | 3017927 | 87.3 | 5.07 | 18.40 | 285.0 | 77.5 | 0.25 | 31.79 | 151.0 | 4.4 | 5.25 | 1.5 | 0.8 | 25.50 |
| 071 | 3008570 | 69.9 | 7.89 | 0.61 | 79.8 | 2.2 | 0.16 | 75.52 | 8.1 | 3.4 | 0.54 | 10.3 | 0.6 | 9.00 |
| 087 | 3003388 | 29.7 | 7.66 | 18.40 | 44.0 | 3.1 | 2.37 | 49.46 | 51.6 | 1.3 | 15.00 | 5.5 | 4.3 | 11.00 |
| 132 | 3008375 | 286.0 | 6.27 | 0.03 | 54.9 | 45.7 | 0.18 | 81.37 | 20.2 | 8.5 | 0.11 | 6.6 | 0.3 | 11.25 |

---

[a] Robitaille et al. (2007)

[b] The mass transport rate from the disk to the stellar surface.

[c] The mass transport rate from the envelope to the disk.

As can be seen in Table 5.2, the stellar masses range from 2.31 to 8.20 $M_\odot$, with $\sim 42\%$ between 7 and 8 $M_\odot$, as an indicative that in the Carina SPR the embedded ongoing star formation is mainly of intermediate-mass, according with the definition of massive stars in Table 1.1. Stellar ages vary from 2.39 $\times 10^3$ to 2.86 $\times 10^5$ yr, which results in a sample of pre-main sequence sources.

Using the definition of Stage O/I, II and III suggested by Robitaille et al. (2006), all the sources are in Stage 0/I ($\dot{M}_{env}/M_* > 10^{-6}$ yr$^{-1}$). Note that all them have disks according to the fitted model, which have masses between 0.02 and 34.20 $\times 10^{-2}$ $M_\odot$, being from 0.61 to 18.4 $\times 10^{-2}$ $M_\odot$ the disk mass range for YSOc with masses between 7 and 8 $M_\odot$. Disk accretion rate, defined as the mass transport rate from the disk to the stellar surface has a range 0.04 – 744 $\times 10^{-7}$ $M_\odot$ yr$^{-1}$ with less than $10^{-5}$ $M_\odot$ yr$^{-1}$ present in about 80% of the sources. Envelope accretion rate, defined as the mass transport rate from the envelope to the disk has a range 0.11 – 19.50 $\times 10^{-4}$ $M_\odot$ yr$^{-1}$, with the value $10^{-4}$ present in 50% of the sources. As it was mentioned in Chapter 1, typical mass accretion rates for high-mass stars are as high as $10^{-2}$ $M_\odot$ yr$^{-1}$, whereas for low-mass stars a typical value is $\sim 10^{-6}$ $M_\odot$ yr$^{-1}$. Carina SPR YSOc are just in the middle of these two limits (See Table 5.3).

Table 5.3: Summary of physical parameters of YSO candidates.

| Stellar Mass | Age ($10^3$ yr) | Disk Mass ($10^{-2}$ $M_\odot$) | Disk Acc. rate ($10^{-7}$ $M_\odot/yr$) | Envelope Mass ($M_\odot$) | Envelope Acc. rate ($10^{-4}$ $M_\odot/yr$) | Total Luminosity ($10^2$ $L_\odot$) |
|---|---|---|---|---|---|---|
| $<$ 7 $M_\odot$[a] | 2.4 – 286 | 0.03 – 34.2 | 0.18 – 744 | 20.2 – 225 | 0.1 – 19.5 | 0.7 – 6.6 |
| 7 - 8 $M_\odot$[b] | 8.9 – 69.9 | 0.61 – 18.4 | 0.16 – 74.7 | 8.1 – 343 | 0.5 – 15 | 5.5 - 11.2 |
| $>$ 8 $M_\odot$[c] | 177 | 0.02 | 0.04 | 145 | 3.4 | 45.6 |

[a] AzTEC 004, 023, 033, 052, 060, 132
[b] AzTEC 026, 035, 044, 071, 087
[c] AzTEC 017

The total luminosity ranges from a few $10^2$ to a few $10^3$ $L_\odot$. This value will be compared with other samples in Section 5.5. The interstellar extinction resulting from SED fit is listed in the last column of Table 5.2, generally differs from the original input value.

## 5.5 Is Lada's Classification valid for Intermediate-mass YSOs?

From the analysis and results of previous chapters, an important question arises: is the Lada classification valid for intermediate-mass objects?

Theoretically not, because several characteristics of massive (more than 8 $M_\odot$) stellar objects are not clear yet. One of them is the formation of a circumstellar disk around a massive star. Zinnecker & Yorke (2007) mention that if the primary source of the massive star's material is accretion from the surrounding molecular core, then a circumstellar disk should be the natural consequence of the star-formation process even in the high-mass case. However, it should be difficult to observe disks around massive stars. The high far UV and extreme UV fluxes associated with high-mass stars will begin to photoevaporate the disks on timescales of $\sim 10^5$ yr (Hollenbach et al., 2000).

The results will be observable as deeply embedded ultracompact HII-regions with comparable lifetimes (Richling & Yorke, 1997). The fact that disks around O stars photoevaporate so quickly provides negative feedback for disk accretion. This limits the build-up of more massive stellar objects and may even imply an upper mass limit for star formation.

Another problem lies in the time that a stellar object takes to reach the zero-age main sequence (ZAMS). An inspection of some results from classical models shows that the amount of time required for stars to collapse onto the ZAMS is inversely related to mass. Figure 5.4 shows some pre-main sequence evolutionary tracks for the sequence of masses from Table 5.4.

Table 5.4: Pre-main sequence contraction times for the classical models presented in Figure 5.4 (Data from Bernasconi & Maeder, 1996)

| Initial mass ($M_\odot$) | Contraction Time (Myr) |
|---:|---:|
| 60 | 0.0282 |
| 25 | 0.0708 |
| 15 | 0.117 |
| 9 | 0.288 |
| 5 | 1.15 |
| 3 | 7.24 |
| 2 | 23.4 |
| 1.5 | 35.4 |
| 1 | 38.9 |
| 0.8 | 68.4 |

In Table 5.4, is shown that 1 $M_\odot$ star takes almost 39 Myr to reach the ZAMS, whereas a 9 $M_\odot$ makes it to the ZAMS in only ~290 000 yr. This inverse relationship between star-formation time and stellar mass may also signal a problem with classical pre-MS evolutionary models.

The reason is that if the most massive stars do indeed form first in a cluster of stars, the intense radiation that they produce would likely disperse the cloud before their low-mass siblings would ever have a chance to develop. Then, it will be necessary to take into account in the models other features such as rotation, turbulence and magnetic field, together with environments that contain strong stellar winds and ionizing radiation from nearby, massive stars. Observationally, because (unless that we adjust a lot of photometric data) we do not know in principle the mass of the observed objects. So, is necessary to make an analysis of the IR colors that permit us to identify the most reddened (embedded) and young objects. The YSOs asociation with emission in the millimeter range indicates the presence of envelopes, and likely, circumstellar disks. Actually, it is observationally unknown the limit mass which a disk can be formed.

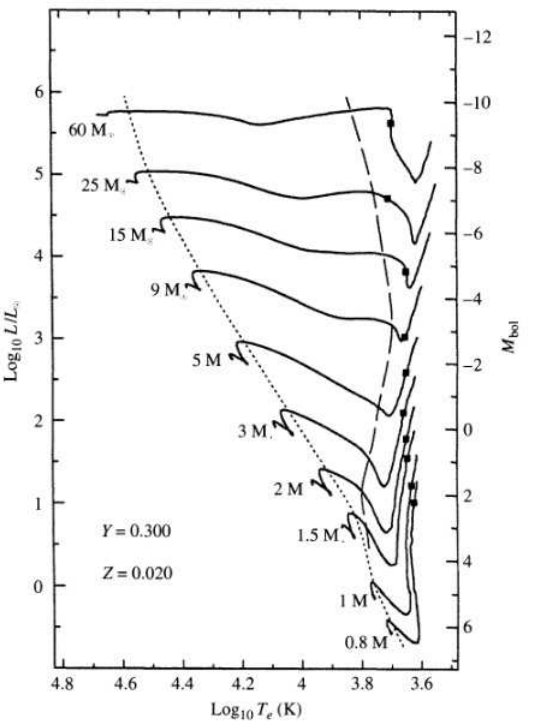

Figure 5.4: Classical pre-main sequence for stars of various masses with the composition X=0.68, Y=0.30, and Z=0.02. The direction of evolution of each track is generally from low to high effective (right to left). The mass of each model is indicated beside its evolutionary track. The square on each track indicates the onset of deuterium burning in these calculations. The long-dash line represents the point on each track where convection in the envelope stops and becomes purely radiative. The short-dash line marks the onset of convection in the core of the star. Contraction times for each track are given in Table 5.4 (Figure adapted by Carroll & Ostlie (2007) from Bernasconi & Maeder, 1996)

An interesting fact seen is that by using repeatedly the Online SED Fitter made by Robitaille et al. (2007), it is possible to observe that the presence of the submillimeter and AzTEC fluxes are very important to obtain only one model with a good fit, even in the case that only the studied object has 3 or 4 IR fluxes. Namely, without the sub millimeter and millimeter fluxes, the number of models that can be fitted can increase, causing a higher uncertainty in the values of the theoretical physical parameters that describe the object in question.

Even in the case that only one well fitted model is present in fits with and without sub-millimeter and millimeter flux, the physical parameters in both fits can be different. For example, if the SED of source AzTEC 071 is presented with sub-millimeter and millimeter data, mass and age parameters of the star from the best fit are 7.89 $M_{\odot}$ and $6.99 \times 10^4$ yr respectively, whereas that the parameters for the best fit WITHOUT these fluxes are 6.03 $M_{\odot}$ and an age of $4.07 \times 10^4$ yr. For this reason, is important to assign correctly the IR counterpart with the AzTEC sources, since a bad match would lead to a wrong interpretation of non-existent sources, based in the physical parameters of the fitted SEDs of these sources. The above visual inspection of invidual images of AzTEC sources, and their counterparts in IRAC, 2MASS and MIPS24 maps (see Fig. 4.8) permit to assess if the asociation done is highly probably or not.

Besides of the position and the separation of the IR sources with respect to the mm-emission, Lad's classification in both, the IR source and the surrounding sources, as well as the mm-core morphology can help to determine if the correspondence is good or not. Of course, in the cases where there is a higher uncertainty, other observations (for example, observed molecular lines associated to the core, presence of masers bound the position of both, IR and mm sources, etc.) will be necessary to determine if IR objects are in the line of sight of background cores or if the object is a YSO with a significant envelope (and a possible disk) of dust.

Originally Andre et al. (1993) found a new class of YSOs: Class 0, distinguished as sources without emission at $\lambda < 10$ $\mu$m, very low values of the ratio $L_{submm}/L_{bol}$, where $L_{bol}$ is bolometric luminosity, and $L_{submm}$ the luminosity radiated longward of 350 $\mu$m; as well as a SED dominated by thermal emission from cold dust in the envelope, that is $M_{env} > M_{\star}$ (Andre et al., 2000). In principle, these definitions are valid in the range of low-mass stars, but they also have been applied in regions of intermediate-mass star formation (see Hennemann et al., 2010). A different comparision between Class 0, I and II sources for low- and high-mass was done by Molinari et al. (2008), fitting SEDs between 8 and 1200 $\mu$m, and based on the shape of the SED and the $L_{bol} - M_{env}$ relationship (tools used in low-mass star formation studies). They found that the distribution of massive YSOs specially classified in their diagram, are the high-mass analogues of Class 0, I and II sources in the usual classification established for low-mass YSOs.

All AzTEC YSOc fulfill the condition that $M_{env} > M_\star$ (see Table 5.2), and both conditions: $L_{submm}/L_{tot} > 0.01$ (Hennemann et al., 2010) and $L_{submm}/L_{tot} > 0.005$ (Andre et al., 2000). Our sample of sources ranges $0.023 < L_{submm}/L_{tot} < 0.35$.

A comparision between $M_{env}$ vs $L_{tot}$ diagram from Molinari et al. (2008) and our data is shown in Figure 5.5, here AzTEC YSO candidates (YSOc) fall in the range of intermediate-mass stars. YSO candidates 026, 035, 044 and 087, which have masses between 7 and 8 $M_\odot$ fall close to the dashed line for massive millimeter sources. The exception is AzTEC 071, whose behavior could be due to the poor fitting in the sub-millimeter and millimeter fluxes of the envelope, where it flattens shape (see Figure 5.3) probably due to a temperature gradient in the envelope, or the flux contribution from a companion. On top of Figure 5.5, different models (continuous line starting with dots, left to right) are for different initial envelope masses of 80, 140, 350, 700 and 2000 $M_\odot$, which correspond to stellar masses of 6.5, 8, 13.5, 18 and 35 $M_\odot$ (see Table 7 from Molinari et al. (2008)). All YSOc in AzTEC sample are in agreement with the locus of this diagram.

In summary, the AzTEC YSO candidates sample can be considered as intermediate-mass Class 0 objects according to Andre et al. (1993) definition, and the physical values fitted from their SEDs (see Table 5.3) are in agreement with those from other authors (Molinari et al., 2008, and reference therein.).

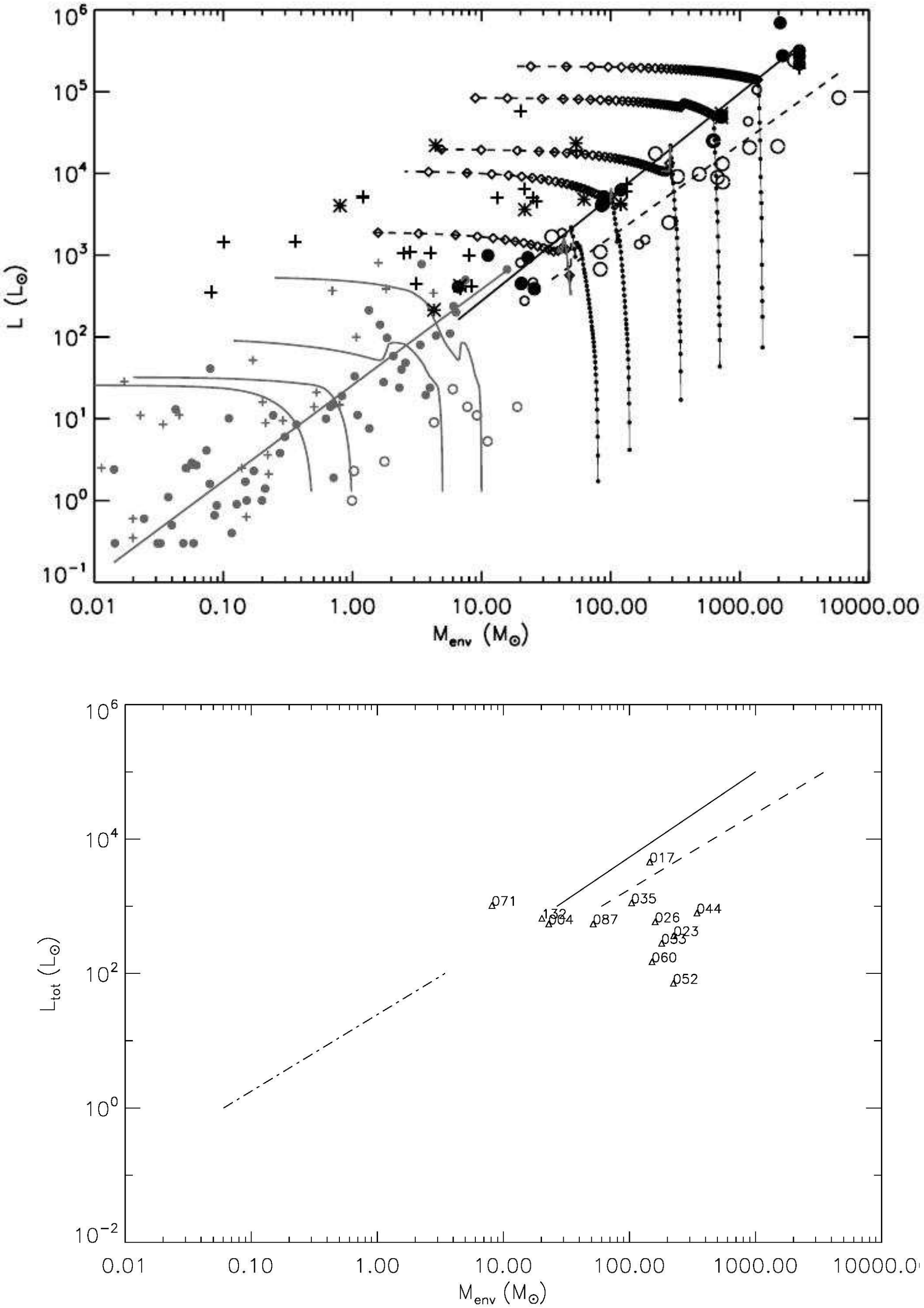

Figure 5.5: *Top:* $M_{env} - L_{bol}$ diagram from Fig. 9 Molinari et al. (2008). *Bottom:* $M_{env} - L_{bol}$ diagram for fitted YSOc. As in top diagram, dot-dashed line delimits Class 0 (below the line) and Class I (above the line) sources for low-mass stars, whereas the upper lines, dashed and continuous, are the least squared fits for Class 0 and I sources for high-mass stars.

# Chapter 6

# Dust cores

Dense prestellar cores, from which a new generation of stars will form, represent a very early stage of the low- and high-mass star formation process, before collapse results in the formation of a central protostar. The mass and spatial distributions of these prestellar cores retain imprints of their formation process, and their lifetime is extremely sensitive to the dominant physics controlling their formation. While the properties of star-forming cores depend strongly on the physical processes leading to their formation, core initial conditions in turn help to determine the evolution of newly formed protostars. Millimeter emission, in particular, traces the dust in dense stellar cores and protostellar envelopes, and provides a measure of core and envelope properties, including sizes, masses and spatial distribution (Enoch et al., 2009).

Little is known for the very earliest stages in the formation of massive stars; in particular the conditions inside the early protostellar core and the presumed prestellar cores. These objects are expected to be massive and cold (cf. McKee & Tan, 2003), with typical temperatures expected to be $\sim$20-30 K.

## 6.1 Dust mass of millimeter cores

As described by Estalella & Anglada (1996), the most important emission process in the continuous infrared and (sub-)millimeter wavelengths in star forming regions, is the thermal radiation that comes from the dust grains. Dust can be found in the interstellar medium in an approximate proportion of $1\%$ compared to the gas mass. The small dust particles (with sizes from $\sim 0.01$ to $0.1$ $\mu$m), that exist within the molecular clouds, absorb with great efficiency the stellar radiation in shorter wavelengths than its size, and when the cooling and heating processes are in balance, the dust particles re-emit the radiation as continuous emission mainly in larger wavelengths. The final spectrum is very similar to a black body characterized by a dust temperature $T_d$, modified by the effect of an absorption coefficient which depends on the frequency or the wavelength (a gray body).

So, the observed flux at a given frequency $\nu$ (or wavelength $\lambda$) can be obtained using the following expression:

$$S_\nu = B_\nu(T_d)\left(1 - e^{-\tau_\nu}\right)\Omega_s \tag{6.1}$$

where $B_\nu(T_d)$ is the Plank function using the dust temperature $T_d$, $\Omega_s$ is the solid angle of the source and $\tau_\nu$ is the optical depth. It is possible to obtain an expression for $\tau_\nu$ knowing the relationship between gas and dust, and the efficiency of the dust extinction in the $\nu$ frequency. Considering that $\tau_\nu$ is proportional to the columnar density and that the proportionality factor varies with the frequency as $\nu^\beta$, $\beta$ with values between 1.5 and 2, the equation is:

$$\tau_\nu = \kappa_\nu \int_{visual} \rho dl \tag{6.2}$$

where $\kappa_\nu$ is the absorption coefficient by mass unit of total density (in mass) of dust and gas, $\rho$, and the integral $\int_{visual} \rho dl$ is the columnar density (in mass) of gas and dust. Also, from sub-millimeter wavelengths onwards, the emission is considered optically thin, so that $\tau_\nu \ll 1$ and $e^{-\tau_\nu} \simeq 1 - \tau_\nu$. It is also assumed that $T_d$ and $\kappa_\nu$ are independent of position within a core. Using the above equations, the expression for the flux is then:

$$S_\nu = B_\nu(T_d)\tau_\nu\Omega_s = B(T_d)\kappa_\nu \frac{A}{D^2}\int \rho dl = B(T_d)\kappa_\nu \frac{M_d}{D^2} \tag{6.3}$$

where $M_d$ is the mass of the dust core, and $D$ is the distance from us to the object. Since we are in the millimeter range, is possible to use the Rayleigh-Jeans approximation for $B_\nu(T_d)$, and solving the above equation for $M$ gives:

$$M_d = \frac{D^2 S_\nu}{B\left(T_d\right)\kappa_\nu} \tag{6.4}$$

The definition of millimeter cores used in this thesis was suggested by di Francesco et al. (2007), in which a millimeter core that contains a compact luminous internal source (i.e., an embedded protostar) is defined as "protostellar core", the final nature of the stellar object would be stellar or substellar, as is the case of the 12 YSOc discussed in Chapter 5). The "starless" core definition is used to refer to dense cores without an internal luminosity source, and the "prestellar cores" one as starless cores that are likely to be gravitationally bound (see Enoch et al., 2008). This last category, however, is not possible to investigate only with millimeter data, it requires high density molecular line observations. Thus, to use the same nomenclature, the AzTEC sources without IR counterparts will be identified as **starless cores**.

## 6.2 Mass and density of millimeter cores

To calculate the mass of millimeter cores, equation 6.4 was used, based on values used by Enoch et al. (2008). The value of $\kappa_{1.1mm} = 0.0114$ g$^{-1}$ cm$^2$ was interpolated from column 5 Table 1 of Ossenkopf & Henning (1994) for dust grains with thin ice mantles, plus a gas-to-dust mass ratio of 100. The value of $T_d$ used depends on whether a core is starless or has an internal source of luminosity. Enoch et al. (2008) used a slightly higher temperature for protostellar cores ($T_d = 15$ K) than for starless cores ($T_d = 10$ K). The millimeter AzTEC sources without counterpart in other IR wavelengths, as well as the ones without a visible counterpart in Spitzer images (see Chapter 4) were assumed to be starless cores[1] , so the used value for $T_d$ was $10$ K, and the distance to Carina Nebula as $D = 2300$ pc. The obtained masses of the cores are listed in Table 6.1.

The following variables are related to the dust and total mass estimation of the studied cores (Equation 6.4), which are discussed in more detail:

- $\kappa_V$ value: To a lesser extent, $\kappa_V$ also modifies the mass of the cores. Enoch et al. (2008) used a value of $\kappa_{1.1mm} = 0.0114$ cm$^2$ g$^{-1}$, and also mentions that Shirley et al. (2011) gets a value of $\kappa_{1.1mm}$= 0.0088 cm$^2$ g$^{-1}$ based on measurement of near-IR data and 450 and 850 $\mu$m SCUBA maps of the low-mass Class 0 core B335, which would increase the values of the mass cores by ~1.3 times. Similar sub-millimeter observations on South Pillars might also modify our estimated physical parameters.

- Distance: Due to the low uncertainty to the distance of Eta Car (5%), core mass does not change considerably. For a 1000 $M_\odot$ core, an uncertainty of $\pm$ 115 pc (5% of 2300 pc) would imply a mass uncertainty of $\pm$ 10.25$\%$ ($\sim$100$M_\odot$).

To calculate the core sizes, a projection line along the longer axis was drawn centered in the mm-emission peak in each of the cores by using the AzTEC map and the program DS9. The projection angle is measured in degrees (30, 45, 60, 90, 120, 135, 150, 180) and is taken from West to the North. Projection data files of all millimeter sources with S/N $\geq$ 4 were used to estimate the semi-major axis of each core, then each set of data is fitted with a Gaussian function, and the FWHM radius of the cores is obtained as a better indicative of core size (See Table 6.1).

---

[1] At the time this thesis was concluded, an article about the Herschel FIR observations of the Carina Nebula Complex (CNC) was published (Gaczkowski et al., 2013). 203 Herschel sources lie in the SPR, and from them 23 AzTEC sources considered as a starless core have sub-millimeter counterpart within a tolerance of 15 arcsec. In total, 35/203 Herschel objects have an AzTEC counterpart with S/N $\geq$ 4. 12 YSOc have IR and Herschel fluxes, while 23 AzTEC sources have only Herschel counterparts. These 23 sources probably are not starless cores as they have supposed in this section, but their study will be treated in a future work.

Table 6.1: Physical parameters for millimeter starless cores (S/N $\geq$ 4).

| **# AzTEC** | **Core Mass** $(10^2 M_\odot)$ | **Semi-major axis** (arcsec) | **Inclination angle**[a] (degrees) | **FWHM radius** (arcsec) | **FWHM radius** (pc) | **Density** $\langle n_{H_2} \rangle$ (cm$^{-3}$) |
|---|---|---|---|---|---|---|
| 002 | 224.05 | 24 | 45 | 24.86 | 0.28 | $4.5e6$ |
| 006 | 98.55 | 60 | 90 | 25.33 | 0.28 | $1.9e6$ |
| 015 | 64.23 | 42 | 45 | 23.45 | 0.26 | $1.5e6$ |
| 022 | 56.90 | 36 | 180 | 30.69 | 0.34 | $6.1e5$ |
| 024 | 56.34 | 36 | 60 | 24.36 | 0.27 | $1.2e6$ |
| 027 | 59.51 | 60 | 120 | 43.41 | 0.48 | $2.2e5$ |
| 030 | 51.33 | 36 | 90 | 23.65 | 0.26 | $1.2e6$ |
| 031 | 56.57 | 54 | 90 | 26.65 | 0.30 | $9.2e5$ |
| 034 | 53.54 | 36 | 150 | 25.36 | 0.28 | $1.0e6$ |
| 040 | 50.18 | 54 | 120 | 20.45 | 0.23 | $1.8e6$ |
| 042 | 46.70 | 66 | 90 | 31.61 | 0.35 | $4.6e5$ |
| 046 | 43.20 | 42 | 60 | 36.60 | 0.41 | $2.7e5$ |
| 048 | 39.06 | 36 | 60 | 28.87 | 0.32 | $5.0e5$ |
| 057 | 39.45 | 66 | 90 | 37.62 | 0.42 | $2.3e5$ |
| 063 | 31.82 | 54 | 45 | 75.93 | 0.84 | $2.2e4$ |
| 065 | 33.60 | 36 | 90 | 36.26 | 0.40 | $2.2e5$ |
| 066 | 30.62 | 42 | 60 | 36.13 | 0.40 | $2.0e5$ |
| 070 | 33.25 | 42 | 45 | 35.27 | 0.39 | $2.3e5$ |
| 074 | 29.61 | 42 | 45 | 25.58 | 0.28 | $5.5e5$ |
| 075 | 29.96 | 72 | 120 | 70.53 | 0.78 | $2.6e4$ |
| 079 | 26.42 | 66 | 180 | 29.85 | 0.33 | $3.0e5$ |
| 081 | 30.04 | 42 | 135 | 21.92 | 0.24 | $8.8e5$ |
| 083 | 28.49 | 48 | 90 | 20.84 | 0.23 | $9.7e5$ |
| 086 | 26.25 | 66 | 150 | 50.10 | 0.56 | $6.4e4$ |
| 089 | 27.27 | 36 | 90 | 29.63 | 0.33 | $3.2e5$ |
| 091 | 26.96 | 42 | 45 | 64.30 | 0.71 | $3.1e4$ |
| 095 | 23.91 | 36 | 90 | 38.19 | 0.42 | $1.3e5$ |
| 098 | 26.34 | 48 | 60 | 29.82 | 0.33 | $3.1e5$ |
| 099 | 24.82 | 42 | 180 | 34.62 | 0.38 | $1.8e5$ |
| 107 | 22.03 | 78 | 135 | 68.57 | 0.76 | $2.1e4$ |
| 112 | 23.85 | 42 | 135 | 30.97 | 0.34 | $2.5e5$ |
| 116 | 25.14 | 30 | 90 | 29.09 | 0.32 | $3.1e5$ |
| 117 | 23.30 | 42 | 45 | 41.82 | 0.46 | $9.8e4$ |
| 119 | 20.83 | 42 | 90 | 59.00 | 0.66 | $3.1e4$ |
| 123 | 23.84 | 36 | 45 | 55.28 | 0.61 | $4.3e4$ |
| 128 | 21.34 | 36 | 45 | 36.24 | 0.40 | $1.4e5$ |
| 130 | 20.81 | 54 | 150 | 50.16 | 0.56 | $5.1e4$ |
| 131 | 20.62 | 36 | 90 | 23.93 | 0.33 | $4.6e5$ |
| 135 | 21.78 | 54 | 135 | 24.18 | 0.27 | $4.7e5$ |
| 148 | 18.50 | 42 | 60 | 47.69 | 0.53 | $5.3e4$ |

---

[a] Measured from West to North

Dust mass densities for these cores were estimated by using the equation:

$$\langle n_{H_2} \rangle = \frac{M_d}{\frac{4}{3}\pi R^3 \mu} \tag{6.5}$$

where $M_d$ is the calculated mass from Equation 6.4, $R$ is the radius (full width at half maximum, FWHM) of each mm-core (in cm) and $\mu = 2.29 m_H$ is the mean mass per particle, with $m_H$ being the hydrogen mass. Since a gas-to-dust mass ratio of 100 was assumed, the values obtained for total core mass, size, and mass density oscillate between $1850$ and $10000$ $M_\odot$ (without the value for AzTEC 002, which is known to be a young cluster, Smith et al., 2005), 0.23 and 0.84 pc, and $2.1 \times 10^4$ and $1.9 \times 10^6$ cm$^{-3}$, with average values of 4271 $M_\odot$, 0.38 pc, and $\sim 7.3 \times 10^5$ cm$^{-3}$, respectively.

Both, the total mass of millimeter cores (about $\sim 10^3\ M_\odot$) and density values ($\geq 10^6$ cm$^3$), is in agreement with typical values for massive dense cores that in principle can form high-mass stars. Nevertheless, in contrast with the result that YSOc in the South Pillars Region that are observed to be of intermediate mass, suggest that more than one stellar object might be formed within these millimeter cores. Individual values of core mass, size, and mass densities are given in Table 6.1, and the histograms of these values are presented in Fig. 6.1. Histograms in mass and densities follow the same tendency that there is a peak in the less massive edge and in the less dense edge.

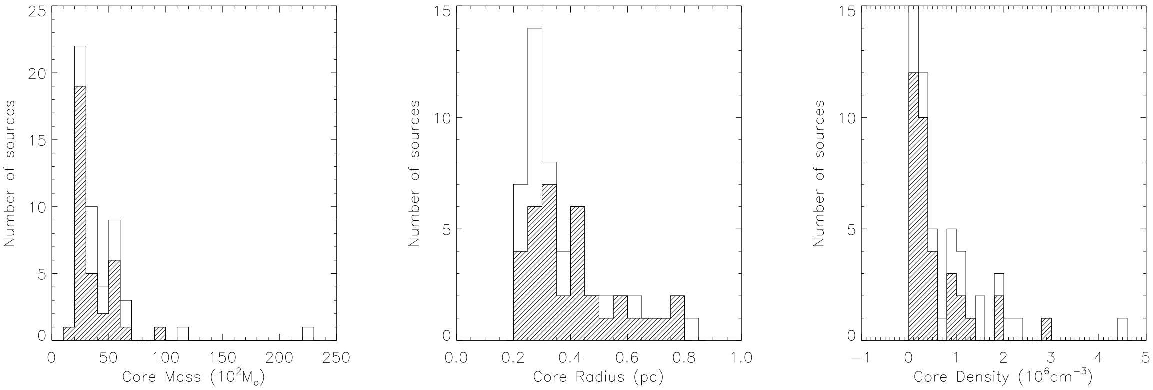

Figure 6.1: Histograms of AzTEC sources (S/N $>$ 4 or Flux 190 mJy) showing mass, radius (sizes), and mass densities distributions. Clear histograms correspond to both, pre-stellar and starless cores, while shadow histograms show only starless cores.

Sources with S/N between 3 and 4 may have an IR counterpart in far-IR wavelengths that might confirm low-mass sources with a possible disk, but these fainter millimeter sources are not considered in histograms, since they can contain several false sources, according to the False Detection Rate test (see Section 3.4.1).

From the values of mass density of millimeter cores at SPR, an intermediate case of physical characteristics between low-mass cores and newborn stellar clusters is observed (see Section 3.1). For a comparison of mass size and density of isolated cores, see Table 6.2 where SPR cores are new born stellar clusters.

Table 6.2: Parameter comparison of cores in two modes of star formation.

| | Mass ($M_\odot$) | Size **(pc)** | Density **(cm$^{-3}$)** |
|---|---|---|---|
| Low-mass cores[a] | 1-10 | 0.1 | $10^4$ |
| AzTEC cores @ SPR | $10^3$–$10^4$ | $0.24 - 0.78$ | $10^4$–$10^6$ |
| Newborn stellar clusters[a] | $10^3$–$10^4$ | $0.5 - 1$ | $10^6$ |

---

[a] Irvine et al. (2005)

The obtained density values for our region can also be compared with those obtained from other authors:

- Young et al. (2006), with Bolocam at 1.1 mm, observed the Ophiuchus region, and obtained density values between $9.0 \times 10^4 - 3.0 \times 10^7$ cm$^{-3}$, with a mean value of $1.6e6$ cm$^{-3}$. Note, however, that Ophiuchus is a star-forming region of low-mass stars.
- Hill et al. (2005), using SIMBA at 1.2 mm, observed 131 star-forming complexes suspected of undergoing massive star formation, and they obtained values for its observed cores between $1.4 \times 10^3 - 1.9 \times 10^6$ cm$^{-3}$, with a mean mean value of $8.7 \times 10^4$ cm$^{-3}$.
- Finally, Motte et al. (2007), with MAMBO@IRAM at 1.2 mm, observed Cygnus X, a high-mass star forming region with several OB associations. The millimeter density values ranges between $1.0 \times 10^4 - 1.0 \times 10^e6$ cm$^{-3}$, with a mean value of $5.0 \times 10^4$ cm$^{-3}$.

This shows that our core characteristics are again between low and high mass star formation mode. Millimeter observations with higher sensitivity and angular resolution are necessary (LMT, ALMA) to judge accurately the nature of all these millimeter sources.

## 6.3 Spatial distribution of millimeter cores

The spatial distribution of AzTEC cores with symbol sizes according with their mass density is shown in Fig. 6.2. From this figure it is possible to divide the core distribution into three groups based on the radial distance to $\eta$ Car in order to see if there is an influence of $\eta$ Car activity:

- The first region is located at a distance ∼7 arcmin (∼4.7 pc) from the star and contains a total of 13 cores. About half of the cores have high densities and three of them lie ∼5.3 arcmin far from $\eta$ Car. All these objects have high masses, highlighting one of them with ∼9900 $M_\odot$ (AzTEC 006), 3 with ∼5000 $M_\odot$ and the rest between 4000 and 2000 $M_\odot$. It also is important to note that although there are several detected IR objects close to $\eta$ Car, none of them lying at a distance smaller than ∼4.5 arcmin has a point millimeter counterpart.
- The second region, at a distance of ∼18.0 arcmin (∼12 pc), covers the position from the Treasure Chest to AzTEC 026. It contains 8 cores, 3 of them having the highest densities (AzTEC 024, 034 and 081) and they are located close to the Treasure Chest, whereas the less dense ones are located close to AzTEC 026. 2 of 8 cores have about 5000 $M_\odot$, whereas the rest have masses between 4000 and 2000 $M_\odot$.

- The third region, located ∼30 arcmin (∼20 pc) from $\eta$ Car, contains the Giant Pillar, and all the detected millimeters objects to the left of this structure. This region presents a variety of density cores with high and low density within the pillar, however, it is important to note that a pair of low density cores are located at the peak of the Giant Pillar (AzTEC 066 and 075). A notable feature of the four millimeter cores (AzTEC 031, 083, 107 and 112) located to the left of the Giant Pillar is that they are close to a bright nebulosity seen in 24 $\mu$m.

Apparently, there is not a clear clue of a sequential star formation around $\eta$ Car.

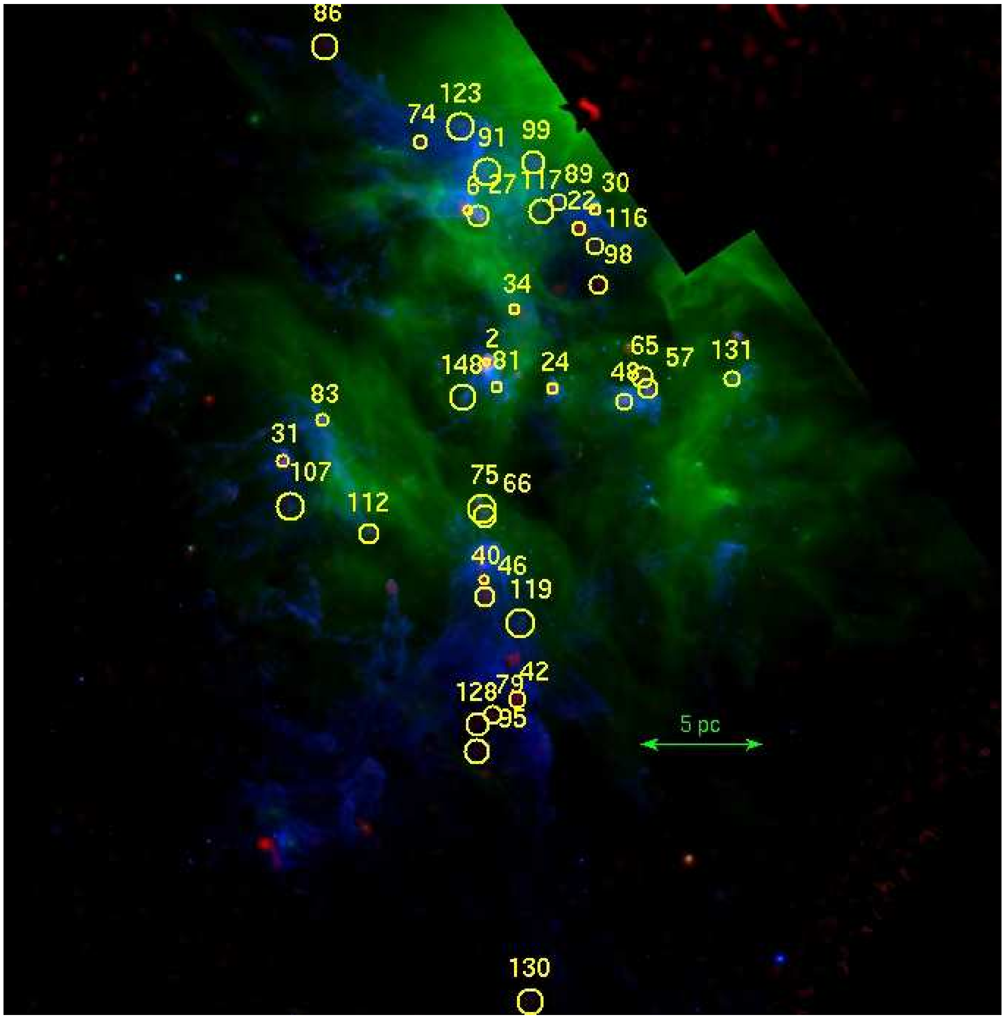

Figure 6.2: Spatial distribution of starless cores in South Pillars. Circle sizes represent their densities, the smallest symbols indicate higher densities, while larger ones indicate lower densities (or more spread millimeter cores).

From a histogram of core sizes (Fig. 6.1) similar to a Gaussian distribution, the highest peak is located about 0.33 pc. Then, a good classification of core sizes ($s_c$) is: small cores $s_c < 0.25$ pc, medium size cores $0.25 \leq s_c < 0.45$ pc, and larger cores $s_c \geq 0.45$ pc. Based on this classification, 8 of the 13 cores in the first region (closer to $\eta$ Car) are medium size cores, and 5 are larger than 0.45 pc. The second region has a total of 8 cores, from which 1 is a small core, six are medium size cores, and only one has a size higher than 0.45 pc; while in the third region we have 2 small cores, 8 medium size cores, and 3 larger cores.

In summary, most of the cores in these regions are more or less compact, and this is a possible indication that single massive sources could be forming, while larger size cores could be either small young stellar clusters with sizes ∼0.5 to 2.0 pc (e.g. Porras et al., 2000, see also section 3.1), or they are condensations in a pre-collapsing stage. If the latest is the case, then the 5 larger cores close to $\eta$ Car could be prevented from collapse due to stellar wind from massive stars in the region, including $\eta$ Car itself. In total, in SPR there are 3 small cores, 26 medium size cores and 11 large cores. The small cores are located only in the second and third regions, whereas medium and large core size are located in all the regions. Cores AzTEC 086 and 130 are located far from other cores in the first and third regions respectively.

# Chapter 7

# Morphology of the South Pillars

## 7.1 Description of the AzTEC source regions

In the South Pillars region several dust pillars are revealed in IR maps, being the most prominent of all them the Giant Pillar (region E in Figure 7.1), which contains 12 identified millimeter sources. However, there are also 3 structures more or less aligned towards $\eta$ Car: The one that contains HH666 (related with the source AzTEC 026), a "twin" pillar to the East of HH666 pillar (which contains AzTEC 023), and the one to the SE of the Giant Pillar (where AzTEC 033 lies, see regions A, B and C, respectively). Additional objects of interest in this region are the bright cluster known as the Treasure Chest (region D) with 4 AzTEC sources around it, and the region (F) around the source IRAS10430-5431 close to the core AzTEC 030. Fig. 7.1 shows the star-forming sites (A to E) that will be discussed in this section, which also includes some examples of isolated AzTEC sources marked with diamonds.

A) **The region around HH666 (AzTEC 026):** The region around the Herbig-Haro object HH666 is a molecular globule in which there is only one millimeter source within a radius of about 0.4 pc, AzTEC 026 (see Figure 7.2, upper-right). Smith et al. (2004) reports that in the 24 $\mu$m map apparently there are no sources detected within the globule, only nebulosity; although, there are several sources detected at 8 $\mu$m around it. These authors also report HH666 IRS, the HH progenitor, as a Class I source, with luminosity from a few hundred to $10^3$ $L_\odot$, and a probable pre-main sequence mass of a few to 8 $M_\odot$, which is in agreement with the estimation obtained in this thesis, since HH666 associated millimeter source has a mass of $\sim$7.32 $M_\odot$ and a luminosity of 5.86e2 $L_\odot$. Furthermore, these authors estimate a flow dynamical age of HH666 of $\sim 10^4$ years, based on the distribution of bow shocks seen at $H\alpha$ filter. Given that this is nearly coincident with the SED fitting estimation of the stellar age of $8.96 \times 10^3$ yr, the expansion velocity of the jet should be greater than the characteristic velocity of $\sim$100 km/s assumed by Smith et al. (2004).

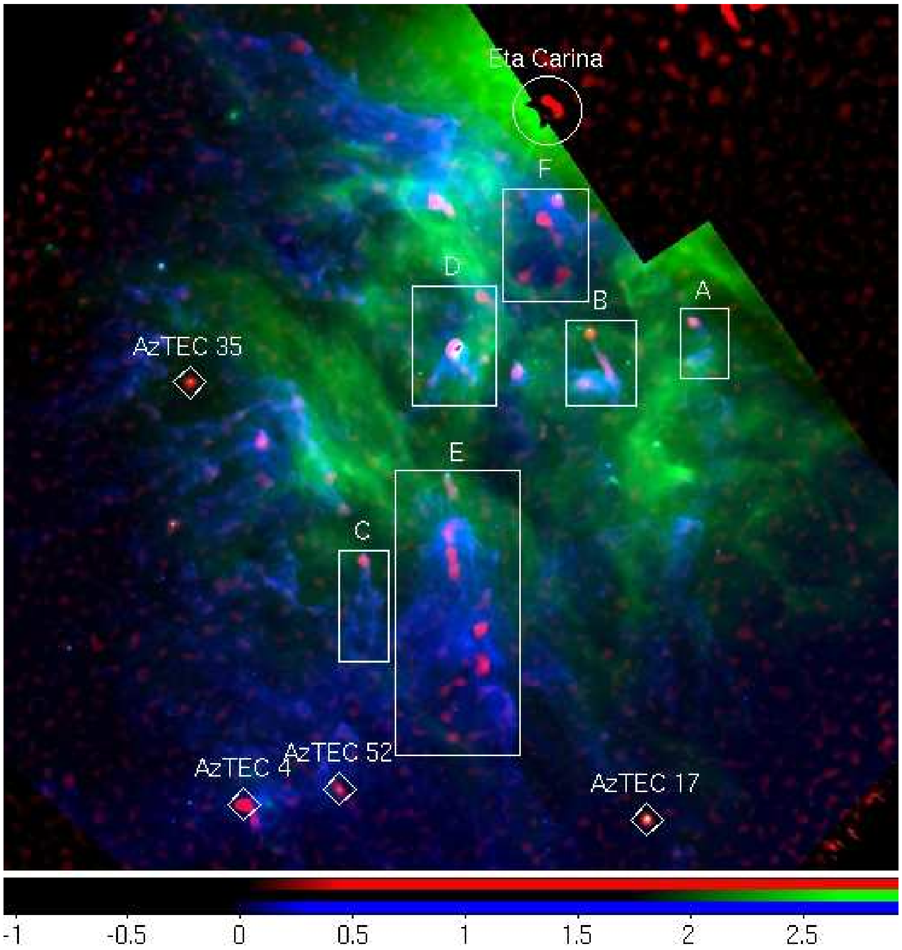

Figure 7.1: Regions that will be described in this section: **A.** The region around HH666, **B.** The outsides of G287.6790-0.8669, **C.** G288.0102-00.9639 and its surroundings, **D.** The young cluster Treasure Chest, **E.** The Giant Pillar and **F.** The region around the source IRAS10430-5431. Also, some AzTEC sources apparently isolated are marked with a rhombus. The colors in the image are *Red:* 1.1mm, *Green:* 24 $\mu$m, and *Blue:* 8 $\mu$m, which are the same for all the images shown in this chapter.

**B) The outsides of G287.6790-0.8669 (AzTEC 023; see Figure 7.2 top-row):** There are 4 AzTEC sources in this region: 023, 048, 057 and 065. AzTEC 023 is the tip of a pillar, and the rest lie in its body. Only AzTEC 023 has an associated stellar source, the YSO candidate G287.6790-0.8669 (see more sources in Mottram et al., 2007), with a mass of ~5 $M_\odot$ and an age of $1.07 \times 10^4$ yr from SED fit. The other 3 millimeter sources in this structure are starless cores. There are two other embedded sources seen as green point sources (24 $\mu$m) around this pillar, but they do not have any millimeter counterpart, neither appear in Povich et al. (2011) catalog. The closest one to AzTEC 023 is located at $\alpha = 10^h44^m50.44^s$, $\delta = -59°55'44.68''$ (J2000), at about 40 arcsec, while the farest one is about 3.2 arcmin from AzTEC 023, with coordinates $\alpha = 10^h44^m25.69^s$, $\delta = -59°58'01.07''$.

**C) G288.0102-00.9639 and its surroundings (AzTEC 033; see Figure 7.2, bottom row):** The millimeter source representative of this region, AzTEC 033, is about 20 arcsec to the south of G288.0099-00.9623 (Povich et al., 2011) which is located in the very tip of the pillar. In Smith et al. (2010a) there are two outflows reported in this pillar: HH1004 and HH1005. The driving source of the parsec-scale (1.7 pc) HH 1004 is considered to be in the "very tip of the dark pillar", and its position ($10^h46^m44.8^s$ $-60°10'20''$) is almost coincident (offset=0.68 arcsec) with the source G288.0102-00.9639 the embedded IR driving source of HH1005, based on the position of both sources. Furthermore, there is 8 $\mu$m extended emission showing pillar structure, but there are not any millimeter cores along it, as they appear in the pillar associated with AzTEC 023. This fact suggests that there is lower molecular mass in this region.

**D) The Treasure Chest (AzTEC 002; see Fig. 7.3 bottom left):** The Treasure Chest is a bright young stellar cluster (Smith et al., 2005), which in the millimeter map appears as a massive (∼22 400 $M_\odot$) dust core, AzTEC 002, of about 1 pc in size. There are also some millimeter sources detected around this region: the AzTEC sources 024, 034, 071, 081, and 148. The brightest star of the cluster, CPD-59°2661, is close (∼20 arcsec) to the AzTEC 002 centroid position. Most millimeter sources are considered starless cores, since AzTEC 071 is the only millimeter source that has an IR counterpart, which it is located almost in the center between the sources AzTEC 002 and 024 at about 2.2 arcmin from each one, but probably more related to AzTEC 002 due to a filamentary nebulosity at 8 $\mu$m that connects them. It is a Class 0/I source associated with a noticeable "duck-head" shape seen in IRAC bands. AzTEC 024, 034, and 081 are starless cores associated with a cavity shaped in 8 $\mu$m, seen as a dark nebulosity. Also, there are some IR Class 0/I sources around AzTEC 024 and 034. AzTEC 024 is located ∼4.4 arcmin SW from AzTEC 002, AzTEC 034 is about 3.7 arcmin NW, and AzTEC 081 at ∼1.6 arcmin to the SW. In the 24 $\mu$m map the nebulosity is extended to the North, suggesting that all millimeter sources might be connected to the same cloud, being the exception AzTEC 024.

**E) The Giant Pillar:** The Giant Pillar is a very large dust region in the south of $\eta$ Car which contains several embedded sources. Some millimeter sources are detected within this pillar: AzTEC 015, 040, 044, 046, 066, 075 and 119 are located in the head (See Fig. 7.3 left), whereas AzTEC 042, 079, 087, 095 and 128 are detected in the tail (See Figure 7.3 upper-left). These sources define quite well the Giant Pillar shape. The source G287.93-0.99 ($\alpha_{J2000} = 10^h45^m56.1^s$, $\delta_{J2000} = -60°08'50''$, (Rathborne et al., 2004) is within this region, but a millimeter counterpart is not clear. Another interesting luminous source, G287.88-0.93 ($\alpha_{J2000} = 10^h46^m00.9^s$, $\delta_{J2000} = -60°05'12''$), is not considered within the Giant Pillar by Rathborne et al. (2004). However, it is possible to observe a connection between the dust pillar and this source in the 8 $\mu$m map; and to note that there are two more millimeter sources close to it: the sources AzTEC 075 and

066. G287.88-0.93 can be distinguished in the 8 $\mu$m and 24 $\mu$m maps. AzTEC 044 has an associated IR counterpart, since this object has counterparts in MSX catalog in A and D bands, because it is also visible as a extended counterpart in IRAC, it is not included in this catalog. This object extends in a cavity at 8 and 24 $\mu$m, with some IR sources around. It is possible that this object can be part of a small cluster. The region to the south of the Giant Pillar (its "tail", see Fig. 7.3 upper right), contains a complex chain of millimeter sources, 4 starless cores and some dimmer objects, plus one YSOc, AzTEC 087, which are located in the periphery of a cavity shaped at 24 $\mu$m.

**F) The source IRAS10430-5431 (AzTEC 030; see Fig. 7.3 bottom-right):** This region is about 6.1 arcmin to the south of $\eta$ Car, and is dominated by the bright source G287.63-0.72 (Smith & Brooks, 2008), which is about 20 arcsec to the North of the starless core AzTEC 030. South to this core, there is an obscure region in 8 and 24 $\mu$m that includes in its border other 4 starless cores: AzTEC 022, 063, 098, and 116. All of them are inside an oval cavity (size $3 \times 4$ arcmin) formed by the 24 $\mu$m emission, which is located to the south of $\eta$ Car, at about 10 arcmin.

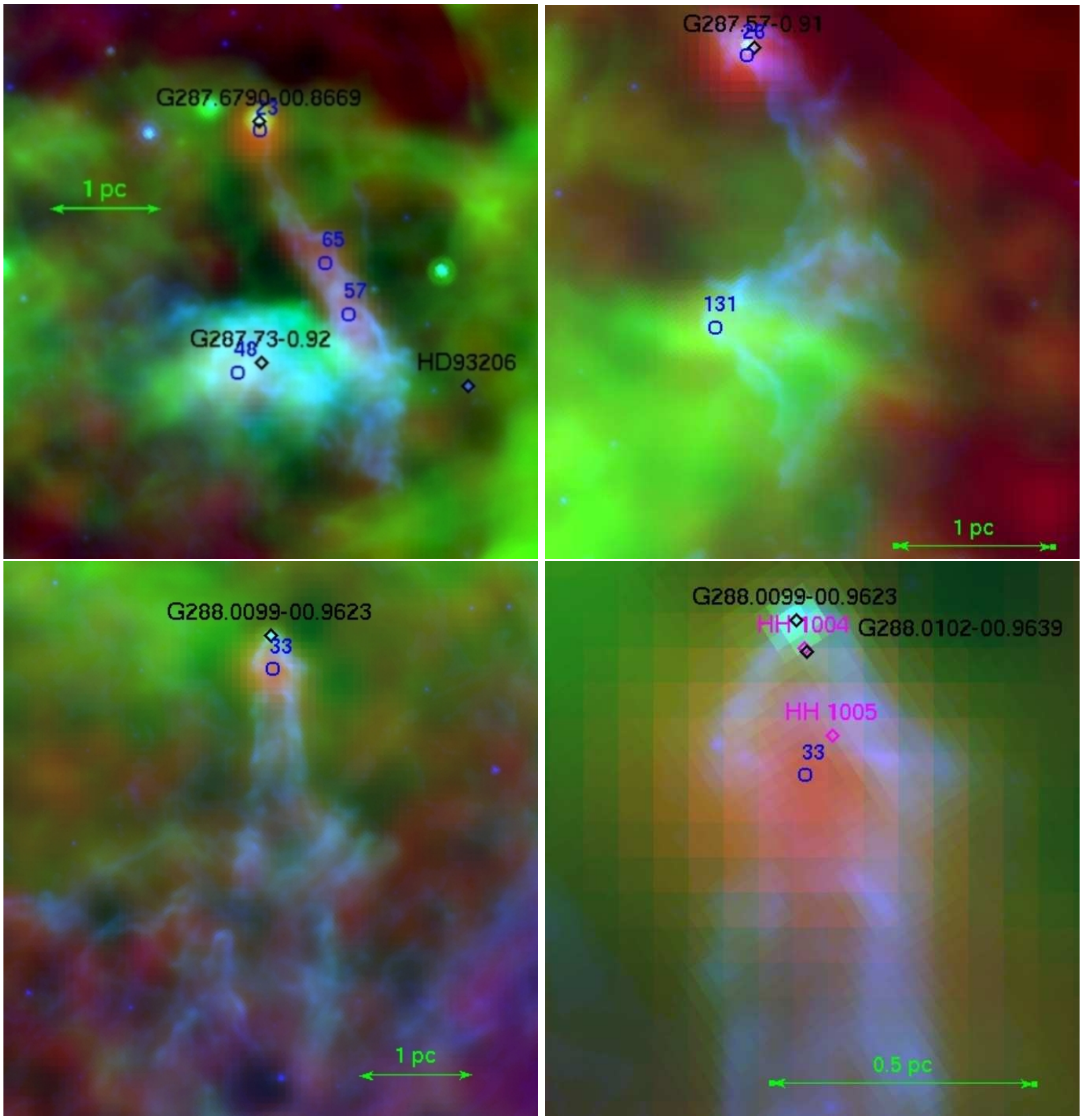

Figure 7.2: *Upper-left:* The YSO candidate *G287.6790-0.8669*, very close to the source AzTEC 023. Both are within a pillar with a easily recognized shape in blue. The sources *G287.73-0.92*, AzTEC 048, 057 and 065 are too within the pillar. *Upper-right:* The object HH666 with the source AzTEC 026, both are in the tip of the dust column (seen in blue). Source AzTEC 026 is clearly brighter that the source AzTEC 131 in the pillar. *Bottom-left:* The source *G288.0065-00.9561* together with the source AzTEC 033, where is clearly seen the shape of the pillar in blue color. *Bottom-right:* Zoom-in image from the last figure.

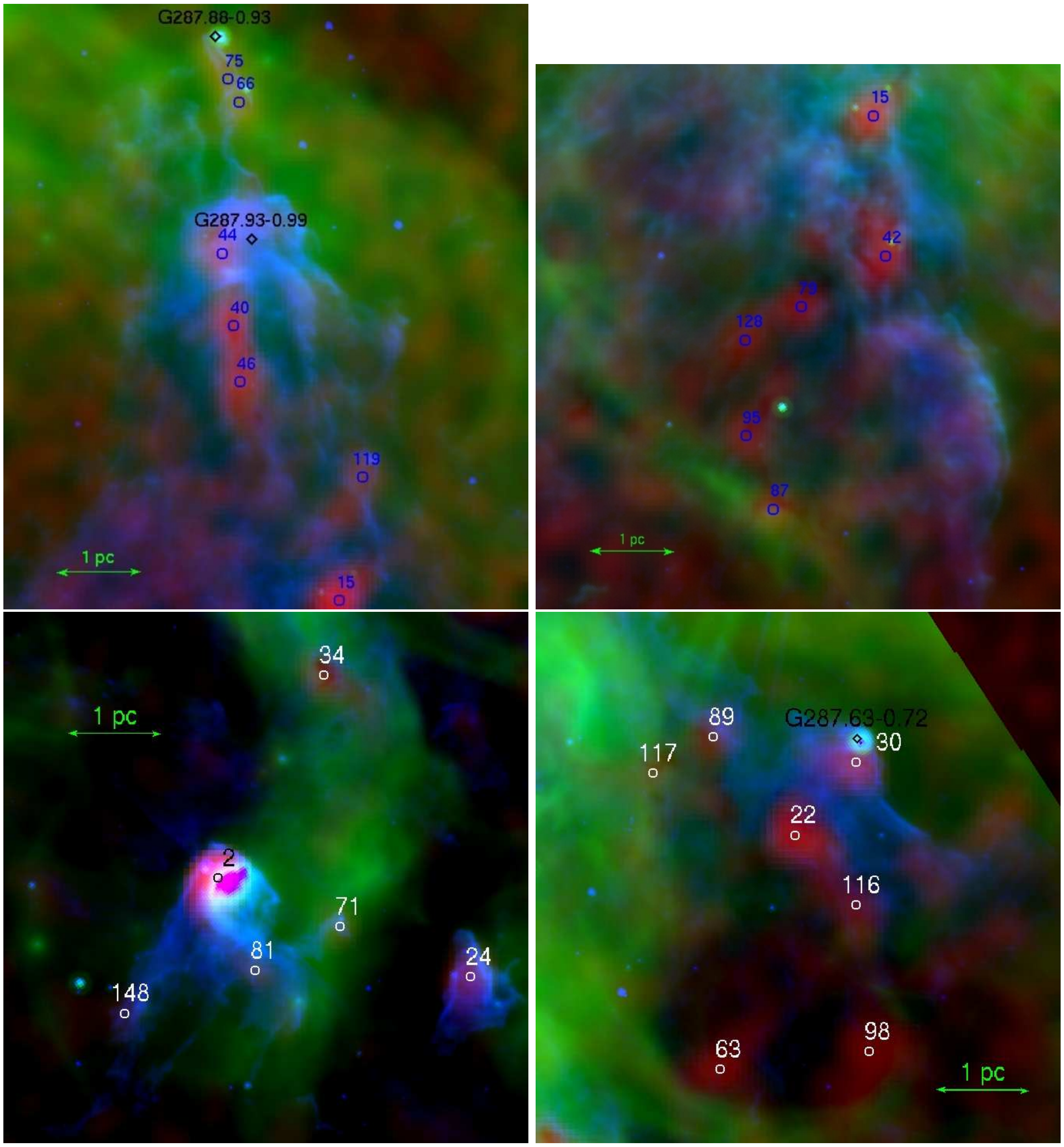

Figure 7.3: *Upper-left:* The region of the Giant Pillar. *Upper-right:* The tail of the Giant Pillar. *Bottom-left:* The region of the young cluster the Treasure Chest and some millimeter sources in its surroundings. *Bottom-right:* The gas clouds around the source *IRAS10430-5431* and the millimeter sources around it. In all images, millimeter sources are marked with white circles. Black circles represent IR sources known.

## 7.2 Isolated AzTEC sources

In addition to the regions described above, there are interesting millimeter sources considered as isolated with respect to the location of other YSOc (see examples in Figure 7.1 and figures within this subsection). All of these isolated AzTEC objects are YSOc. They are listed in Table 7.2, and briefly described in the following lines.

Table 7.1: Isolated millimeter YSOc.

| **AzTEC Source** | **Counterparts**[a] (Bands) | **Stellar Mass** ($M_\odot$) | **Millimeter companions**[b] | **Projected distance from $\eta$ Car** (pc) | **Location Angle**[c] (°) |
|---|---|---|---|---|---|
| 004 | I1, I2, MIPS-24 | 4.23 | 60 | 32.9 | 156.4 |
| 017 | H, K, I1, I3, A, S9W, C, D, L18W, E, MIPS-24 | 8.20 | 237 | 31.2 | 187.6 |
| 035 | K, I1, I2, I3, I4, L18W, MIPS-24 | 7.81 | None | 19.7 | 127.3 |
| 052 | J, H, K, I1, I2, I3, I4, MIPS-24 | 2.31 | 278, 371 | 31.0 | 162.8 |
| 132 | H, K, I1, I2, I3, A, S9W, C, D, L18W, E, MIPS-24 | 9.80 | None | 24.6 | 138.6 |

---

[a] Within a radius of 10 arcsec. See Table 2.2 for the wavelength values of these bands.
[b] Within a radius $\lesssim$ 2.2 arcmin.
[c] Starting with 0° to the north of $\eta$ Car and increasing counterclockwise.

- **AzTEC 004:** This is the second brighter source (after the Treasure Chest), it falls about 50 arcmin (∼33 pc) to the SE of $\eta$ Car, has a diameter of about 1.3 arcmin, and a stellar mass of $\sim 4.2\ M_\odot$. It hides at least 3 bright embedded sources detected at Spitzer bands, that appear aligned towards an embedded pair at ∼45 arcsec (0.5 pc) to the NW. AzTEC 004 has a dimmer millimeter companion, the source AzTEC 060: a millimeter core. AzTEC 004 coincides very well with a hole in 8 $\mu$m band, and an empty region in K band which is surrounded by about eight sources. This is most probably a deeply embedded young stellar cluster (See Figure 7.4 left).

- **AzTEC 017:** This is a very interesting source, since it can be distinguished in all the maps, at a distance of 47 arcmin to the south of $\eta$-Car, with a stellar mass of $\sim 8.2\ M_\odot$, the highest of all YSOc. Appears in the millimeter map as a spherical core ($\sim 19.5$ arcsec radius) which contains a star, clearly seen in the MIPS24, and all IRAC bands. In the MIPS24 map seems to have a higher emission than in IRAC bands. There are two fainter companions probably in physical association with AzTEC 017. In IRAC bands, several sources with multiple companions are revealed (Fig.7.4 right).

- **AzTEC 035:** An isolated source which appears in the 1.1 millimeter map as a source with circular shape, with a diameter of about 1 arcmin, and a stellar mass of about $7.8\ M_\odot$; it could be a small cluster since the mm-emission encloses a big area (See Figure 7.5 left). In the 8 $\mu$m emission, is seen as a small cloud without nebulosity in its surroundings. There is a close Class 0/I companion 5 arcsec distant at SW of AzTEC 035, but there are other Class 0/I IR sources in the periphery and inside the almost circular cavity formed by dust seen in Spitzer bands. In the 24 $\mu$m emission, this object appears as an isolated source with some nebulosity around it, the only source seen in the 24 $\mu$m map close to AzTEC 035 is at a distance of about 1.6 arcmin.

- **AzTEC 052:** This isolated source is seen as an extended object in Spitzer bands, probably due to a double or a triple system associated. There are few sources at about ∼1 arcmin of AzTEC 052, more o less in a circular shape, with almost no nebulosity around. Millimeter emission of this object fills very well the hole that can be seen in 8 $\mu$m (Figure 7.5 right). It has the lowest mass of all YSOc: $\sim 2.3$ $M_\odot$.

- **AzTEC 132:** This source although not really a bright source (S/N ∼4), it has information in several wavelengths. In the 1.1 mm map this object has a diameter of about 1.1 arcmin, and is located in the middle of a chain of Class 0/I IR sources (Figure 7.6). In the 8 $\mu$m map the source is clearly seen around an envelope with a few sources detected in this wavelength. In all IRAC bands, is possible distinguish a multiple system of at least 3 bright sources close to AzTEC 132. A single source is seen in the 24 $\mu$m map with some nebulosity around it. Its stellar mass is about $6.3\ M_\odot$.

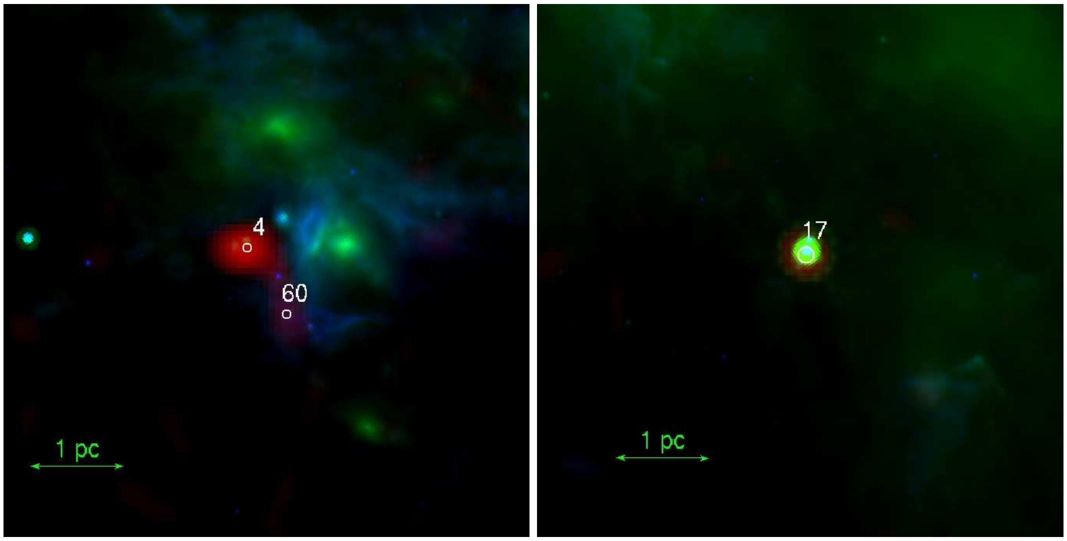

Figure 7.4: *Left:* Isolated source AzTEC 004. *Right:* Isolated source AzTEC 017.

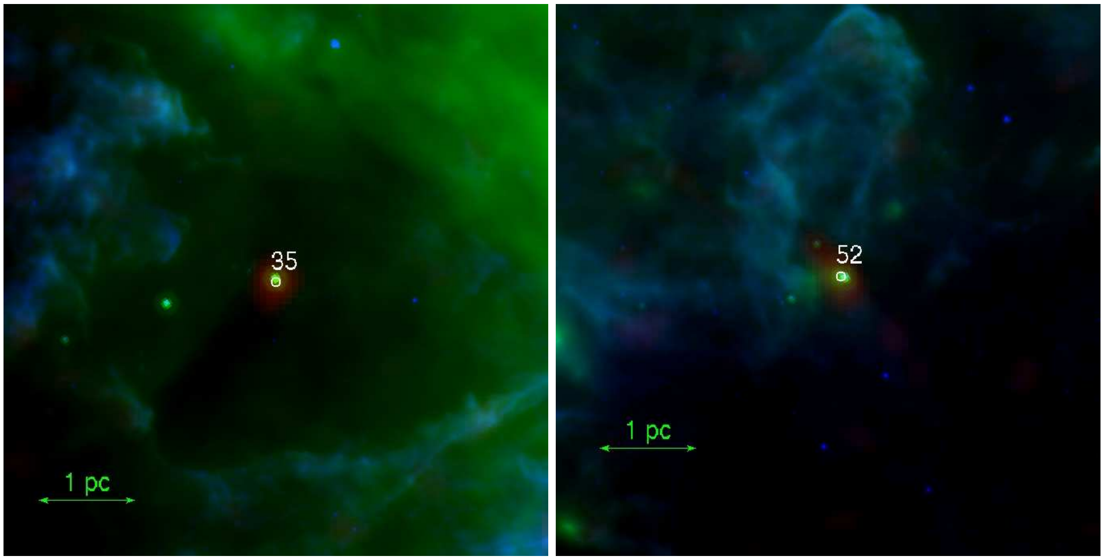

Figure 7.5: *Left:* Isolated source AzTEC 035. *Right:* Isolated source AzTEC 052.

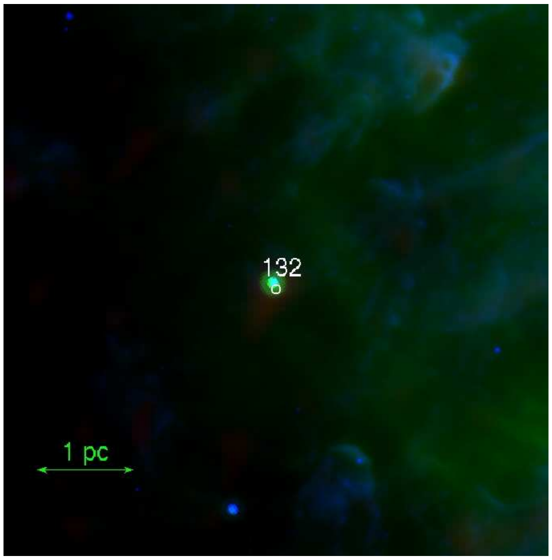

Figure 7.6: Isolated source AzTEC 132.

# Chapter 8

# Summary and Conclusions

1. A multi-wavelength photometric catalog of about 38 000 sources from 2 $\mu$m to 1.1 mm in a 1 square degree are of the Carina South Pillar Region has been constructed. This catalog is based on millimeter observations with the bolometer array AzTEC as a visitor instrument to ASTE telescope and IR public available data. It is found that 118/38000 of the total sources in the region are millimeter AzTEC sources.
2. This work is focused on the population of 118 millimeter point-like sources with and without IR counterpart, which are identified as either YSO candidates (YSOc) or as possible starless cores (Enoch et al., 2008, and references therein), respectively. After a visual inspection of 52/118 millimeter sources with S/N $\geq$ 4 (or integrated flux $\geq$ 300 mJy), a total of 12 YSOc and 40 starless cores are reported.
3. A primary observational classification of embedded sources, based on estimations of the IR index $\alpha_{IR} \equiv d\log(\lambda F_\lambda)/d\log\lambda$ ($\lambda$ from 2.12 to 24 $\mu$m), gives about 33 700 objects classified as Class III, 2300 as Class II and 900 as Class 0/I.
4. With the help of NIR diagnostic diagrams, a mean extinction value $A_V \sim 15$ mag from embedded main sequence stars is estimated. Furthermore, the MIR diagrams show also a more embedded young object population with larger $A_V$ values. Although a complete study based on mid-IR and millimeter interstellar extinction maps is necessary to better estimate individual $A_V$ values, the extinction estimated from NIR photometry provides an acceptable constrain to physical parameters from the fitted models (Robitaille et al., 2007) to the YSOc sample.
5. In summary, 17% of AzTEC sources (S/N $>$ 4) lie within a pillar body, and only 3-4 associated with the pillar head. Also 15% are located within an irradiated edge structure. Almost 40% show IR sources near or associated the millimeter emission, and 25% show more than one source related to the millimeter emission. All of these sources are good candidates to be observed with larger angular resolution (e.g., LMT, ALMA).

6. **Physical parameters of 12 YSOc fitted by SEDs range from 2.31 to 8.20 $M_\odot$ for stellar mass with a peak in ∼7$M_\odot$; 3.42e-1 to 1.74e-4 $M_\odot$ for disk mass and a peak between $10^{-1}$ and $10^{-2}$ $M_\odot$; 8.13 and 3.43e2 $M_\odot$ for envelope mass and a peak $\sim 10^2$ $M_\odot$; and 7.13e1 to 4.56e3 $L_\odot$ for total luminosity with a peak $\sim 10^2$ $L_\odot$. While 5/12 YSOc have masses between 7 and 8 $M_\odot$, only one YSOc (AzTEC 052) has a stellar mass smaller than 3 $M_\odot$ (and appears 31 pc far from $\eta$ Car). More massive YSOc are closer to $\eta$ Car.**
7. **12 YSOc were *a priori* classified using Lada IR index, resulting in 2 Class II and 10 Class 0/I. Using physical parameters from SED fitting, and Andre et al. (1993) and Hennemann et al. (2010) criteria for $L_{submm}/L_{tot}$, the 12 YSOc are classified as Class 0. Also, according with the position of YSOc in $M_{env}$ vs $L_{tot}$ from Molinari et al. (2008), YSOc AzTEC 026, 035, 044, and 087 are most probably Class 0.**
8. **40 starless cores have integrated fluxes from about 300 to 2900 mJy. Assuming standard considerations such as $\kappa_V = 0.0114$ cm$^2$ g$^{-1}$ and $T_{dust}$=10 K, these values imply a core mass range of about 1800 $-$ 100 000 $M_\odot$ with a median value of $\sim$ 3480 $M_\odot$. Then, core mass-densities are from $10^4$ to $10^6$ cm$^{-3}$, with an average value of $4.7e5$ cm$^{-3}$, assuming an homogeneous mass distribution in a spherical volume.**
9. After a brief analysis of the parameters that may alter the estimation of core mass and core density, these estimation for AzTEC cores are in better agreement with those estimated on cores at star-forming complexes suspected of undergoing massive star formation (Hill et al., 2005).
10. AzTEC sources lying in the pillar heads most probably are associated with exciting stars of HH objects, some of them are already reported (Smith et al. (2004), Smith et al. (2010a)). The largest pillar structure, known as the Giant Pillar, contains nine AzTEC sources and several Class 0/I IR objects.
11. Five AzTEC sources are classified as “isolated” in regard of their location relative to other millimeter sources. In general, these isolated objects appear surrounded by –or are part of– a chain of IR Class 0/I YSOs.

## 8.1 Future work

- AzTEC starless cores are good candidates to be observed in higher angular resolution telescopes (LTM, ALMA) in order to improve their association with submillimeter counterparts (Herschel, LABOCA). These sources are suspected to be real Class 0 objects (Without fluxes in wavelengths $\leq$ 10 $\mu$m), and their physical parameters are needed to be characterized.

- Use the technique *Fruit-Loops* to generate extended emission maps at 1.1 mm, together with 8 and 24 $\mu$m maps, generate more detailed extinction maps towards this region.

# Figure Index

# Table Index

# References

Allen, D. A., & Hillier, D. J. 1993, Proceedings of the Astronomical Society of Australia, 10, 338

Andre, P. ., Ward-Thompson, D., & Barsony, M. 2000, Protostars and Planets IV, 59

Andre, P., Ward-Thompson, D., & Barsony, M. 1993, ApJ, 406, 122

Barsony, M., Ward-Thompson, D., Andre, P., & O'Linger, J. 1997, in Bulletin of the American Astronomical Society, Vol. 29, American Astronomical Society Meeting Abstracts, 1361–+

Bernasconi, P. A., & Maeder, A. 1996, A&A, 307, 829

Bonnell, I. A. 2002, in Astronomical Society of the Pacific Conference Series, Vol. 267, Hot Star Workshop III: The Earliest Phases of Massive Star Birth, ed. P. Crowther, 193–+

Bonnell, I. A., Bate, M. R., & Zinnecker, H. 1998, MNRAS, 298, 93

Burbidge, G. R. 1962, ApJ, 136, 304

Carpenter, J. M., Meyer, M. R., Dougados, C., Strom, S. E., & Hillenbrand, L. A. 1997, AJ, 114, 198

Carroll, B. W., & Ostlie, D. A. 2007, An Introduction to Modern Astrophysics (Addison Wesley)

Chandler, C. J., Gear, W. K., Sandell, G., Hayashi, S., Duncan, W. D., Griffin, M. J., & Hazella, S. 1990, MNRAS, 243, 330

Cox, P., Mezger, P. G., Sievers, A., Najarro, F., Bronfman, L., Kreysa, E., & Haslam, G. 1995, A&A, 297, 168

Crowther, P. A. 2007, ARA&A, 45, 177

Crowther, P. A., Smith, L. J., Hillier, D. J., & Schmutz, W. 1995, A&A, 293, 427

Currie, D. G., Dowling, D. M., Shaya, E. J., Hester, J., Scowen, P., Groth, E. J., Lynds, R., O'neil, Jr., E. J., & Wide Field/Planetary Camera Instrument Definition Team. 1996, AJ, 112, 1115

Davidson, K., & Humphreys, R. M. 1997, ARA&A, 35, 1

Davies, B., Lumsden, S. L., Hoare, M. G., Oudmaijer, R. D., & de Wit, W.-J. 2010, MNRAS, 402, 1504

De Marchi, G., Paresce, F., Panagia, N., Beccari, G., Spezzi, L., Sirianni, M., Andersen, M., Mutchler, M., Balick, B., Dopita, M. A., Frogel, J. A., Whitmore, B. C., Bond, H., Calzetti, D., Carollo, C. M., Disney, M. J., Hall, D. N. B., Holtzman, J. A., Kimble, R. A., McCarthy, P. J., O'Connell, R. W., Saha, A., Silk, J. I., Trauger, J. T., Walker, A. R., Windhorst, R. A., & Young, E. T. 2011, ApJ, 739, 27

di Francesco, J., Evans, II, N. J., Caselli, P., Myers, P. C., Shirley, Y., Aikawa, Y., & Tafalla, M. 2007, Protostars and Planets V, 17

Enoch, M. L., Evans, II, N. J., Sargent, A. I., & Glenn, J. 2009, ApJ, 692, 973

Enoch, M. L., Evans, II, N. J., Sargent, A. I., Glenn, J., Rosolowsky, E., & Myers, P. 2008, ApJ, 684, 1240

Ercolano, B., Bevan, A., & Robitaille, T. 2013, MNRAS, 428, 2714

Estalella, R., & Anglada, G. 1996, Introducción a la Física del Medio Interestelar (Edicions de la Universitat de Barcelona)

Fazio, G. G., Hora, J. L., Allen, L. E., Ashby, M. L. N., Barmby, P., Deutsch, L. K., Huang, J.-S., Kleiner, S., Marengo, M., Megeath, S. T., Melnick, G. J., Pahre, M. A., Patten, B. M., Polizotti, J., Smith, H. A., Taylor, R. S., Wang, Z., Willner, S. P., Hoffmann, W. F., Pipher, J. L., Forrest, W. J., McMurty, C. W., McCreight, C. R., McKelvey, M. E., McMurray, R. E., Koch, D. G., Moseley, S. H., Arendt, R. G., Mentzell, J. E., Marx, C. T., Losch, P., Mayman, P., Eichhorn, W., Krebs, D., Jhabvala, M., Gezari, D. Y., Fixsen, D. J., Flores, J., Shakoorzadeh, K., Jungo, R., Hakun, C., Workman, L., Karpati, G., Kichak, R., Whitley, R., Mann, S., Tollestrup, E. V., Eisenhardt, P., Stern, D., Gorjian, V., Bhattacharya, B., Carey, S., Nelson, B. O., Glaccum, W. J., Lacy, M., Lowrance, P. J., Laine, S., Reach, W. T., Stauffer, J. A., Surace, J. A., Wilson, G., Wright, E. L., Hoffman, A., Domingo, G., & Cohen, M. 2004, ApJS, 154, 10

Gaczkowski, B., Preibisch, T., Ratzka, T., Roccatagliata, V., Ohlendorf, H., & Zinnecker, H. 2013, A&A, 549, A67

Gaposchkin, C. H. P. 1957, The galactic novae., ed. Gaposchkin, C. H. P.

Garay, G. 2004, in IAU Symposium, Vol. 221, Star Formation at High Angular Resolution, ed. M. G. Burton, R. Jayawardhana, & T. L. Bourke, 169–+

Garay, G., & Lizano, S. 1999, PASP, 111, 1049

Garay, G., Rodriguez, L. F., Moran, J. M., & Churchwell, E. 1993, ApJ, 418, 368

Gardner, F. F., Milne, D. K., Mezger, P. G., & Wilson, T. L. 1970, A&A, 7, 349

Gumley, L. E. 2002, Practical IDL Programming (Morgan Kaufmann)

Gutermuth, R. A., Myers, P. C., Megeath, S. T., Allen, L. E., Pipher, J. L., Muzerolle, J., Porras, A., Winston, E., & Fazio, G. 2008, ApJ, 674, 336

Hennemann, M., Motte, F., Bontemps, S., Schneider, N., Csengeri, T., Balog, Z., di Francesco, J., Zavagno, A., André, P., Men'shchikov, A., Abergel, A., Ali, B., Baluteau, J.-P., Bernard, J.-P., Cox, P., Didelon, P., di Giorgio, A.-M., Griffin, M., Hargrave, P., Hill, T., Horeau, B., Huang, M., Kirk, J., Leeks, S., Li, J. Z., Marston, A., Martin, P., Molinari, S., Nguyen Luong, Q., Olofsson, G., Persi, P., Pezzuto, S., Russeil, D., Saraceno, P., Sauvage, M., Sibthorpe, B., Spinoglio, L., Testi, L., Ward-Thompson, D., White, G., Wilson, C., & Woodcraft, A. 2010, A&A, 518, L84

Herter, T. L., Adams, J. D., De Buizer, J. M., Gull, G. E., Schoenwald, J., Henderson, C. P., Keller, L. D., Nikola, T., Stacey, G., & Vacca, W. D. 2012, ApJ, 749, L18

Hill, T., Burton, M. G., Minier, V., Thompson, M. A., Walsh, A. J., Hunt-Cunningham, M., & Garay, G. 2005, MNRAS, 363, 405

Hillenbrand, L. A., & Hartmann, L. W. 1998, ApJ, 492, 540

Hofner, P., Peterson, S., & Cesaroni, R. 1999, ApJ, 514, 899

Hollenbach, D. J., Yorke, H. W., & Johnstone, D. 2000, Protostars and Planets IV, 401

Hughes, D. H., Jáuregui Correa, J.-C., Schloerb, F. P., Erickson, N., Romero, J. G., Heyer, M., Reynoso, D. H., Narayanan, G., Perez-Grovas, A. S., Souccar, K., Wilson, G., & Yun, M. 2010, in Society of Photo-Optical Instrumentation Engineers (SPIE) Conference Series, Vol. 7733, Society of Photo-Optical Instrumentation Engineers (SPIE) Conference Series

Humphreys, R. M., & Davidson, K. 1994, PASP, 106, 1025

Irvine, W. M., Carrasco, E., & Aretxaga, I. 2005, The Large Millimeter Telescope (University of Massachusetts Amherst / Instituto Nacional de Astrofísica, Óptica y Electrónica)

Kenyon, S. J., Hartmann, L. W., Strom, K. M., & Strom, S. E. 1990, AJ, 99, 869

Kohno, K. 2005, in Astronomical Society of the Pacific Conference Series, Vol. 344, The Cool Universe: Observing Cosmic Dawn, ed. C. Lidman & D. Alloin, 242–+

Kraus, S., Hofmann, K.-H., Menten, K. M., Schertl, D., Weigelt, G., Wyrowski, F., Meilland, A., Perraut, K., Petrov, R., Robbe-Dubois, S., Schilke, P., & Testi, L. 2010, Nature, 466, 339

Krumholz, M. R., Klein, R. I., McKee, C. F., Offner, S. S. R., & Cunningham, A. J. 2009, Science, 323, 754

Lada, C. J. 1987, in IAU Symposium, Vol. 115, Star Forming Regions, ed. M. Peimbert & J. Jugaku, 1–17

Lada, C. J., & Lada, E. A. 2003, ARA&A, 41, 57

Ladd, E. F., Adams, F. C., Casey, S., Davidson, J. A., Fuller, G. A., Harper, D. A., Myers, P. C., & Padman, R. 1991, ApJ, 366, 203

Larson, R. B. 1982, MNRAS, 200, 159

Massey, P., & Hunter, D. A. 1998, ApJ, 493, 180

McKee, C. F., & Tan, J. 2003, ApJ, 585, 850

McKee, C. F., & Tan, J. C. 2002, Nature, 416, 59

Megeath, S. T., Cox, P., Bronfman, L., & Roelfsema, P. R. 1996a, A&A, 305, 296

Megeath, S. T., Herter, T., Beichman, C., Gautier, N., Hester, J. J., Rayner, J., & Shupe, D. 1996b, A&A, 307, 775

Mill, J. D., O’Neil, R. R., Price, S., Romick, G. J., Uy, O. M., Gaposchkin, E. M., Light, G. C., Moore, Jr., W. W., Murdock, T. L., & Stair, Jr., A. T. 1994, Journal of Spacecraft and Rockets, 31, 900

Molinari, S., Pezzuto, S., Cesaroni, R., Brand, J., Faustini, F., & Testi, L. 2008, A&A, 481, 345

Motte, F., Bontemps, S., Schilke, P., Schneider, N., Menten, K. M., & Broguière, D. 2007, A&A, 476, 1243

Mottram, J. C., Hoare, M. G., Lumsden, S. L., Oudmaijer, R. D., Urquhart, J. S., Sheret, T. L., Clarke, A. J., & Allsopp, J. 2007, A&A, 476, 1019

Murakami, H., Baba, H., Barthel, P., Clements, D. L., Cohen, M., Doi, Y., Enya, K., Figueredo, E., Fujishiro, N., Fujiwara, H., Fujiwara, M., Garcia-Lario, P., Goto, T., Hasegawa, S., Hibi, Y., Hirao, T., Hiromoto, N., Hong, S. S., Imai, K., Ishigaki, M., Ishiguro, M., Ishihara, D., Ita, Y., Jeong, W.-S., Jeong, K. S., Kaneda, H., Kataza, H., Kawada, M., Kawai, T., Kawamura, A., Kessler, M. F., Kester, D., Kii, T., Kim, D. C., Kim, W., Kobayashi, H., Koo, B. C., Kwon, S. M., Lee, H. M., Lorente, R., Makiuti, S., Matsuhara, H., Matsumoto, T., Matsuo, H., Matsuura, S., Müller, T. G., Murakami, N., Nagata, H., Nakagawa, T., Naoi, T., Narita, M., Noda, M., Oh, S. H., Ohnishi, A., Ohyama, Y., Okada, Y., Okuda, H., Oliver, S., Onaka, T., Ootsubo, T., Oyabu, S., Pak, S., Park, Y.-S., Pearson, C. P., Rowan-Robinson, M., Saito, T., Sakon, I., Salama, A., Sato, S., Savage, R. S., Serjeant, S., Shibai, H., Shirahata, M., Sohn, J., Suzuki, T., Takagi, T., Takahashi, H., Tanabé, T., Takeuchi, T. T., Takita, S., Thomson, M., Uemizu, K., Ueno, M., Usui, F., Verdugo, E., Wada, T., Wang, L., Watabe, T., Watarai, H., White, G. J., Yamamura, I., Yamauchi, C., & Yasuda, A. 2007, PASJ, 59, 369

Ohlendorf, H., Preibisch, T., Gaczkowski, B., Ratzka, T., Grellmann, R., & McLeod, A. F. 2012, A&A, 540, A81

Osorio, M., Lizano, S., & D’Alessio, P. 1999, ApJ, 525, 808

Ossenkopf, V., & Henning, T. 1994, A&A, 291, 943

Parker, R. J., & Goodwin, S. P. 2007, MNRAS, 380, 1271

Pérez-Grovas, A. S., Schloerb, F. P., Hughes, D., & Yun, M. 2006, in Society of Photo-Optical Instrumentation Engineers (SPIE) Conference Series, Vol. 6267, Society of Photo-Optical Instrumentation Engineers (SPIE) Conference Series

Plambeck, R. L., Wright, M. C. H., Friedel, D. N., Widicus Weaver, S. L., Bolatto, A. D., Pound, M. W., Woody, D. P., Lamb, J. W., & Scott, S. L. 2009, ApJ, 704, L25

Porras, A., Cruz-González, I., & Salas, L. 2000, in ESA Special Publication, Vol. 445, Star Formation from the Small to the Large Scale, ed. F. Favata, A. Kaas, & A. Wilson, 491

Povich, M. S., Smith, N., Majewski, S. R., Getman, K. V., Townsley, L. K., Babler, B. L., Broos, P. S., Indebetouw, R., Meade, M. R., Robitaille, T. P., Stassun, K. G., Whitney, B. A., Yonekura, Y., & Fukui, Y. 2011, ApJS, 194, 14

Preibisch, T., Ratzka, T., Gehring, T., Ohlendorf, H., Zinnecker, H., King, R. R., McCaughrean, M. J., & Lewis, J. R. 2011, A&A, 530, A40

Rathborne, J. M., Brooks, K. J., Burton, M. G., Cohen, M., & Bontemps, S. 2004, A&A, 418, 563

Richling, S., & Yorke, H. W. 1997, A&A, 327, 317

Rieke, G. H., Young, E. T., Engelbracht, C. W., Kelly, D. M., Low, F. J., Haller, E. E., Beeman, J. W., Gordon, K. D., Stansberry, J. A., Misselt, K. A., Cadien, J., Morrison, J. E., Rivlis, G., Latter, W. B., Noriega-Crespo, A., Padgett, D. L., Stapelfeldt, K. R., Hines, D. C., Egami, E., Muzerolle, J., Alonso-Herrero, A., Blaylock, M., Dole, H., Hinz, J. L., Le Floc'h, E., Papovich, C., Pérez-González, P. G., Smith, P. S., Su, K. Y. L., Bennett, L., Frayer, D. T., Henderson, D., Lu, N., Masci, F., Pesenson, M., Rebull, L., Rho, J., Keene, J., Stolovy, S., Wachter, S., Wheaton, W., Werner, M. W., & Richards, P. L. 2004, ApJS, 154, 25

Robitaille, T. P., Whitney, B. A., Indebetouw, R., & Wood, K. 2007, ApJS, 169, 328

Robitaille, T. P., Whitney, B. A., Indebetouw, R., Wood, K., & Denzmore, P. 2006, ApJS, 167, 256

Scott, K. S., Austermann, J. E., Perera, T. A., Wilson, G. W., Aretxaga, I., Bock, J. J., Hughes, D. H., Kang, Y., Kim, S., Mauskopf, P. D., Sanders, D. B., Scoville, N., & Yun, M. S. 2008, MNRAS, 385, 2225

Shirley, Y. L., Huard, T. L., Pontoppidan, K. M., Wilner, D. J., Stutz, A. M., Bieging, J. H., & Evans, II, N. J. 2011, ApJ, 728, 143

Sjouwerman, L. O., Capen, S. M., & Claussen, M. J. 2009, ApJ, 705, 1554

Skrutskie, M. F., Cutri, R. M., Stiening, R., Weinberg, M. D., Schneider, S., Carpenter, J. M., Beichman, C., Capps, R., Chester, T., Elias, J., Huchra, J., Liebert, J., Lonsdale, C., Monet, D. G., Price, S., Seitzer, P., Jarrett, T., Kirkpatrick, J. D., Gizis, J. E., Howard, E., Evans, T., Fowler, J., Fullmer, L., Hurt, R., Light, R., Kopan, E. L., Marsh, K. A., McCallon, H. L., Tam, R., Van Dyk, S., & Wheelock, S. 2006, AJ, 131, 1163

Smith, N. . 2006, MNRAS, 367, 763

Smith, N. 2002, MNRAS, 337, 1252

Smith, N., Bally, J., & Brooks, K. J. 2004, AJ, 127, 2793

Smith, N., Bally, J., & Walborn, N. R. 2010a, MNRAS, 405, 1153

Smith, N., & Brooks, K. J. 2008, The Carina Nebula: A Laboratory for Feedback and Triggered Star Formation, ed. Reipurth, B., 138–+

Smith, N., & Conti, P. S. 2008, ApJ, 679, 1467

Smith, N., Egan, M. P., Carey, S., Price, S. D., Morse, J. A., & Price, P. A. 2000, ApJ, 532, L145

Smith, N., & Frew, D. J. 2011, MNRAS, 415, 2009

Smith, N., Povich, M. S., Whitney, B. A., Churchwell, E., Babler, B. L., Meade, M. R., Bally, J., Gehrz, R. D., Robitaille, T. P., & Stassun, K. G. 2010b, MNRAS, 406, 952

Smith, N., Stassun, K. G., & Bally, J. 2005, AJ, 129, 888

Stahler, S. W., & Palla, F. 2004, The Formation of Stars (Wiley-VCH)

Stahler, S. W., Palla, F., & Ho, P. T. P. 2000, Protostars and Planets IV, 327

Takita, S., Kataza, H., Kitamura, Y., Ishihara, D., Ita, Y., Oyabu, S., & Ueno, M. 2010, A&A, 519, A83

Taylor, M. B. 2005, in Astronomical Society of the Pacific Conference Series, Vol. 347, Astronomical Data Analysis Software and Systems XIV, ed. P. Shopbell, M. Britton, & R. Ebert, 29

van Genderen, A. M., de Groot, M., & The, P. S. 1993, Space Sci. Rev., 66, 219

van Genderen, A. M., de Groot, M. J. H., & The, P. S. 1994, A&A, 283, 89

Walborn, N. R. 1973, ApJ, 179, 517

Walborn, N. R. 2002, in Astronomical Society of the Pacific Conference Series, Vol. 267, Hot Star Workshop III: The Earliest Phases of Massive Star Birth, ed. P. Crowther, 111–+

Walborn, N. R., Howarth, I. D., Lennon, D. J., Massey, P., Oey, M. S., Moffat, A. F. J., Skalkowski, G., Morrell, N. I., Drissen, L., & Parker, J. W. 2002, AJ, 123, 2754

Wang, K., Zhang, Q., Wu, Y., & Zhang, H. 2011, ApJ, 735, 64

Westphal, J. A., & Neubebauer, G. 1969, ApJ, 156, L45+

Whitney, B. A., Indebetouw, R., Bjorkman, J. E., & Wood, K. 2004, ApJ, 617, 1177

Wilking, B. A., Lada, C. J., & Young, E. T. 1989, ApJ, 340, 823

Wilson, G. W., Austermann, J. E., Perera, T. A., Scott, K. S., Ade, P. A. R., Bock, J. J., Glenn, J., Golwala, S. R., Kim, S., Kang, Y., Lydon, D., Mauskopf, P. D., Predmore, C. R., Roberts, C. M., Souccar, K., & Yun, M. S. 2008, MNRAS, 386, 807

Yorke, H. W. 2004, in IAU Symposium, Vol. 221, Star Formation at High Angular Resolution, ed. M. G. Burton, R. Jayawardhana, & T. L. Bourke, 141–+

Yorke, H. W., & Sonnhalter, C. 2002, ApJ, 569, 846

Young, K. E., Enoch, M. L., Evans, II, N. J., Glenn, J., Sargent, A., Huard, T. L., Aguirre, J., Golwala, S., Haig, D., Harvey, P., Laurent, G., Mauskopf, P., & Sayers, J. 2006, ApJ, 644, 326

Zhang, Q., & Ho, P. T. P. 1997, ApJ, 488, 241

Zhang, Y., Tan, J. C., De Buizer, J. M., Sandell, G., Beltran, M. T., Churchwell, E., McKee, C. F., Shuping, R., Staff, J. E., Telesco, C., & Whitney, B. 2013, ApJ, 767, 58

Zinnecker, H. 2004, in Astronomical Society of the Pacific Conference Series, Vol. 322, The Formation and Evolution of Massive Young Star Clusters, ed. H. J. G. L. M. Lamers, L. J. Smith, & A. Nota, 349–+

Zinnecker, H., & Yorke, H. W. 2007, ARA&A, 45, 481